Microfluidic Study of In-Situ Recovery of Bitumen in Solvent-Based Processes

by

Kiarash Keshmiri

A thesis submitted in partial fulfillment of the requirements for the degree of

Doctor of Philosophy

In

Chemical Engineering

Department of Chemical and Materials Engineering
University of Alberta

Abstract

Viscosity reduction is critically important for heavy oil extraction and experimental studies have shown this can be achieved by injection of a light solvent into a reservoir and dilution of heavy oil in place. Solvent-based methods have challenges like slow diffusion process and oil production rate as well as high cost of solvent. There is presently a lack of understanding regarding the pore-scale mechanisms involved in dilution of bitumen. Therefore, microfluidic as the science of fluid flow in micro-scale, has a great potential to play a significant role in the investigation and development of solvent-based heavy oil extraction methods. However, microfluidic is limited in applicability due to materials and operating condition.

In the first section of this work, possibility of using poly(dimethylsiloxane) (PDMS) microchannels in solvent-based bitumen extraction methods is studied. Swelling ratio of PDMS samples in different organic solvents and diluted bitumen were evaluated. We were particularly interested in the kinetic of swelling, deformation, and discoloration of PDMS. The hypothesis was that a PDMS microchip can still be used if the experiment time is much shorter than the time it takes for PDMS discoloration and deformation. The effect of surface coating on bitumen resistivity and compatibility of PDMS slabs was also studied.

Choosing the best material for micromodel fabrication, this thesis focuses on the experimental observation and characterization of solvent-based bitumen extraction. In the second section, a microchannel was used to measure hexane diffusion in bitumen with tremendously tiny amount of solvent and bitumen compared with prevalent methods. Semitransparent nature of bitumen facilitates the application of light transmission imaging during the time and relating intensities to solvent concentration. Diffusion mass transfer was studied with consideration of

Fickian and Single-File mass transfer mechanisms and corresponding equation was applied to calculate diffusion coefficient. The accuracy of Fickian mass transfer mechanism was confirmed with calculating values of fitting parameter (i.e. n_w) in addition to superimposition of data for both techniques. Comparison between constant and concentration dependent coefficients revealed that application of constant value causes up to 100 times larger coefficients specially at high (>0.85) and low (<0.15) hexane concentration. Diffusion of n-alkane solvent in bitumen leads to asphaltene precipitation and flow of diluted bitumen in the porous media.

Understanding of fluid flow in porous media is critically important for heavy oil and bitumen recovery. Therefore, capillary filling of pure liquids and diluted bitumen were experimentally monitored using white light microscope and compared with Washburn theoretical model. In addition, capillary filling of bitumen samples in periodically constricted microchannels was compared with Navier-Stokes equation. Glass microchannels were treated with two silanes which changed the water contact angle from 15° (untreated) to 115° (treated) microchannels. For all the samples, a linear relation between square of propagation distance and time was found as expected in the case of Washburn model. Experimental results indicated slower velocity compared to theoretical prediction due to simplifications of the Washburn model. Dynamic contact angles were measured and compared with predicted values using image processing.

Solvent diffusion in bitumen causes in-situ upgrading and asphaltene precipitation which causes pore clogging and prevents diluted oil to drain towards the production well. Understanding of asphaltene precipitation and deposition improves the efficiency of solvent-based extraction methods and solvent selection. In the last section of this study, micromodel was used to study asphaltene deposition. Detection point of asphaltene deposition showed faster precipitation from n-pentane compared with n-decane. Structure of asphaltene precipitates were

evaluated with Helium Ion Microscopy (HIM). A high-resolution total internal reflection fluorescence (TIRF) microscopy was used to identify the morphology of precipitates and results compared with HIM. While precipitated asphaltene with heavier solvent had larger particles, light solvent formed higher aggregation and formation damage, accordingly.

Preface

Chapter 3 was done in collaboration with Nicholas Moore, a bachelor student in department of Chemical and Material Engineering at University of Alberta. Nicholas Moore measured the weight of PDMS samples submerged in pure solvents. The rest of the theoretical experimental study, characterization, and writing manuscript was conducted by myself. A version of this chapter has been submitted to the Journal of Petroleum Science and Technology and is under review for publication.

Chapter 4 was done in collaboration with Mohammad Pourmohammadbagher, a master student in department of Chemical and Material Engineering at University of Alberta. He was responsible for X-ray experiments and its simulation. I was in charge of microfluidic experimental and simulation section and we both collaborate on evaluation of mass transfer mechanism. A version of this chapter has been submitted to the Fuel journal and is under review for publication.

Chapter 5 of this thesis has been presented in Proceedings of the ASME 5th Joint US-European Fluids Engineering Summer Conference FEDSM2018 as K. Keshmiri, H. Huang, N. Nazemifard, “Effects of Wettability on Capillary Flow on non-Newtonian Fluid in Microchannels”. I was responsible for the data collection and analysis as well as the manuscript composition.

Chapter 6 was done in collaboration with Seyedehniloufar Manafi, a research assistant at University of Alberta. Seyedehniloufar made TIRF images and 3D reconstruction of precipitated asphaltene. I was responsible for all the rest of experimental and characterization sections. A version of chapter 6 of this thesis is under review for submission to the Fuel journal as K.

Keshmiri, H. Huang, N. Nazemifard, “Microfluidic Platform to Evaluate Asphaltene Deposition During Solvent-Based Extraction of Heavy Oils”. I was responsible for the data collection and analysis as well as the manuscript composition.

Dedication:

To my beloved wife,

Who bring me happiness, love, support, and patience.

To my angel mother,

Who I owe her all I am.

To the loving memories of,

My father, “Jamshid” and my little sister, “Rojin”…

Acknowledgements

I would like to extend my deepest gratitude to my supervisor, Dr. Neda Nazemifard, for her encouragement, insightful expertise, and her support during the course of my PhD program. Her belief in me harnessed all the difficulties and gave me the confidence to pursue my ideas. I am really blessed to have her as my advisor through my research journey.

I would also like to thank Dr. Haibo Huang, my co-supervisor that I wholeheartedly enjoyed being a group member of his research team at InnoTech Alberta. Dr. Huang is an excellent team leader engineer with meticulous scientific integrity that taught me how to see a bigger picture of a challenge as a scientist with engineering prospective.

I am also thankful to Dr. Hyun-Joong Chung, my supervisory committee member, for his technical advice and support for providing experimental equipment in surface treatment and wettability alteration. Thank you to Dr. Aaron Hryciw from NanoFab for well addressing and being always available to explain any issue with micromodel fabrication. Great appreciation goes to my supportive lab mates and friends for their support and friendship. I thank Saeed, Hanrui, Swapnali, Sarang, Amin, Yucheng, Muhammad, Gunjan, and Kevan.

I gratefully acknowledge the financial support from InnoTech Alberta and Faculty of Graduate Studies and Research and scholarships from University of Alberta (NSERC, GSA).

The most difficult part of writing is how you truly thank your family. I would like to share my soul and show my deepest appreciation to my wife Niloufar who believed in me, cared about me, and inspired me through my life. No word can truly express my gratitude to my mother Minoo and my father Jamshid for their endless love and sacrifice. Your unending support is all I have in my life.

Table of Contents

List of Tables

List of Figures

List of Symbols

Symbols	Description	Units
ΔH_m	Enthalpy of mixing	$J.mol^{-1}$
V_m	Volume of mixture	$cm^3.mol^{-1}$
δ_i	Solubility parameter of the component i	$MPa^{0.5}$
$\emptyset_i$	Volume fraction of the component i	
ΔS_m	Entropy of mixing	$J.K^{-1}.mol^{-1}$
ΔG_m	Gibbs free energy of mixing	$J.mol^{-1}$
δ_p	Polar forces	$MPa^{0.5}$
δ_d	Dispersion forces	$MPa^{0.5}$
δ_h	Hydrogen bonding forces	$MPa^{0.5}$
R_i	Interaction radius	$MPa^{0.5}$
w_i	mass of swollen PDMS in each solvent	gr
n_w	Fitting parameter	
I_i	Light intensity in medium i	
ρ	Density	$mol.L^{-1}$
Δx	Path length	cm
ε	Absorbance	$L.mol^{-1}.cm^{-1}$
D	Mutual diffusion coefficient	$m^2.s^{-1}$
θ	Dynamic contact angle	°
γ	Air-liquid surface tension	$mN.m^{-1}$

E_t	Total energy of microchannel	
t	Time	S
μ	Fluid viscosity	mPa.s
h	Microchannel depth	μm
w	Microchannel width	μm
x	Penetration distance	mm
P	Pressure	Pa
r	Hydraulic radius	μm
V_x	Penetration velocity	$mm.s^{-1}$
λ	wavelength of radius variation	μm
ΔP_{ca}	Capillary pressure	Pa

Subscripts

m	mixing
d	dispersion
p	polar
h	hydrogen
hex	hexane
bit	bitumen

exp	experimental
calc	calculated
s	solid
l	liquid
g	gas
ca	capillary
pen	pentane

Abbreviations

SAGD	Steam Assisted Gravity Drainage
PDMS	Polydimethylsiloxane
HIM	Helium Ion Microscopy
AIE	International Energy Agency
BP	British Petroleum
LED	Light Emitting Diode
VAPEX	Vapor Extraction
PMMA	Poly(methyl methacrylate)
UV-VIS	Ultraviolet–Visible Spectrophotometry
TIRF	Total Internal Reflection Fluorescence
PFOCTS	Trichloro(1h 1h 2h 2h-perfluorooctyl)silane

CCD	Charge Couple Device
NMR	Nuclear Magnetic Resonance
HF	Hydrofluoric acid
AARD	Average Absolute Relative Deviation
HMDS	Hexamethyldisilazane
CVD	Chemical Vapor Deposition
N-Solv	Enhanced solvent extraction
AxSET	Axial Super-Resolution Evanescent-wave Tomography
ASTM	American Society of Testing Materials
SEM	Scanning Electron Microscope
LASER	Liquid Addition to Steam for Enhanced Recovery

Chapter 1: General Introduction

1.1. Background

World energy demand along with limited conventional oil resources, are bringing more attempts to find potential resources and transform them into commercial field. Exploration and research on alternative sources are environmentally important but the reality is that fossil fuels with higher energy efficiency are still cheaper than other alternatives. Since oil demand continues to rise, the world is turning towards discovery of less accessible unconventional reserves like bitumen and heavy oil [1]. Canada has over 1.8 trillion barrels of heavy oil and bitumen, representing 11% of the world's oil reserves [2]. Unconventional oil has different properties compared with light oils [3] and the main difference is their high viscosity ranging from 1×10^5 cP to 1×10^9 cP [4] that challenges production and transportation [5]. The success of in-situ heavy oil extraction methods depends on viscosity reduction of the bitumen as well as pumping up the recovered bitumen. Viscosity reduction is possible by thermal process, mass transfer, and molecular scission methods. These resources require different recovery methods compared with conventional ones. Steam-Assisted Gravity Drainage (SAGD) is the most commonly used thermal recovery technique. However, high energy consumption of steam formation and CO_2 emission are the main disadvantages of this method [6] which lead to research for alternative methods.

Butler suggested a new recovery method analogue of SAGD based on solvent injection and dilution instead of heating for viscosity reduction [7]. Mass transfer is the main phenomenon by diffusing the molecules of solvent into the bitumen. There is no water required with in-situ upgrading of bitumen (i.e. deasphalting of bitumen) and high level of solvent recovery [8].

Despite the benefits of solvent-based methods, molecular diffusion of solvent into bitumen is extremely slow and making this technique not suitable for field application yet. Moreover, the hydrocarbon solvents and transportation to the well location is expensive and selection of appropriate solvent plays a key role in economic viability of the process. Since diffusion is a molecular-scale phenomenon, it is believed that macro-scale performance of solvent-based techniques is largely affected by micro-scale understanding of involved mechanisms. Microfluidics are compatible with visualization techniques and can provide direct evidence of the solvent mass transfer in bitumen and pore-scale events associated with solvent-based extraction methods.

1.2. Objectives

The first objective of this thesis focuses on the diffusion mechanism identification in bitumen hexane binary system in presence of precipitated asphaltene. Proposing a fast and cheap technique to estimate constant and concentration dependent diffusion coefficients and comparison with macro-scale diffusion coefficients is the next topic of study.

The second objective is to study the capillary flow of diluted bitumen in microchannel with different surface wettability and to understand the effective parameters on deviation between experimental and theoretical predictions.

The third objective is pore-scale investigation of asphaltene precipitation and deposition. Effect of n-alkane solvents on asphaltene particle morphology, viscosity of bitumen and formation damage is also evaluated.

1.3. Structure of Thesis

The application of microfluidic platforms in solvent-based extraction methods and related topics are studied in this work. In the current chapter, a general overview of the thesis along with thesis motivation and overview have been laid out. Chapter 2 is a review of application of microfluidics in energy division. In chapter 3, suitable material for micromodel fabrication was selected. Chapter 4 is about solvent diffusion in bitumen with focus on diffusion coefficient measurement. Capillary flow of pure liquids as well as bitumen was evaluated in chapter 5. Pore-scale study of asphaltene precipitation and deposition is discussed in chapter 6. The brief highlights of each chapter are presented in the following:

- Chapter Two: This chapter is an overview of current application of micro and nanofluidics in energy sector and its future potential regarding the limitation of present energy resources. Renewable energies and fossil fuel are generally reviewed and more details of microfluidics in heavy oil and bitumen recovery are explained. A review on potential materials to fabricate microdevices is explained.

- Chapter Three: The possibility of using Polydimethylsiloxane (PDMS) Micromodel in heavy oil and bitumen related studies is evaluated here. Dynamic of swelling ratio for PDMS in different solvents and bitumen along with transparency of swelled PDMS were evaluated. Moreover, effect of surface coating on solvent and bitumen resistivity and compatibility of PDMS was also studied.

- Chapter Four: The glass micromodel is used to study diffusion of hexane into bitumen and experimental results are compared with x-ray scanning approach as a macro-scale method. Diffusion mass transfer mechanisms were evaluated and suitable mechanism was used to calculate constant and concentration dependent diffusion coefficient.

- Chapter Five: According to chapter 4, asphaltene precipitation and diluted of bitumen are two important effects of solvent diffusion in bitumen. Therefore, capillary-driven flow of pure liquids and diluted bitumen in straight and periodiccaly constricted microchannels is studied in this chapter. Effects of hydrophilic and hydrophobic surfaces on fluid flow, dynamic contact angle and flow velocity was experimentally investigated and compared with theoretical model.

- Chapter six: In this chapter, asphaltene precipitation and deposition, as the second issue with solvent diffusion in bitumen, is studied. 2D microchannels with two patterns and surface wettability were used and morphology of precipitated asphaltene was evaluated using HIM analysis and 3D reconstruction.

- Chapter Seven: A brief summary of the outcome of the research in this thesis and recommendations for future work are presented in this chapter.

References

[1] L. A. James, Mass Transfer Mechanisms during the Solvent Recovery of Heavy Oil (Doctoral dissertation), Waterloo: Retrieved from ProQuest Dissertations & Theses Global, 2009.

[2] Oil and Gas Journal, Alberta Energy Regulator and Canadian Association of Petroleum Producers, 2015.

[3] O. V. Trevisan, A. C. L. Lisboa, F. A. França and W. Trindade, "Oil production in offshore fields: An overview of the Brazilian technology development," in World Heavy Oil Conference, Pequim, 2006.

[4] A. K. Mehrotra, "A model for the viscosity of bitumen/bitumen fractions-diluent blends," Journal of Canadian Petroleum Technology, vol. 31, no. 9, pp. 28-32, 1992.

[5] R. M. Butler, Thermal Recovery of Oil and Bitumen, Englewood Cliffs, NJ: Prentice Hall, 1991.

[6] M. Keshavarz, R. Okuno and T. Babadagli, "Efficient oil displacement near the chamber edge in ES-SAGD," Journal of Petroleum Science and Engineering, vol. 118, pp. 99-113, 2014.

[7] R. M. Butler and I. J. Mokrys, "Recovery of Heavy Oils Using Vaporized Hydrocarbon Solvents: Further Development of the VAPEX Process," in etroleum Conference of The South Saskatchewan, Regina, 1992.

[8] R. Luhning, S. Das, L. Fisher, J. Bakker, J. Grabowski, J. Engleman, S. Wong, L. Sullivan and H. Boyle, "Full Scale VAPEX Process-Climate Change Advantage and Economic Consequences," Journal of Canadian Petroleum Technology, vol. 42, no. 2, pp. 31-34, 2003.

Chapter 2: Micro/Nanofluidcs in Energy Application

2.1. Introduction

Our use of energy has been increasing since the industrial revolution in the eighteenth century and is expected to continue increasing for the next two decades according to International Energy Agency (IEA). Access to clean and reliable energy resources is not only a present challenge, but also one of the main concerns for future generations. According to British Petroleum (BP) Statistical Review of World Energy [1], 67% of global energy sources are fossil fuel, 27% from hydro and nuclear, and 6% from renewables such as wind and solar. Although advancement of sustainable and renewable alternative energies is critically important, change in global energy systems is very slow with a time-scale of 50 to 100 years [2] to replace and infiltrate the energy supply. Therefore, fossil fuels are still the main energy resources since they are more energy efficient and abundant, comparatively.

Although there exists a limited amount of fossil fuels, non-of the predictions [3] regarding the end point of these resources have come true due to the technological advances in both upstream and downstream sections. One of the main progresses is related to measurement instruments and accurate pilots and simulations. However, most of the experiments are conducted with massive equipment and long running time. As an example, knowledge of thermodynamic properties like minimum miscibility pressure is crucial for production estimation in CO_2 enhanced oil recovery method. Present measurement methods such as slim tube test [4] are costly and take a few days and simulation methods [5] without pairing with experimental data set can have significant error. Considering all the challenges in macro-scale world, we can move to small-scale named as “microfluidics” with growing application in engineering, health

and life science. In fact, there are various challenges in oil and gas recovery, underground water resources, biomolecules detection, targeted drug delivery, and energy conversion involve in micro and nano-scale phenomena.

With the advances in micro-technologies during the last two decades, accurate, cheap and reliable information in extremely lower time is achieved. Nguyen et al. [6] mentioned a microfluidic approach for CO_2 in oil minimum miscible pressure measurement and compared the results with well-known macro-methods. They obtained the results in 30 minutes and analyzed the results benefiting the inherent fluorescent nature of oil. In another work [7], CO_2 diffusion into bitumen was evaluated using a few nanoliter sample and a few minutes with high accuracy of data.

Generally, microfluidics is applicable in surface topics such as solar or electrochemical energies and in-situ operations related to carbon capture storage and oil extraction and multiphase flow in porous media. Noteworthy to mention that both micro and nano technologies miniaturize the small-scale processes but sometimes different topics and scope of study. For example, energy related nanotechnology is more focused on fuel and solar cells, lithium-ion batteries, and light emitting diode (LED). On the other side, microfluidics are mostly focused on fluidic challenges mainly involved in conventional (e.g. oil and gas) and renewable (e.g. hydro power) energy resources [2]. Global warming as the biggest environmental threat is directly related to carbon emission and microfluidic is among the pioneer methods to study CO_2 storage and its application in heavy oil extraction. Finally, size-scale of the microfluidic platforms is in the same length-scale of typical oil and gas porous media [8]. Application of microfluidics could be divided into three categories as briefly discussed below.

2.1.1. Microfluidics in Electrochemical Energy

Electrochemical energy conversion devices such as fuel cells and electrolyzers are the best example of scalable meso-scale process that can reach power conversion at megawatt-scale [9]. Fuel cells are the well-stablished systems among the other electrochemical microsystems with the focus on high energy density power sources that is supplied through the tiny hydrogen fuel cells [10]. In contrast to traditional fuel cells that used ion exchange membrane, microfluidic fuel cells take advantage of diffusion mixing between fuel and oxidant stream at low Reynolds number to produce electrical power in absence of membrane. Transport and reaction properties of fuel and oxidant are among the main challenges in development of microfluidic fuel cells [11]. Microfluidic designs with different flow combinations and electrode positions are represented in figure 2.1 [12].

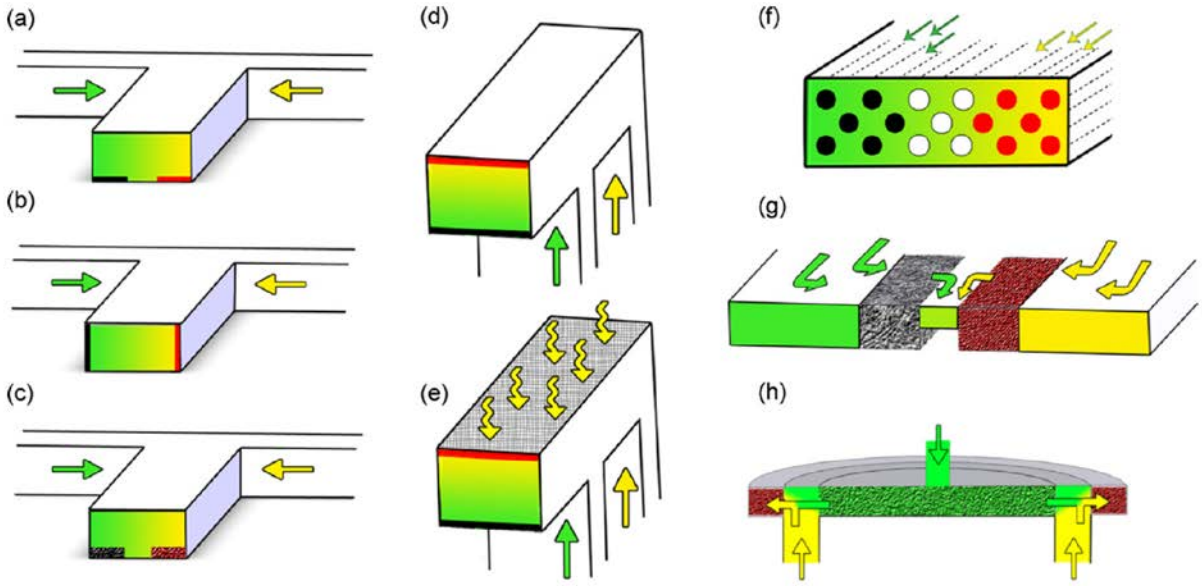

Figure 2.1. Schematic of microfluidic fuel cells with fuel in green, oxidant in yellow, cathodes in red and anodes in black. Green and yellow streams are combined in T-channels with different positions of electrodes (i.e. a, b, and c). F-channel (d) with air-breathing porous electrode (e). Electrode array (f), porous electrode (g) and radial porous electrode microfluidic fuel cell [12]. Reprinted with permission from Elsevier.

It seems future energy scenarios depends highly on storage of energy specially for renewable sources such as wind and solar power. Therefore, improvement of convection and diffusion of reactants and products as well as electrical charge transport can increase the energy conversion efficiency [9]. High energy conversion efficiency along with appropriate scale-up strategies could pave the way to large-scale energy storage.

2.1.2. Microfluidics in Renewable Energies

One of the sustainable and environmentally friendly alternative sources of fossil fuels is solar energy. Solar energy that arrives on the surface of the earth in one hour, is more than one year of global energy demand [13]. Although, storage and transport of the solar energy is a serious challenge, optofluidic that combines microfluidics and optics can improve the application of solar energy to drive chemical reactions such as solar-driven photocatalysis [14]. Photocatalytic microfluidic reactors provide highly accurate control of light and fluids with a large surface to volume ratio and controlled distribution of light onto the photocatalyst. Meng et al. [15] presented a novel microfluidic-based photocatalytic microreactor with nanofibrous TiO_2 as photocatalyst with a simple fabrication process. Produced nanofibrous TiO_2 were transferred and scaled between a PDMS mold and glass wafer and photocatalyst activity of the microreactor was evaluated with methylene blue photodegradation. High efficiency of nanofibrous TiO_2 microreactor was reported due to high surface to volume ratio of the porous structure. It seems

that tubular nanostructured TiO_2 photocatalysts present exciting opportunities to convert carbon dioxide and water vapor into hydrocarbon fuels using sunlight (figure 2.2) [16].

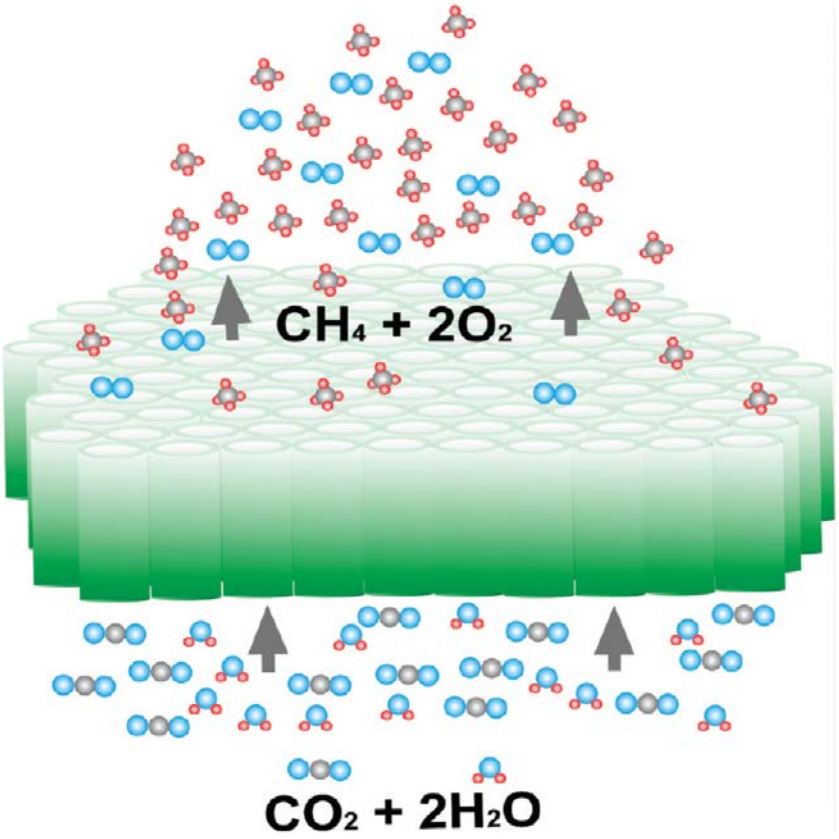

Figure 2.2. CO_2 conversion with flow-through photocatalytic membrane [16]. Reprinted with permission from American Chemical Society.

Hydroelectricity is a macro-scale technology and microfluidic studies has not been even close to possibility of scaleup in this field. However, environmental challenges of hydropower plants such as particulate sedimentation processes could be analyzed through the microfluidic platforms. Since hydropower is the potential energy of water to generate power, Sinton mentioned generated current in microchannel as a form of microfluidic hydropower [2]. According to this similarity, Haldrup et al. [17] reported a promising low-cost efficient

electrokinetic generator where electrokinetic energy conversion method can convert pressure into electric energy for micro-scale application.

2.1.3. Microfluidics in Fossil Fuel

Flow visualization in a scale matching with real-size porous media through the opaque, inaccessible underground reservoir has been always challenging but micromodels are simulating the porous rock structure and fluid flow is monitoring through the complicated structure with various surface properties. Microfluidic has a strong potential to study fundamental concepts of oil recovery such as capillarity, mixing, diffusion and convection, emulsions etc. since they are among the fundamental topics of interest in microfluidics too [18]. Micromodels provides a platform to miniaturize various applications in observation and characterization of oil and gas recovery mechanisms at reservoir-matched pressures and temperatures as well as modeling of fluid flow in porous media. Microfluidics has been used to evaluate minimum miscibility pressure [19], onset point of asphaltene precipitation [20], diffusion coefficient of solvent in heavy oil [21]. Buchgraber et al. [22] used silicon micromodel to study capillary and residual CO_2 trapping mechanisms. Effect of imbibing water flow rate on trapping mechanism was also evaluated. At lower flow rates, residual saturation was dominated while dissolution was dominated at high flow rates that represents flow near wellbore during the enhanced sequestration.

Moreover, microfluidic pressure/volume/temperature (PVT) platforms are introduced as a reliable and accurate measurement system. For example, measurement of volumetric properties as a function of pressure and temperature are essential in oil recovery enhancement and lifecycle

improvement of a reservoir [23]. Molla and Mostowfi [24] presented a novel micro-scale (PVT) cell with a long and narrow capillary (1 m long and total volume of 5 μL) to measure saturation pressure and phase-volume ratio by only a few microliters of oil sample as precise as laboratory-scale pressurized visual PVT cell.

2.2. Microfluidics and Unconventional Petroleum Resources

World energy demand along with limited conventional oil resources, are bringing more attempts to find potential resources and transform them into commercial field. Discoveries lead to find unconventional resources like bitumen and heavy oil with different properties compared with light oils [25]. Their main challenge is viscosity reduction for extraction and transportation [26]. There are different heavy oil and bitumen recovery methods including miscible displacement, chemical flooding and thermal recoveries. SAGD is the most well-known thermal technique, taking the advantages of temperature dependency of heavy oil viscosity. Butler suggested a new recovery method analogue of SAGD based on solvent injection and dilution to reduce the viscosity of heavy oil [27].

Time scale of gravity drainage is extremely smaller than diffusion mechanism of solvent into bitumen. Therefore, low rate of oil production is the major barrier toward commercialization of solvent-based methods. Solvent-based methods such as VAPEX involve injecting a solvent into the reservoir via upper horizontal well (injector). Solvent diffuses into the heavy oil and mobilized oil drained into the production well by the resultant action of gravitational and capillary forces. A typical representation of thermal or solvent recovery method is shown in figure 2.3 [28].

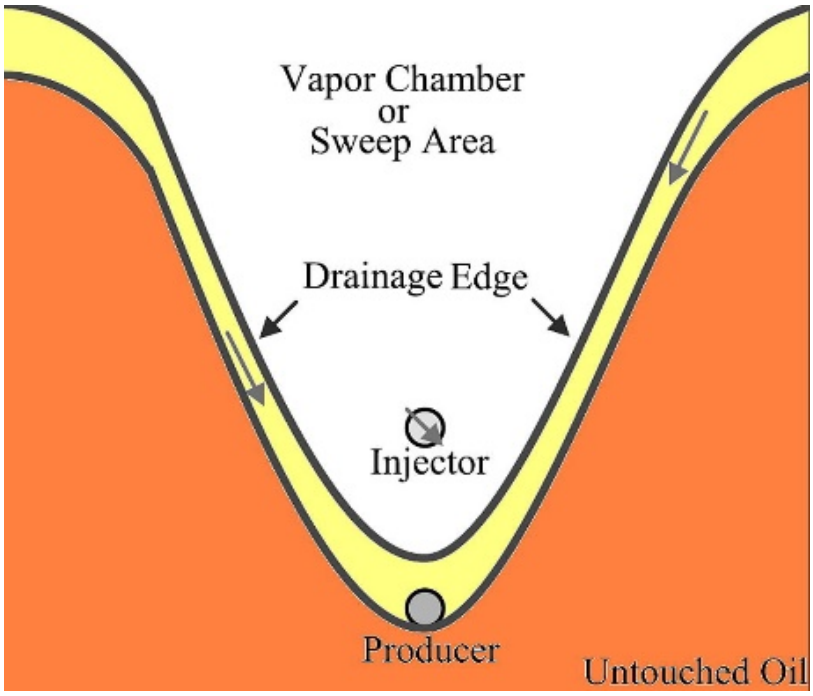

Figure 2.3. Cross sectional view of solvent injection into the injection well and diluted bitumen drained toward the production well [28]. Reprinted with permission from Elsevier.

VAPEX starts with establishing a communication between the injection and production wells (figure 2.4.a). Solvent chamber grows upward to the top of the reservoir and lateral spreading in chamber rising phase (figure 2.4.b and 2.4.c) [29]. The height of the oil filled pores decreasing when the solvent reaches the extend of the oil formation known as falling phase (figure 2.4.d). In the past few years, various modifications have been proposed to VAPEX process such as Steam Alternating Solvent (SAS), Expanding Solvent-SAGD (ES-SAGD) [30], Cyclic Solvent Injection (CSI) [31], N-solv [32], and LASER [33]. Because of abrupt solvent concentration profile at the interface of bitumen-solvent, molecular diffusion mass transfer take places as the dominant viscosity reduction mechanism. Diffusion of solvent into the bitumen leads to the formation of a thin film of live oil phase as represented in figure 2.5. Porous media is divided

into three sections of solvent chamber (dark blue), the live oil mobilized region (light blue), and the bitumen filled pores (gray).

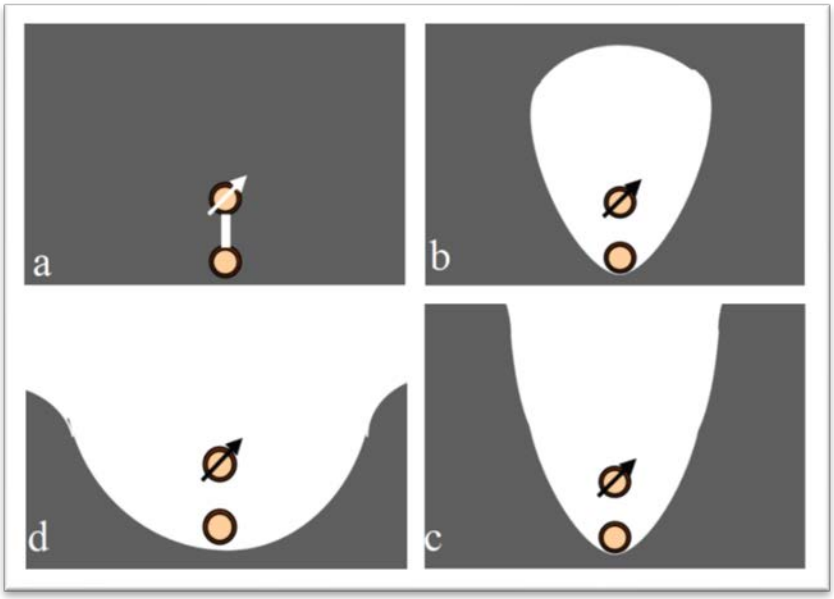

Figure 2.4. Stages of VAPEX process. Reproduced from ref. 29.

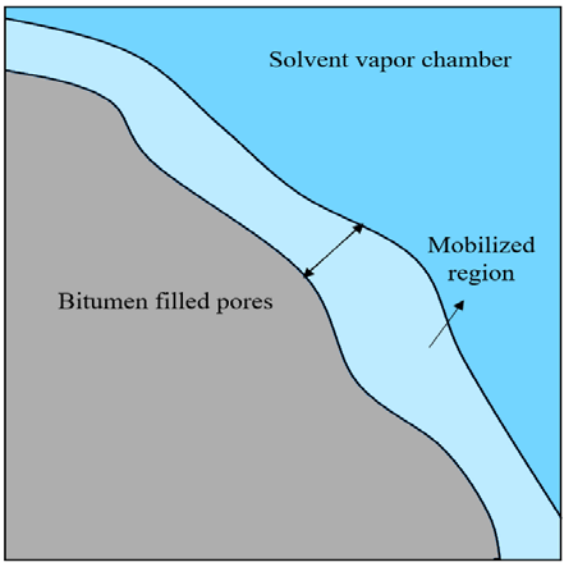

Figure 2.5. Solvent-bitumen interface

In the case of pure solvent, the concentration of vapor chamber is around 100%. Vapor solvent condenses if the pressure increases over the vapor pressure at the temperature of supply solvent. The maximum pressure is the solvent's vapor pressure at the supply temperature. The solvent concentration decreases toward the solvent-bitumen interface where it diffuses into the oil as shown in figure 2.6. There is a portion in mobilized region which the viscosity is sufficiently reduced to mobilize the oil under the gravity forces.

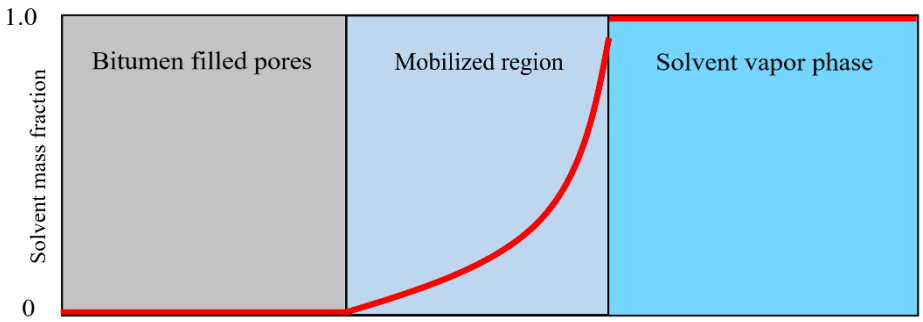

Figure 2.6. Schematic solvent concentration profile across the VAPEX process.

Diffusion of solvent into the bitumen corresponds to two important phenomena of heavy oil dilution and de-asphalting. The de-asphalting process of the bitumen during the solvent-based heavy oil recovery upgrades the bitumen in-situ and reduces the operating and environmental cost of upgrading. However, it may reduce the permeability, oil production rate, and the sweep efficiency of the heavy oil extraction. The precipitated asphaltene may block the pores throats and pore bodies and eliminating of fluid flow near the blocked region.

Researches into SAGD and VAPEX methods has mostly related to simulations, core and sand-pack flooding studies [34] that are limited with visualization of the phenomena inside the porous media [35] and control of the experimental condition. Macro-scale performance of these combined techniques is largely affected by pore-level understanding of involved mechanisms.

However, precise mechanisms of oil recovery at micro-scale in porous media in unconventional reservoirs are not well understood. Microfluidic provides a platform for direct observation and characterization of heavy oil upstream sector such as different extraction methods (e.g. SAGD and VAPEX) and downstream sector (i.e. refining of petroleum crude) with accurate quantification of fluid phase dynamic and chemistry properties [2].

De Hass et al. [36] developed a microfluidic network, “steam-on-a-chip”, to study SAGD extraction process in a real-time and compare oil recovery efficiency using steam and steam with alkaline additives. Fluorescent nature of the bitumen provides high resolution to quantify fluid phase dynamic under real reservoir condition and pore size. Glass micromodels were etched in depth of 56 μm and 65 μm to provide 67.7% and 72.5% porosities, respectively. Steam propagation was recorded using microscope and high-speed camera and corresponding recovery efficiency of alkaline steam additive was ~50% higher than pure steam. This was a successful example of how lab-on-a-chip method can help to study an energy intensive oil recovery method by potential alternatives. Qi et al. [37] designed a series of high-temperature and high-pressure micromodels to study the pore-scale behavior of condensing solvent bitumen extraction process. In this method, solvent vapor is injected at the elevated temperature and pressure and condenses at the bitumen interface. In fact, hot solvent transfers latent heat and condensed solvent dilutes the bitumen through the diffusion and mass transfer [38]. They reported three distinct regions of vapor solvent chamber, condensing edge, and liquid solvent zones were identified with specific features. Combination of bitumen dilution and vapor fingering at condensing edge resulted in highest bitumen recovery at this zone. High asphaltene deposition rate was recorded for liquid solvent zone due to lower fluorescent intensity that showed pore clogging and blockage for liquid solvent rather than solvent vapor.

There are several important pore-level phenomena such as fluid mixing, solvent mass transfer and local dilution effects, and immiscible displacement of mobile oil by steam and water condensate. Etched glass micromodel provides visualization of mass transfer and interaction of mass transfer and mixing along with gravity force to advance the interface in solvent and hybrid injection processes. An important practical advantage of miniaturization in the mentioned processes is that microfluidic channels can go to high temperature and pressures with less complication compared to macro–scale devices [39].

Oil transportation by pipeline is one of the main challenges associated with heavy oil and bitumen. Microfluidics is a strong platform for a variety of reservoir fluid characterization such as interfacial properties [39], phase behavior [40] and fluid composition [41]. Asphaltene precipitation disrupts the heavy oil extraction, transportation in pipelines and refineries. Microfluidic platform offers a timely characterization of asphaltene behavior in up and downstream sectors [42]. Asphaltene stability is highly dependent on composition and solubility power of the asphaltene in bulk oil changing at in-situ solvent injection processes or mixing of different crudes in wellbores, pipelines, and at refineries [42]. In addition, Pressure depletion can destabilize the saphaltene content mostly in wellbore tubulars [43]. Considering the small amount of oil sample in microfluidic devices, they are suitable for performing deposition test with a large number of necessary pore volume throughputs to simulate the near-wellbore region that is impossible by conventional core flooding experiments [44].

2.2.1. Potential Microfluidic Devices for Heavy Oil and Bitumen

In previous sections, application of microfluidic platforms in various fields of energy was reviewed. Depending on the application, microfluidic devices can be fabricated from glass, polymers such as PDMS and Poly(methyl methacrylate) (PMMA), ceramic, Teflon, paper, etc. [45]. Each one applies in a field of science depending on the ease of prototyping and performance of the platform [45]. Surface properties such as roughness or hydrophilicity of the device are extremely amplified compared with macro-scale that can enable specific function or causes errors. For example, velocity calculation in microchannel is largely affected by contact angle of the liquid on the walls and contact angle could be unstable and variable due to the surface inhomogeneity or roughness. Glass and Polydimethylsiloxane (PDMS) are two widely used materials in microfluidics that are briefly discussed below.

2.2.1.1. Glass Micromodel

Glass with photolithography procedure for fabrication [46], was the first microfluidic fabrication material with unique features such as high resistivity toward temperature, pressure and suitable for solvent-involved applications. Optical transparency and thermostability along with solvent compatibility makes glass pioneer in micro-reactors [47], rheology study [48], solvent extraction [49], droplet formation [50], etc. Glass microfluidics has disadvantages such as high cost of fabrication with dangerous chemicals such as HF involved in etching, and high temperature and super-clean environment for bonding [51]. The limitations motivate us for finding a replacement before conducting the bitumen related studies.

2.2.1.2. Polymeric Micromodel

Polymer is the most-commonly fabrication material with inexpensive and fast fabrication process. For example, PDMS as the most popular material of polymer's group has a low curing temperature (40 to 70 °C) and easily seals to glass or PDMS in confined micro-structures. PDMS is gas permeable and compatible for cell cultivation and is widely used in bioengineering and biomedical studies [52]. However, porous structure of the PDMS surface, makes it incompatible with organic solvents. Considering the PDMS advantages over the glass, the possibility of PDMS application in pore-scale study of heavy oil and bitumen is evaluated in the next chapter using untreated and silane-treated PDMS microchannel.

References

[1] BP, "BP Statistical Review of World Energy," http://bp.com/statisticalreview2016, 2017. [Online].

[2] D. Sinton, "Energy: the microfluidic frontier," Lab on a Chip, vol. 14, p. 3127, 2014.

[3] C. J. Campbell and J. H. Laherr`ere, "The end of cheap oil," Scientific American, 1998.

[5] J.-N. Jaubert, L. Avaullee and J.-F. Souvay, "A crude oil data bank containing more than 5000 PVT and gas injection data," Journal of Petroleum Science and Engineering, vol. 34, no. 1-4, pp. 65-107, 2002.

[6] P. Nguyen, D. Mohaddes, J. Riordon, H. Fadaei, P. Lele and D. Sinton, "Fast Fluorescence-Based Microfluidic Method for Measuring Minimum Miscibility Pressure of CO_2 in Crude Oils," Analytical Chemistry, vol. 87, pp. 3160-3164, 2015.

[7] H. Fadaei, B. Scarff and D. Sinton, "Rapid Microfluidics-Based Measurement of CO_2 Diffusivity in Bitumen," Energy & Fuels, pp. 4829-4835, 2011.

[8] C. A. Conn, K. Ma, G. J. Hirasaki and S. L. Biswal, "Visualizing oil displacement with foam in a microfluidic device with permeability contrast," Lab on a Chip, vol. 14, no. 20, pp. 3968-77, 2014.

[9] M. A. Modestino, D. F. Rivas, S. M. H. Hashemi, J. G. E. Gardeniers and D. Psaltis, "The potential for microfluidics in electrochemical energy systems," Energy & Environmental Science , vol. 9, p. 3381, 2016.

[10] P. P. Edwards, V. L. Kuznetsov, W. I. F. David and N. P. Brandon, "Hydrogen and fuel cells: Towards a sustainable energy future," Energy Policy, vol. 36, no. 12, pp. 4356-4362, 2008.

[11] J. Lee, K. G. Lim, G. T. R. Palmore and A. Tripathi, "Optimization of Microfluidic Fuel Cells Using Transport Principles," Analytical Chemistry, vol. 79, pp. 7301-7307, 2007.

[12] E. Kjeang, N. Djilali and D. Sinton, "Microfluidic fuel cells: A review," Journal of Power Sources, vol. 186, p. 353–369, 2009.

[13] O. Morton, "Solar energy: A new day dawning?: Silicon Valley sunrise," Nature, vol. 443, pp. 19-22, 2006.

[14] S. S. Ahsan, A. Gumus and D. Erickson, "Redox mediated photocatalytic water-splitting in optofluidic microreactors," Lab on a Chip, vol. 13, p. 409, 2013.

[15] Z. Meng, X. Zhang and J. Qin, "A high efficiency microfluidic-based photocatalytic microreactor using electrospun nanofibrous TiO2 as a photocatalyst," Nanoscale, vol. 5, no. 11, pp. 4687-4690, 2013.

[16] S. C. Roy, O. K. Varghese, M. Paulose and C. A. Grimes, "Toward Solar Fuels: Photocatalytic Conversion of Carbon Dioxide to Hydrocarbons," ACS Nano, vol. 4, no. 3, p. 1259–127, 2010.

[17] S. Haldrup, J. Catalano, M. R. Hansen, M. Wagner, G. V. Jensen, J. S. Pedersen and A. Bentien, "High Electrokinetic Energy Conversion Efficiency in Charged Nanoporous Nitrocellulose/Sulfonated Polystyrene Membranes," Nano Letters, vol. 15, pp. 1158-1165, 2015.

[18] V. A. Lifton, "Microfluidics: an enabling screening technology for enhanced oil recovery (EOR)," Lab on a Chip, vol. 16, p. 1777, 2016.

[19] P. Nguyen, D. Mohaddes, J. Riordon, H. Fadaei, P. Lele and D. Sinton, "Fast fluorescence-based microfluidic method for measuring minimum miscibility pressure of CO_2 in crude oils," Analytical Chemistry, vol. 87, no. 6, p. 3160–3164, 2015.

[20] M. H. Schneider, V. J. Sieben, A. M. Kharrat and F. Mostowfi, "Measurement of asphaltenes using optical spectroscopy on a microfluidic platform," Analytical Chemistry, vol. 85, p. 5153–5160, 2013.

[21] S. G. R. Lefortier, P. J. Hamersma, A. Bardow and M. T. Kreutzer, "Rapid microfluidic screening of CO_2 solubility and diffusion in pure and mixed solvents," Lab on a Chip, vol. 12, no. 18, pp. 3387-3391, 2012.

[22] M. Buchgraber, A. R. Kovscek and L. M. Castanier, "A study of microscale gas trapping using etched silicon micromodels," Transport Porous Media, vol. 95, no. 3, pp. 647-668, 2012.

[23] A. Danesh, PVT and phase behavior of petroleum reservoir fluids, ElsevierScience, 1998.

[24] S. Molla and F. Mostowfi, "Microfluidic PVT-saturation pressure and phase -volume measurement of black oil," in SPE Annual Technical Conference and Exhibition, Amsterdam, 2014.

[25] O. V. Trevisan, A. C. L. Lisboa, F. A. França and W. Trindade, "Oil production in offshore fields: An overview of the Brazilian technology development," in World Heavy Oil Conference, Pequim, 2006.

[26] R. M. Butler, Thermal Recovery of Oil and Bitumen, Englewood Cliffs, NJ: Prentice Hall, 1991.

[27] R. M. Butler and I. J. Mokrys, "Recovery of heavy oils using vaporized hydrocarbon solvents: further development of the VAPEX process," in Technical Meeting / Petroleum Conference of The South Saskatchewan Section, Regina, 1992.

[28] K. Pourabdollah, B. Mokhtari, "The VAPEX Process, from beginning up to date," Fuel, vol. 107, pp. 1-33, 2013.

[29] O. Mohammadzadeh Shanehsaz, "Experimental Studies Focused on the Pore-Scale Aspects of Heavy Oil and Bitumen Recovery Using the Steam Assisted Gravity Drainage (SAGD) and Solvent-Aided SAGD (SA-SAGD) Recovery Processes," University of Waterloo, Waterloo, Ontario, Canada, 2012.

[30] T. Nasr, G. Beaulieu, H. Golbeck, G. Heck, “Novel expanding solvent-SAGD process “ES-SAGD,” Journal of Canadian Petroleum Technology, vol. 42, 2003.

[31] G. B. Lim, P. R. Kry, J. P. Lebel, M. Y. Kwan, “Cyclic solvent process for in-situ bitumen and heavy oil production,” Patent CA2349234, 2004.

[32] J. Nenniger, E. Nenniger, “Method and apparatus for stimulating heavy oil production,” Patent CA2567399C.

[33] R. Leaute, “Liquid addition to steam for enhancing recovery (LASER) of bitumen with CSS: Evolution of technology from research concept to a field pilot at Cold Lake,” SPE International Thermal Operations and Heavy Oil Symposium, Calgary, Canada, 2002.

[34] F. Torabi, B. Yadali Jamaloei, B. M. Stengler and D. E. Jackson, "The evaluation of CO_2 based vapour extraction (VAPEX) process for heavy-oil recovery," Journal of Petroleum Exploration and Production Technology, vol. 2, pp. 93-105, 2012.

[35] G. Q. Wu, A. Kantzas and D. Salama, "Computed tomography study of VAPEX process in laboratory 3D model," Journal of Canadian Petroleum Technology, vol. 49, pp. 40-47, 2010.

[36] T. W. de Haas, H. Fadaei, U. Guerrerob and D. Sinton, "Steam-on-a-chip for oil recovery: the role of alkaline additives in steam assisted gravity drainage," Lab on a Chip, vol. 13, pp. 3832-3839, 2013.

[37] Z. Qi, A. Abedini, P. Lele, N. Mosavat, A. Guerrero and D. Sinton, "Pore-scale analysis of condensing solvent bitumen extraction," Fuel, vol. 193, p. 284–293, 2017.

[38] L. A. James, N. Rezaei and I. Chatzis, "VAPEX, warm VAPEX and hybrid VAPEX – the state of enhanced oil recovery for in situ heavy oils in canada," Journal of Canadaian Petroleum Technology, vol. 47, no. 4, 2008.

[39] F. Mostowfi, J. Czarnecki, J. Masliyah and S. A. Bhattacharjee, "microfluidic electrochemical detection technique for assessing stability of thin films and emulsions," Journal of Colloidal Interface Science, vol. 317, no. 2, pp. 593-603, 2008.

[40] B. Bao, J. Riordon, F. Mostowfi and D. Sinton, "Microfluidic and nanofluidic phase behaviour characterization for industrial CO_2, oil and gas," Lab on a Chip, vol. 17, pp. 2740-2759, 2017.

[41] M. K. Shah, R. Fisher, I. Hassan, E. Makarov, O. Medvedev and A. Memon, "Measuring Reservoir Fluid Composition Using a Novel Continuous Contact Flash Method Based on a Microfluidic Device," in Abu Dhabi International Petroleum Exhibition and Conference, Abu Dhabi, UAE, 2015.

[42] V. J. Sieben, A. K. Tharanivasan, S. I. Andersen and F. Mostowfi, "Microfluidic approach for evaluating the solubility of crude oil asphaltenes," Energy & Fuels, vol. 30, p. 1933−1946, 2016.

[43] A. Hammami, C. H. Phelps, T. Monger-McClure and T. M. Little, "Asphaltene precipitation from live oils: an experimental investigation of onset conditions and reversibility," Energy & Fuels, vol. 14, pp. 14-18, 2000.

[44] M. Tavakkoli, P. He, P.-H. Lin, S. Rezaee, M. Puerto, R. Doherty, J. Creek, S. L. Biswal and F. M. Vargas, "Asphaltene deposition and fouling in reservoirs," in Offshore Technology Conference, Houston, Texas, USA, 2017.

[45] K. Ren, J. Zhou and H. Wu, "Materials for Microfluidic Chip Fabrication," Accounts of Chemical Research, vol. 46, no. 11, pp. 2396-2406, 2012.

[46] C. H. Lin, G. B. Lee, Y. H. Lin and G. L. Chang, "A fast prototyping process for fabrication of microfluidic systems on soda-lime glass," Journal of Micromechanics and Microengineering, vol. 11, pp. 726-732, 2001.

[47] S. K. Yap, W. K. Wong, N. X. Y. Ng and S. A. Khan, "Three-phase microfluidic reactor networks – Design, modeling and application to scaled-out nanoparticle-catalyzed hydrogenations with online catalyst recovery and recycle," Chemical Engineering Science, vol. 169, pp. 117-127, 2017.

[48] K. Keshmiri, S. Mozaffari, P. Tchoukov, H. Huang and N. Nazemifard, "Using Microfluidic Device to Study Rheological Properties of Heavy Oil," in AIChE Annual Meeting, San Francisco, 2016.

[49] D. Ciceri, J. M. Perera and G. W. Stevens, "The use of microfluidic devices in solvent extraction," Journal of Chemical Technology and Biotechnology, vol. 89, p. 771–786, 2014.

[50] M. Saqib, O. B. Şahinoğlu and E. Y. Erdem, "Alternating droplet formation by using tapered channel geometry," Scientific Reports, vol. 8, p. 1606, 2018.

[51] K. Ren, J. Zhou and H. Wu, "Materials for Microfluidic Chip Fabrication," Accounts of Chemical Research, vol. 46, no. 11, pp. 2396-2406, 2013.

[52] K. Ren and R. N. Zare, "Chemical Recognition in Cell-Imprinted Polymers," ACS Nano, vol. 6, pp. 4314-4318, 2012.

Chapter 3: Polydimethylsiloxane (PDMS) Micromodel

As discussed in chapter 2, the possibility of PDMS microchannel application in heavy oil and bitumen is studied here. It is believed that working with PDMS microchannel saves time and cost of fabrication compared with glass microchannel. In addition, resistivity improvement of PDMS microchannel coated with silane will be evaluated in this chapter.

3.1. Introduction

Microfluidic devices have been applied in energy sector [1-3], single [4] and multiphase flow study [5], fuel cells [6], microbioreactors [7], enhanced oil recovery [8, 9], evaluation of wetting properties [10], etc. Glass was the main substrate for fabrication of microchannel early in the 1990s due to its mechanical and optical properties, low chemical reactivity, and transparency. Microchannels are fabricated by photolithography and wet etching methods [11]. However, disadvantages of glass microchannel are high price, multistage fabrication process, and irreproducible thermal bonding of glass substrates [12]. Poly(dimethylsiloxane) (PDMS) is one of the most popular materials for microfluidic fabrication that has been thoroughly studied in various fields of application [13-15]. PDMS microchannels with low polarity and chemical inertness can be fabricated easily and at low cost [16-18]. Microchannels are transparent to visible light and therefore suitable for detection systems like Ultraviolet–Visible Spectrophotometry (UV-VIS) spectroscopy and fluorescence [19]. PDMS consists of an elastomer base and a curing agent. A main drawback of using PDMS microchannel to extract bitumen is that PDMS swells with solvents such as toluene and low molecular weight organic

A version of this chapter has been submitted to the Journal of Petroleum Science and Technology and is under review for publication.

solutes. In addition, bitumen is a complicated material and large molecules in bitumen (e.g., asphaltene) can affect the swelling of microchannel [23]. Swelling deforms the microchannel and changes the rate and profile of fluid flow, which decreases the accuracy of data capture in bitumen extraction measurements. However, if the PDMS swelling ratio is slow, it can be used as a cheap and easily-made choice for micro-scale studies where contacting time between PDMS and bitumen is shorter than swelling rate.

Numbers of surface modification methods are available to improve the solvent compatibility of the PDMS. Abate et al. [24] presented a coating technique with a glass-like layer using sol-gel chemistry. It increased chemical resistance of the channel but it changed the dimensions of the designed microchannel. Also, Coating of the surface with other materials like Teflon [25] and silane [26] are reported by other authors. Laser surface modification [27] is another method to adjust the surface but considering this technique, PDMS is not a cheap and fast method of microfluidic device fabrication anymore. Application of self-assembled monolayer (SAM) with a high number of CF_3 and CF_2 groups alter the wettability of the surface [28]. Presence of these functional groups on the surface of trichloro(1h 1h 2h 2h-perfluorooctyl)silane (PFOCTS) coated PDMS has been reported by other authors [28]. There are a few limitations on PDMS surface treatment such as aggregation of fluorocarbon and surface structural defect that impacts on coating performance [29].

In this study, dynamic of swelling ratio for PDMS in pure solvents and diluted bitumen samples (%10 to %50) in small time-lapsed increments were measured and transparency of swelled PDMS as a function of time was evaluated using UV-VIS. Total Internal Reflection Fluorescence (TIRF) microscopy was also applied to detect the bitumen on PDMS samples due to the fluorescence nature of the bitumen [30]. Moreover, PDMS slabs were coated with

PFOCTS in order to evaluate the effect of silane coating on solvent and bitumen compatibility of PDMS.

3.2. Theory

Solubility parameter can correlate experimental swelling rates based on cohesive energy densities of the materials. Two materials are soluble with similar cohesive energies. In fact, cohesive energy of the solute must be overcome to allow solvent molecules to insert [16]. Therefore, solubility parameter is useful for predicting the swelling behavior of a polymer in a solvent without knowing any other information about the solvent [16]. For a binary system the Hildebrand-Scatchard equation [31] relates the solubility parameters of non-polar liquids to the enthalpy change on mixing them:

$$\Delta H_m = V_m(\delta_1 - \delta_2)^2 \emptyset_1 \emptyset_2 \qquad (3-1)$$

Where V_m is the volume of the mixture, δ_i is the solubility parameter of the component i, and $\emptyset_i$ is the volume fraction of i in the mixture. For a soluble binary system, the free energy of mixing must be less than zero [32]. Based on the energy, enthalpy, and entropy of mixing ($\Delta G_m = \Delta H_m - T\Delta S_m$), and Hildebrand-Scatchard equation ($\Delta H_m \infty (\delta_{pd} - \delta_s)^2$), swelling is maximal when $(\delta_p - \delta_s)^2$ is zero or solubility parameter of PDMS (δ_{pd}) and solubility parameter of solvent (δ_s) are similar [31]. However, there are some exceptions for maximal swelling because of other effective factors such as polarity of the solvent [33]. Hansen [34] divided solubility parameter into dispersion forces (δ_d), polar forces (δ_p), and hydrogen bonding forces (δ_h) within the material (Eq. 3-2). The role of each force parameter can affect the strength of the solubility of two solvents with the same solubility parameter.

$$\delta^2 = \delta_d^2 + \delta_p^2 + \delta_h^2 \qquad (3-2)$$

Su et al [35] showed that polar interaction is the main effect for deciding the swelling degree of PDMS in water and alcohol. This is in good agreement with our results, because hexane and toluene with the highest swelling ratio had polar force factor close to PDMS. Lee et al. [16] reported an indistinguishable solubility parameter of 9.9 $\mathrm{cal}^{1/2}\mathrm{cm}^{-3/2}$ for methylene chloride and acetone with much higher swelling of methylene chloride compared with acetone that is related to the polarity of the solvents. The solubility of solvents in PDMS is also determined with interaction radius (R_i) (Eq. 3-3) and has the same unit as solubility parameter [36]. The smaller the R_i, the higher the solubility of the solvent into PDMS [37]. Solubility parameter of studied pure liquids in this work and R_i are represented in table 3.1

$$R_i^2 = 4\left(\delta_{solute,d} - \delta_{solvent,d}\right)^2 + \left(\delta_{solute,p} - \delta_{solvent,p}\right)^2 + \left(\delta_{solute,h} - \delta_{solvent,h}\right)^2 \qquad (3-3)$$

Table 3.1. Solubility parameters and interaction radius of pure liquids and PDMS

	δ_d ($\mathrm{MPa}^{0.5}$)	δ_p ($\mathrm{MPa}^{0.5}$)	δ_h ($\mathrm{MPa}^{0.5}$)	δ ($\mathrm{MPa}^{0.5}$)	R_i ($\mathrm{MPa}^{0.5}$)
Hexane [38]	14.9	0.01	0.0	14.9	9.45
Toluene [38]	18.04	1.39	2.0	18.2	7.11
Acetone [38]	15.5	10.4	7	19.93	11.63
Methanol [38]	15.1	12.3	22.3	29.61	18.66
Isopropanol [38]	15.8	6.1	16.4	23.57	12.05
Benzene [38]	18.4	0.0	2.0	18.5	7.28
PDMS [39]	16.86	0.12	8.6	18.92	---

It is noteworthy to mention that experimental swelling ratio of PDMS at room temperature (i.e. 22 °C) was measured using the following equation where w is the mass of swollen network and W_0 is the mass of dry extracted PDMS slab.

$$Swell\ ratio = \frac{w - w_0}{w_0} \qquad (3-4)$$

3.3. Experimental Section

3.3.1. Materials

Hexane (lab grade), acetone (lab grade), methanol (analytical grade), toluene (HPLC grade), and isopropanol (lab grade) were supplied from Sigma-Aldrich Co., USA. PDMS (Sylgard 184 Silicone Elastomer Kit) purchased from Dow Corning Co., USA. PFOCTS was supplied from Sigma-Aldrich Co., USA. McKay River bitumen was provided by InnoTech Alberta. The solid and water content of the bitumen sample was less than 0.5%

3.3.2. PDMS Fabrication and Bitumen Sample Preparation

According to the manufacturer (Dow Corning, Midland, MI), the recommended ratio for curing agent to base is 1:10. Here we have tried two other ratios with higher curing agent (1:2) and less (1:20) to evaluate the optimum ratio for PDMS fabrication. Therefore, PDMS samples were prepared by mixing a 1:2, 1:10, and 1:20 curing agent to base (Sylgard 184) ratios. Higher curing agent:base ratio means higher cross linking and rigid PDMS structure that breaks easily under shear strain. Mixture was degassed in a vacuum chamber for 60 minutes to remove the air

trapped during the mixing. Then mixture was poured into a brass mold with two cylindrical reservoirs and a 20 mm × 1 mm × 100 μm (length × width × depth) rectangular channel connecting the reservoirs. After 24 hours curing at 80ºC to add Si-H to C=C bonds. PDMS was extracted and individual chips was washed and glass substrate (24 × 50 microscope coverslips from Fisher Scientific) was bonded to the PDMS forming an enclosed space. In addition to microchannel, PDMS samples were cut into small square pieces (2.5 cm × 2.5 cm) to submerge in different liquids. These pieces were washed with acetone and then DI water to remove the possible contaminants. Stock bitumen was used to prepare 10% to 50% bitumen dilutions in hexane. All the samples were aged for 24 hours to settle down the large aggregates and precipitates.

3.3.3. Silanization

Effect of silanization on swelling ratio of PDMS slabs in solvents were evaluated by coating the PDMS surface with PFOCTS. In fact, this coating is a fast and cheap process for surface modification that can improve the possibility of using PDMS microchannel in solvent-based heavy oil extraction studies. For silanization, a small amount of PFOCTS was placed in a vacuum chamber for four hours at room temperature (i.e. 22 °C). Evaporated silane molecules reacted with the surface to form siloxane bonds at the interface. Irreversible bonding forms a monolayer of silane that was confirmed by water contact angle measurement that increased from ~ 95 degree (untreated PDMS) to ~ 115 degree (silanized PDMS) as shown in figure 3.1. Noteworthy to mention that plasma treatment was conducted on PDMS slabs to activate the surface before silanization process [28].

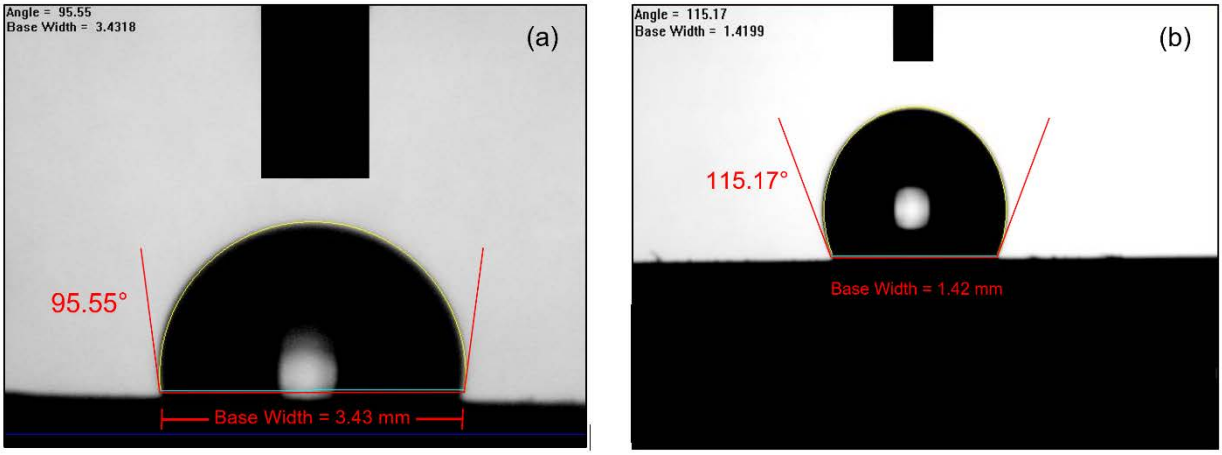

Figure 3.1. Water contact angle on (a) pure PDMS and (b) PFOCTS treated PDMS slab

3.3.4. UV-VIS Spectrophotometer

The transparency of the PDMS swollen at different bitumen samples was measured using ultraviolet-visible (UV-VIS) spectrophotometer (Cary 50 UV-Vis, Varian Inc., USA) at a wavelength of 400 nm and room temperature (22 °C). For this purpose, transparency of 2.5 cm × 1 cm × 0.3 cm (length × width × thickness) PDMS slabs was measured as a function of time. Absorbance (A) was calculated and related to the transmittance (T) based on the Eq. (3-2).

$$A = \log_{10}\left(\frac{100}{T(\%)}\right) = 2 - \log(T\%) \qquad (3-5)$$

3.3.5. TIRF Microscopy

In this work, TIRF microscopy was applied on the surface of PDMS to image adsorbed bitumen due to its fluorescence nature [40]. This method excites fluorescence at solid surface without any other fluorescence background from deeper areas [30]. Therefore, fluorescence

nature of the bitumen enables us to capture bitumen absorption on the surface of the sample. As mentioned earlier, TIRF microscopy eliminates background noises. In fact, PDMS has small pores on the surface and TIRF microscope illustrates bitumen distribution on specific spatial location. Based on previous study in our group [30], a 488-nm laser source and 500-550 nm (green) emission filter were selected for the microscopy.

3.4. Results and Discussion

3.4.1. Pure Solvents Swelling

The first part was related to the effects of PDMS preparation method on solubility in different solvents. Therefore, weight of swollen networks at different reagent to base ratios (1:10, 1:2, 1:20) were recorded. All sides of PDMS slabs should be covered with solvent for a uniform absorption of the solvent. Swelling ratio of the PDMS in solvent should be measured until equilibrium condition. This condition was considered at the time that there is no more change in the mass of swollen network. Based upon this, a procedure was developed whereby small (5cm x 5cm) squares of PDMS were immersed in solvent in airtight bottles. Due to the volatile nature of the solvents when exposed to air at room temperature (22 °C), the evaporation of the solvent could affect the measurements. This was resolved by measuring the weight of samples while it was submersed in the solvent plate. Weight of samples was measured in different time intervals until a constant weight was observed.

Swelling ratio of PDMS samples (1:2, 1:10, and 1:20 ratios) in different solvents are depicted in figure 3.2. Slabs were submerged into solvent and weight of samples was measured. Each

experiment was performed three times to evaluate the reliability of the results and error bars were calculated based on repeatability of the experiments with a 95% confidence interval of the mean. According to the error bars, the highest standard deviation of mean was related to PDMS slab submerged in toluene (1.286 ± 0.0317) that was small enough (< 5%) to confirm the repeatability and reliability of the experiments.

According to calculation, 1:20 PDMS slab had highest swelling ratio where submerged slabs in toluene and hexane with 128% and 105% increase in weight had the largest ratios. It means low cross linked elastomer (1:20 curing agent:base PDMS) swells more than other ratios where solvent molecules detach non-crosslinked oligomers from PDMS. Toluene and hexane swelled over 85% after 80 minutes while other solvents had less than 20% of swelling. In fact, PDMS with low polarity [41] contribution had higher swelling ratio in liquids with lower polarity index (i.e. toluene and hexane), while PDMS is more compatible with polar liquids (i.e. methanol, acetone, isopropanol). Solvents with high solubility in PDMS are not compatible with PDMS microfluidic platforms even for fast experiments. As it is shown, higher rate of swelling was related to the first 60 minutes and was decreased until equilibrium condition was achieved. Swelling was stopped after 350 minutes for 1:20 PDMS in toluene and 250 minutes for 1:20 ratio PDMS in hexane. The comparison between the 1:10 and 1:2 PDMS slabs revealed that a sample with higher reagent to base ratio (1:2) with a rigid, fragile structure had the higher swelling ratio. Curing agent to base ratio affected the number of cross-links in cured PDMS and higher swelling ratio of PDMS in solvent [16]. It seems the 1:10 cross-linker to base reagent ratio was the preferential ratio for minimizing organic solvent absorption. Neither increasing nor decreasing the amount of cross-linker had any beneficial effects for solvent compatibility. This confirms previous studies that showed minimum swelling ratio for 1:10 PDMS sample [42].

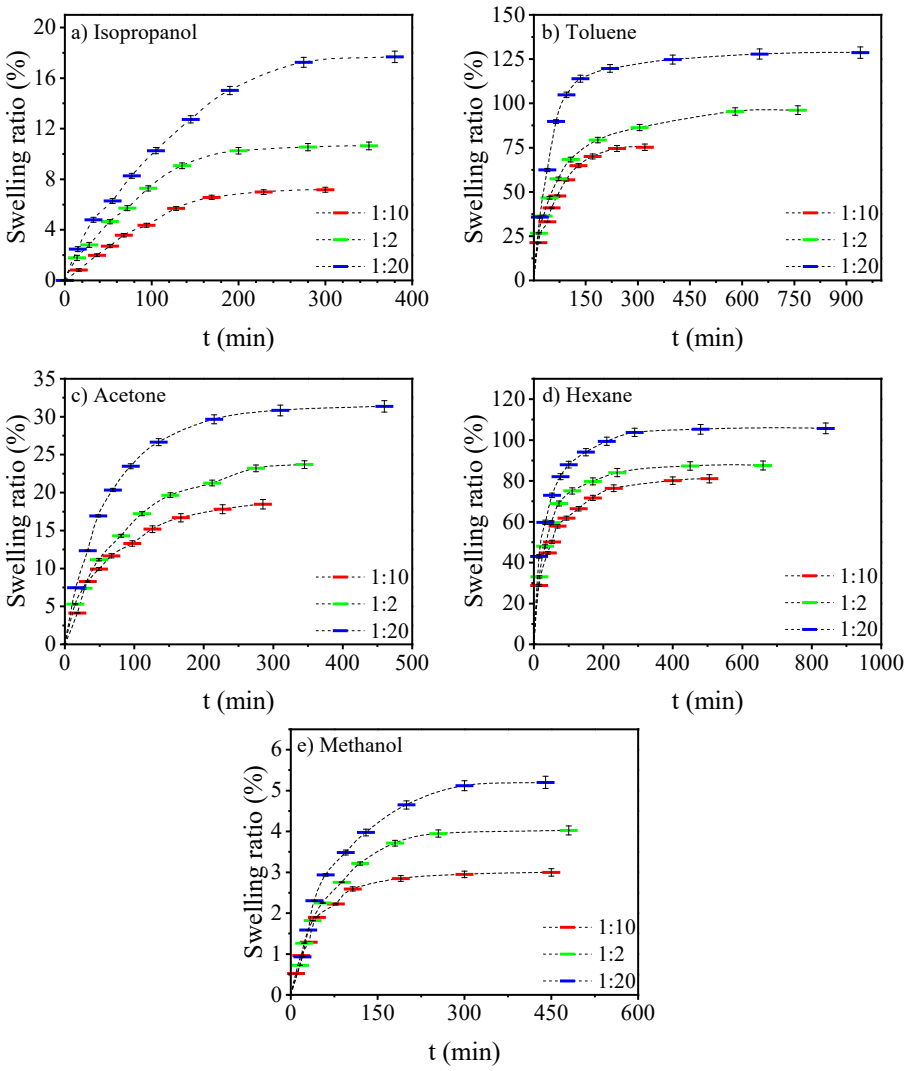

Figure 3.2. Swelling ratio of PDMS chips in a) Isopropanol, b) Toluene, c) Acetone, d) Hexane, e) Methanol. Error bars were calculated with repeatability of the experiment.

The final swelling ratio as a function of solubility parameter is shown in figure 3.3. According to figure 3.2, the highest swelling ratios were related to the 1:20 PDMS slab in toluene and hexane. These two solvents had smaller interaction radius (table 3.1) compared with the other liquids. Moreover, effective factors on the solubility parameter can affect the swelling ratio drastically. For instance, as represented in table. 3.1 [38], the polar section of the acetone (10.4 $MPa^{0.5}$) is different compared to hexane (i.e. 0.01 $MPa^{0.5}$) and caused different PDMS

swellings of 105% and 31% respectively. In fact, low soluble liquids had a high polar force section (δ_p > 10 MPa0.5), while highly soluble solvents had a small polar force (<1.5 $MPa^{0.5}$) that is closer to the PDMS polar force. Figure 3.3 showed that different reagent to base PDMS samples for low soluble liquids, such as methanol did not affect the swelling ratio.

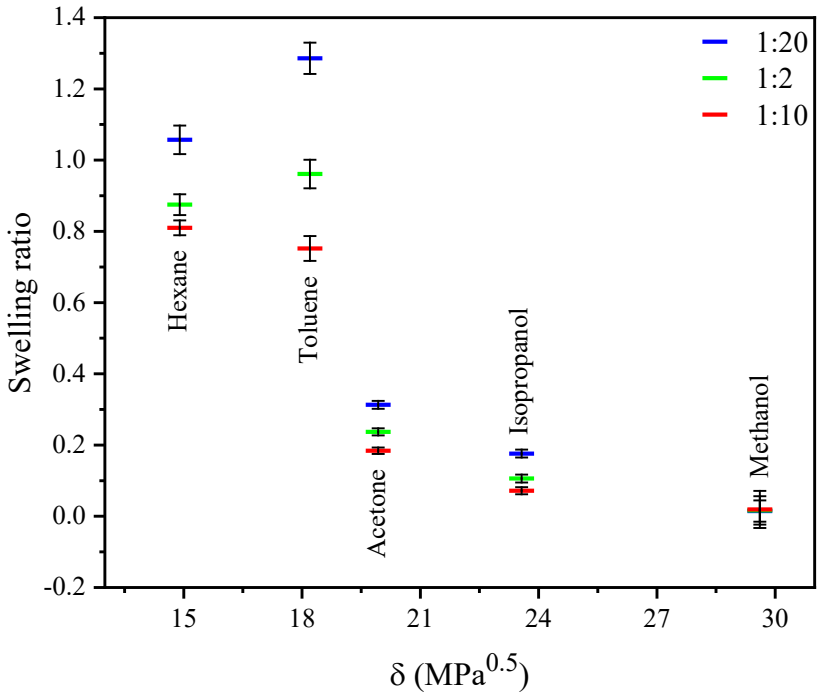

Figure 3.3. Equilibrium swelling ratio of PDMS at different solvents (hallow shape: 1:2, filled shape: 1:10, and blank shape: 1:20 reagent to base ratio PDMS)

Figure 3.4 depicts the swelling ratio of PFOCTS coated PDMS slabs at different curing agent:base ratios submerged in toluene. PDMS coating followed the same steps for all the samples and each experiment was repeated three times to compare the mean and standard deviation values. Swelling ratios and standard error of means are in the same order of uncoated PDMS samples therefore, silane coating did not improve the solvent compatibility of the PDMS. It shows that coating with short-chain silane would not affect the swelling. In other words, the low wetting did not prevent the diffusion of small solvent molecules into PDMS when immersed

in the solvent. Kushmeric et al. [43] showed aggregates of deposited perfluorocyltrichlorosilane on the surface of PDMS led to the degradation of expected hydrophobic surface property of treated PDMS.

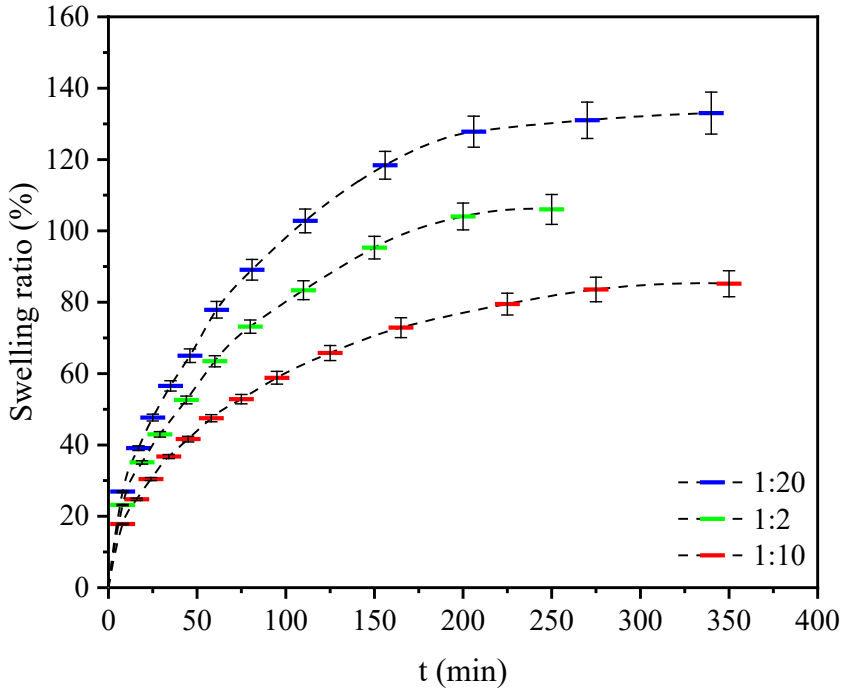

Figure 3.4. Swelling ratio of PFOCTS coated PDMS slabs in toluene

3.4.2. Diluted Bitumen

3.4.2.1. Swelling Ratio

The main part of this study is to determine compatibility of PDMS chip in heavy oil and bitumen extraction studies. Transparent nature of PDMS along with its flexibility makes it a suitable option for micro structure fabrication. However, the nature of bitumen as a complex fluid as well as organic solvents such as hexane in extraction methods like VAPEX can affect the microchannel structure, size and even transparency. Therefore, swelling ratio of 1:2 and 1:10

curing agent to base PDMS samples were evaluated in diluted bitumen samples in hexane (10 wt% to 50 wt%). As shown in figure 3.5, higher swelling ratio for the 1:2 PDMS slabs was notified compared with 1:10 samples that means the later one is the optimum ratio. However, swelling ratio for both PDMS samples was too high and not acceptable for heavy oil and bitumen related experiments. The higher swelling ratio was related to 10 wt% bitumen samples which means solvent had more effect on swelling compared with bitumen. However, higher equilibrium swelling ratio of 10 wt% bitumen sample compared with pure hexane swelling ratio revealed the effect of bitumen molecules sticking on the surface of PDMS slab. In fact, large bitumen molecules along with solvent, increased the swelling ratio but with increasing the concentration of bitumen, effect of solvent molecules, as the dominant molecule, was reduced compared to pure solvent.

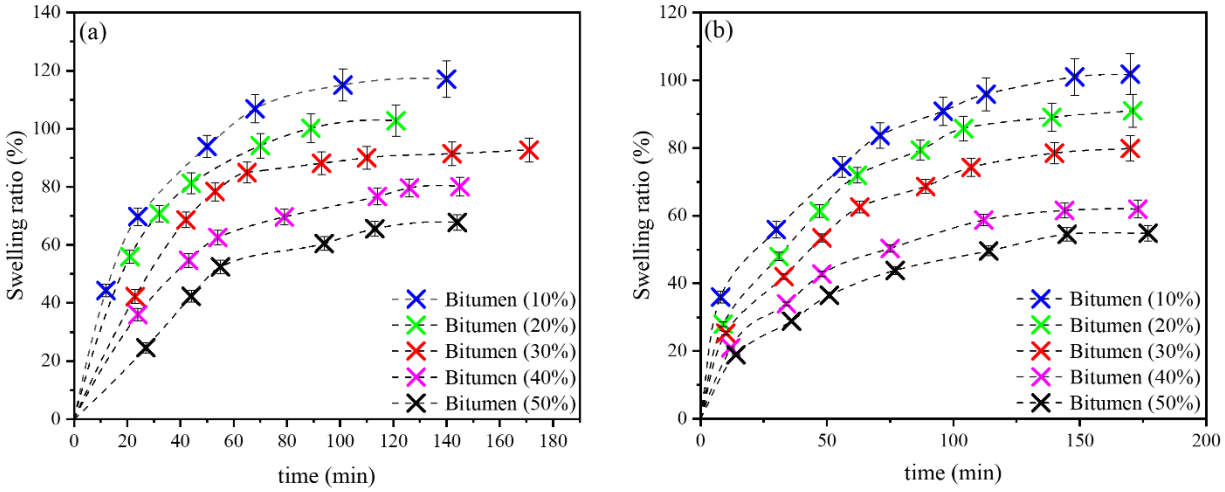

Figure 3.5. Swelling ratio of diluted bitumen in PDMS, a) 1:2, b) 1:10

In order to have a better understanding about the deformation of the samples, PDMS microchannel was fabricated and diluted bitumen was injected into the microchannel. Prior to diluted bitumen injection, PDMS microchannel was examined with water with no destructive

effect on PDMS using white light microscope coupled with high-speed CCD camera. According to time-lapsed images of water capillary flow in PDMS microchannel (figure 3.6), deformation of channel and leakage was not monitored and water flowed through the microchannel. In fact, it confirmed PDMS microchannel is applicable in capillary-driven flow study of specific liquids. Moreover, capillary flow of diluted bitumen (10 wt% to 60 wt%) in glass etched microchannels was studied in our previous work and proved the application of glass microchannel for any kind of liquid due to glass stability and resistivity [4].

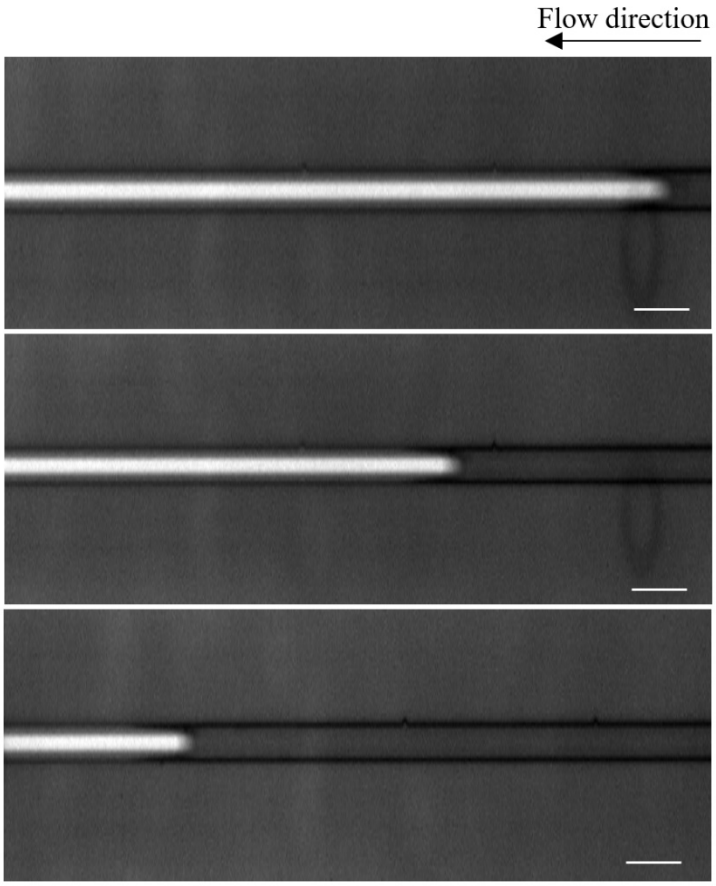

Figure 3.6. Time-lapsed images of water flow in PDMS microchannel. Scale bar is 1mm.

An extremely fast lateral diffusion of 30% diluted bitumen out of the microchannel, into the glass PDMS temporary bonding, was noticed in 20 seconds after injection. The edge of

microchannel (red solid line) and direction of bitumen diffusion (vertical arrow) are represented in figure 3.7a. In fact, the first black line from the bottom is related to microchannel, the grey region is diffused bitumen and the upper region is PDMS and glass bonded area. Diluted bitumen changed both the size and structure of microchannel very fast that showed PDMS microchannel are not applicable in bitumen visualization. A top and side view of the microchannel with diffusion of bitumen into the bonded layer after five minutes is shown in figure 3.7b and 3.7c. Diffusion of bitumen out of the injection reservoir and microchannel is represented in figure 3.7b. Figure 3.7c depicts side view of the microchannel deformation and detachment of PDMS glass bonding.

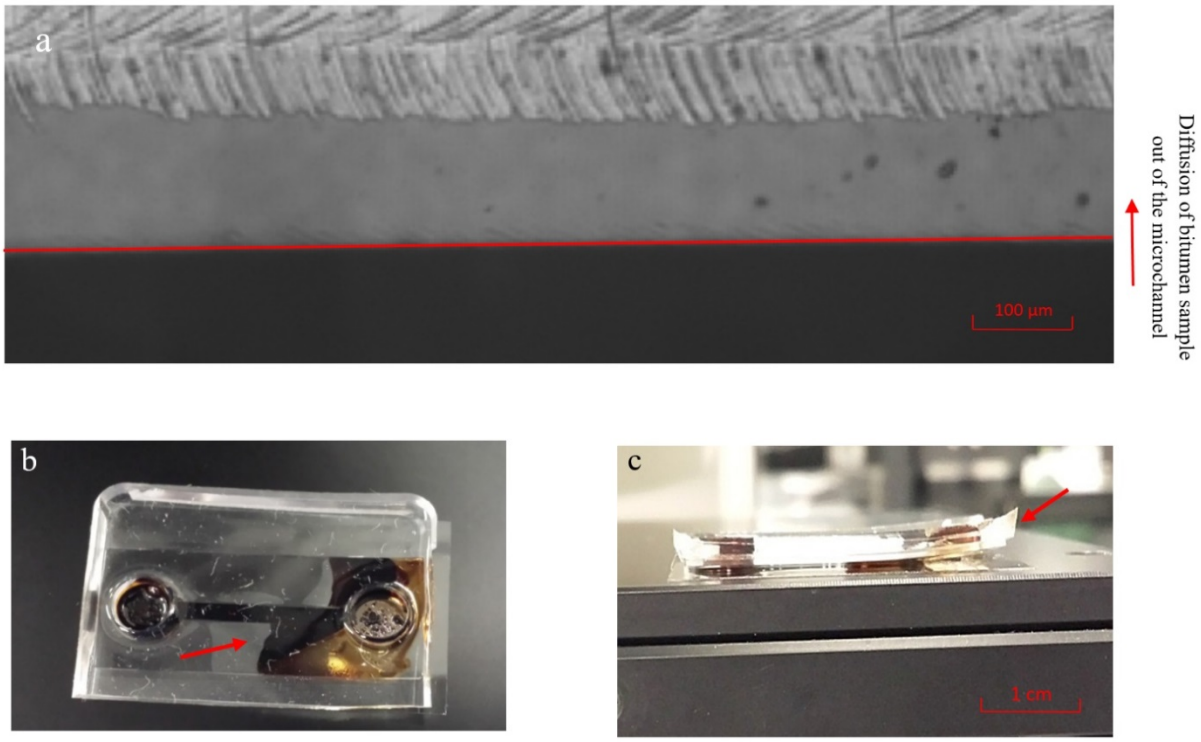

Figure 3.7. Diffusion of 50% bitumen into PDMS microchannel a: microscopic view after 30 seconds, b: top view and c: side view after 5 minutes

3.4.2.2. Transparency and Fluorescence Intensity

The UV-VIS transmittance spectra of 1:10 curing agent to base ratio PDMS is shown in figure 3.8 as a function of time at 400 nm wavelength based on three measurements at different positions of the sample. A higher transmittance reduction of PDMS was reported with increasing the concentration of bitumen. Transparency of 50% bitumen after 180 minutes was as low as 15% which is not enough for using PDMS microchannel in heavy oil and bitumen flow study.

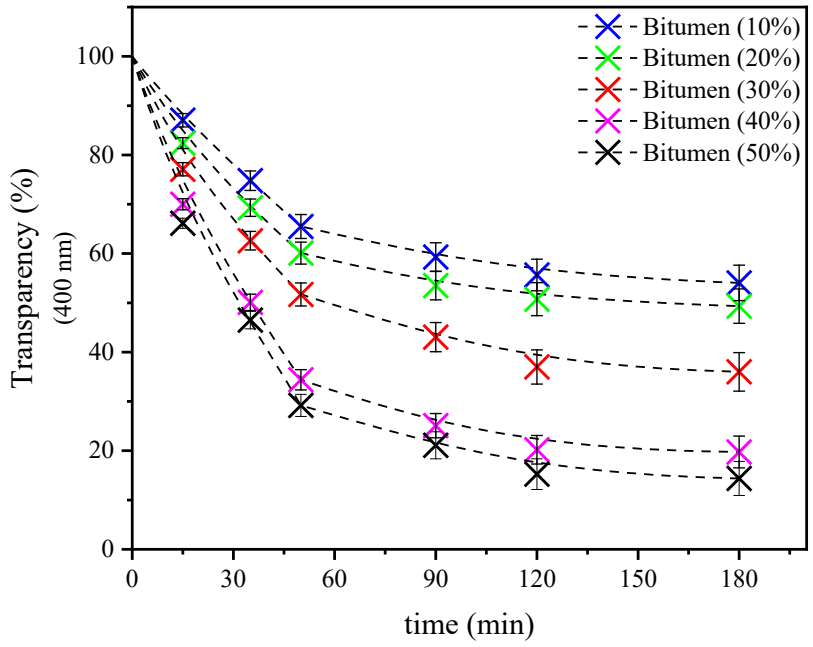

Figure 3.8. UV-VIS spectrum of a 4mm thick 1:10 PDMS slab at different bitumen concentration

Fluorescence microscopy is an efficient way to detect bitumen because of its natural fluorescence. Therefore, TIRF microscopy was applied to detect bitumen on the surface layer of 1:10 PDMS in different bitumen samples (10 wt% to 50 wt%). PDMS slab was submerged into bitumen sample and bitumen content was evaluated at different times. Based on previous studies, it was understood that fluorescence from the hexane does not interfere with fluorescence from

bitumen in our desired excitation and emission wavelength so all the fluorescence is emitted by bitumen. Fluorescence intensity of 1:10 PDMS in diluted bitumen (50 wt%) with a 488 nm laser source and 500-550 nm emission filter (green) after 1, 2 and 3 minutes is shown in figure 3.9.

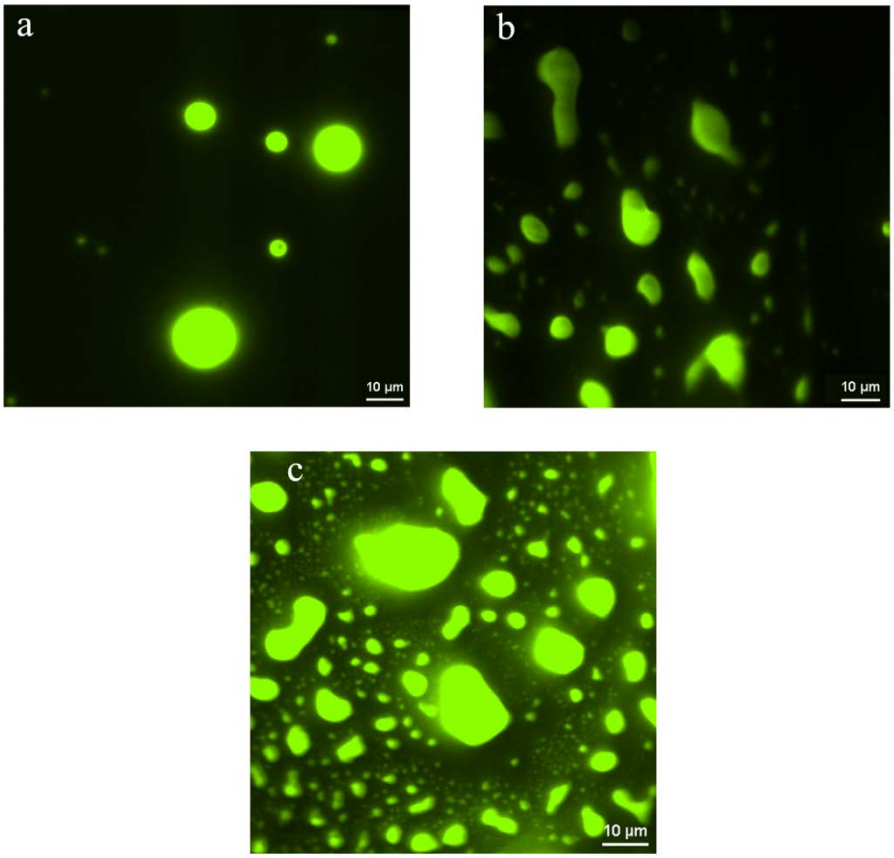

Figure 3.9. TIRF images of PDMS swollen at 50% bitumen solution a) t=1 min, b) t= 2 min, c) t=3 min

Fluorescent images showed that bitumen content of the PDMS surface is increasing fast that makes PDMS inappropriate for micro-scale monitoring of heavy oil and bitumen. Moreover, bitumen size increased on the surface that could be related to bridging and aggregation of asphaltene and other components of the bitumen on the PDMS surface. However, larger size of bitumen molecules compared with pure solvents did not reduce the swelling rate of bitumen in

PDMS slab and PDMS microchannel. All in all, it seems dynamic of the swelling is fast and it is not possible to use PDMS either for pure solvent or high viscosity fluids such as bitumen and heavy oil.

3.5. Conclusion

Application of PDMS microchannel can improve our understanding of fluid flow in small scales such as porous media. The solubility parameter is effective in swelling correlation and solvent compatibility of PDMS. It has been reported that PDMS will highly swells in contact with pure solvents that makes it inappropriate for solvent related studies. This is related to polar factor of solubility parameter where similar polar factors between solvent and PDMS lead to high swelling as in case of toluene and hexane. It was found that swelling of immersed PDMS into toluene and hexane was very fast with deformation of the PDMS slab (i.e. curved edges). However, degree of swelling in other solvents was relatively low. In addition, effect of solvent swelling on different PDMS (curing agent to base ratio) was measured to find the best ratio for PDMS fabrication and results indicated that the 1:10 PDMS had the minimum swelling. The improvement of solvent compatibility of PDMS with silanization was evaluated using PFOCTS as a fast and low-price method of surface modification. However, high level of swelling ratios was reported for coated PDMS slabs. This means surface treatment with short-chain silane did not improve the resistivity toward swelling and is not a suitable approach for solvent compatibility enhancement.

Moreover, compatibility of PDMS with bitumen as a highly viscos and large molecule fluid was evaluated to investigate the application of PDMS in heavy oil and bitumen flow study. In

other words, when dynamic of swelling is not very fast, PDMS microchannel is still applicable for investigation of fluid flow. Diluted bitumen (10 wt% to 50 wt%) was injected in PDMS fabricated microchannel and the shape of microchannel was disturbed after and glass PDMS bonding was broken. Deformation of microchannel along with fast dynamic of swelling confirmed PDMS is not suitable for evaluation of flow and rheology of heavy oil and bitumen. Furthermore, transparency of 1:2 and 1:10 PDMS slabs were measured and showed higher concentration of bitumen led to lower transparency and poor bitumen flow visualization consequently. TIRF microscopy was the last step for evaluation of bitumen swelling dynamic. It clearly showed a fast bitumen concentration increasing on the PDMS surface. High level of swelling, low transparency and high concentration of bitumen on the surface are solid reasons to believe that PDMS microchannel is limited to certain solvents and is not a potential replacement for glass microchannel in heavy oil study.

References

[1] C. Hu, J. E. Morris and R. L. Hartman, "Microfluidic investigation of the deposition of asphaltenes in porous media," Lab on a Chip, vol. 14, no. 12, pp. 2014-2022, 2014.

[2] S. Molla and F. Mostowfi, "Microfluidic PVT–Saturation Pressure and Phase-Volume Measurement of Black Oils," SPE Reservoir Evaluation & Engineering, vol. 20, no. 1, pp. 233-239, 2017.

[3] R. Fisher, M. K. Shah, D. Eskin, K. Schmidt, A. Singh, S. Molla and F. Mostowfi, "Equilibrium gas–oil ratio measurements using a microfluidic technique," Lab on a Chip, vol. 13, pp. 2623-2633, 2013.

[4] K. Keshmiri, S. Mozaffari, P. Tchoukov, H. Huang and N. Nazemifard, "Using Microfluidic Device to Study Rheological Properties of Heavy Oil," in American Institude of Chemical Engineering (AIChE), San Francico, CA, USA, 2016.

[5] K. Xu, T. Liang , P. Zhu, P. Qi, J. Lu, C. Huh and M. Balhoff, "A 2.5-D glass micromodel for investigation of multi-phase flow in porous media," Lab on a Chip, vol. 17, pp. 640-646, 2017.

[6] J. P. Esquivel, F. J. Del Campo, J. L. Gómez de la Fuente, S. Rojas and N. Sabaté, "Microfluidic fuel cells on paper: meeting the power needs of next generation lateral flow devices," Energy and Environmental Scienece, vol. 7, pp. 1744-1749, 2014.

[7] G. Pasirayi, V. Auger, S. Scott, P. Rahman, M. Islam, L. O'Hare and Z. Ali, "Microfluidic Bioreactors for Cell Culturing: A Review," Micro and Nanosystems, vol. 3, pp. 137-160, 2011.

[8] L. Va, "Microfluidics: an enabling screening technology for enhanced oil recovery (EOR)," Lab on a Chip, vol. 16, no. 10, pp. 1777-1796, 2016.

[9] P. Lele, A. H. Syed, J. Riordon, N. Mosavat, A. Guerrero, H. Fadaei and D. Sinton, "Deformation of microdroplets in crude oil for rapid screening of enhanced oil recovery additives," Journal of Petroleum Science and Engineering, Vols. In Press, Accepted Manuscript, 2018.

[10] H. Lee, S. G. Leeb and P. S. Doyle, "Photopatterned oil-reservoir micromodels with tailored wetting properties," Lab Chip, vol. 15, p. 3047, 2015.

[11] D. Reyes, D. Iossifidis, P. A. Auroux and A. Manz, "Micro total analysis systems. 1. Introduction, theory, and technology," Anal Chem, vol. 74, no. 12, pp. 2623-36, 2002.

[12] E. Carrilho, S. M. Lunte and W. K. T. Coltro, "Comparison of the analytical performance of electrophoresis microchannels fabricated in PDMS, glass, and polyester-toner," Electrophoresis, vol. 29, no. 24, p. 4928–4937, 2008.

[13] M. Hashimoto, R. Langer and D. S. Kohane, "Benchtop fabrication of microfluidic systems based on curable polymers with improved solvent compatibility," Lab Chip, vol. 13, pp. 252-259, 2013.

[14] E. Leclerc, Y. Sakai and T. Fujii, "Microfluidic PDMS (Polydimethylsiloxane) Bioreactor forLarge-Scale Culture of Hepatocytes," Biotechnology Progress, vol. 20, pp. 750-755, 2004.

[15] M. Yao and J. Fang, "Hydrophilic PEO-PDMS for microfluidic applications," Journal of Micromechanics and Microengineering, vol. 22, no. 2, p. 025012, 2012.

[16] J. Ng Lee, C. Park and G. M. Whitesides, "Solvent Compatibility of Poly(dimethylsiloxane)-Based Microfluidic Devices," Analytical Chemistry, vol. 75 (23), p. 6544–655, 2003.

[17] J. Ng, I. Gitlin, A. Stroock and G. Whitesides, "Components for integrated poly(dimethylsiloxane) microfluidic systems," Electrophoresis, vol. 23(20), pp. 3461-73, 2002.

[18] I. D. Johnston, D. K. McCluskey, C. K. L. Tan and M. C. Tracey, "Mechanical characterization of bulk Sylgard 184 for microfluidics and microengineering," Journal of Micromechanics and Microengineering, vol. 24, p. 35017, 2014.

[19] C. Xiang, N. Yang, R. Zhang, J. Guo and H. Huang, "An Ultraviolet-Visible (UV) Photometry System Based on the PDMS-based Microfluidic Chip," in 13th Global Congress on Manufacturing and Management (GCMM 2016), 2017.

[20] K. Khanafer, A. Duprey, M. Schlicht and R. Berguer, "Effects of strain rate, mixing ratio, and stress–strain definition on the mechanical behavior of thepolydimethylsiloxane (PDMS) material as related to its biological applications," Biomed. Microdevices, vol. 11, no. 2, pp. 503-508, 2009.

[21] Z. Wang, "Polydimethylsiloxane mechanical properties measured by macro-scopic compression and nanoindentation techniques," Ph.D. thesis, University of South Florida, 2011.

[22] R. Seghir and S. Arscott, "Extended PDMS stiffness range for flexible systems," Sensors and Actuators, vol. 230, no. A, pp. 33-39, 2015.

[23] F. Saryazdi, H. Motahhari, F. F. Schoeggl, S. D. Taylor and H. W. Yarranton, "Density of Hydrocarbon Mixtures and Bitumen Diluted with Solvents and Dissolved Gases," Energy and Fuels, vol. 27, no. 7, pp. 3666-3678, 2013.

[24] A. R. Abate, D. Lee, T. Do, C. Holtzea and D. A. Weitz, "Glass coating for PDMS microfluidic channels by sol–gel methods," Lab Chip, vol. 8, pp. 516-518, 2008.

[25] S. H. Cho, J. Godin and Y. Lo, "Optofluidic Waveguides in Teflon AF-Coated PDMS Microfluidic Channels," IEEE Photonics Technol Lett, vol. 21, no. 15, p. 1057–1059, 2009.

[26] G. A. Diaz-Quijada and D. D. M. Wayner, "A Simple Approach to Micropatterning and Surface Modification of Poly(dimethylsiloxane)," Langmuir, vol. 20, pp. 9607-11, 2004.

[27] M. Khorasani and H. Mirzadeh, "Laser surface modification of silicone rubber to reduce platelet adhesion in vitro," J Biomater Sci Polym Ed, vol. 15, no. 1, pp. 59-72, 2004.

[28] Z. Pan, H. Shahsavan, W. Zhang, F. K. Yang and B. Zhao, "Superhydro-oleophobic bio-inspired polydimethylsiloxane micropillared surface via FDTS coating/blending approaches," Applied Surface Science, vol. 324, pp. 612-620, 2015.

[29] R. M. Diebold and D. R. Clarke, "Smooth, Aggregate-Free Self-Assembled Monolayer Deposition of Silane Coupling Agents on Silicon Dioxide," Langmuir, vol. 28, no. 44, pp. 15513-15520, 2012.

[30] S. S. Shende, S. Pendharker, Z. Jacob and N. Nazemifard, "Total Internal Reflection Fluorescence Microscopy To Investigate the Distribution of Residual Bitumen in Oil Sands Tailings," Energy Fuels, vol. 30, no. 7, p. 5537–5546, 2016.

[31] Y. Du, Y. Xue and H. L. Frisch, Physical Properties of Polymers Handbook, Woodbury, NY: AIP Press, 1996.

[32] T. Ougizawa and T. Inoue, Miscibility and interfacial behavior in polymer-polymer mixtures, in polymer blends and alloys, NY, chapter 3: Marcel Dekker, Inc, 1999.

[33] C. V. Rumens, M. A. Ziai, K. E. Belsey, J. C. Batchelor and S. J. Holder, "Swelling of PDMS networks in solvent vapours; applications for passive RFID wireless sensors," J. Mater. Chem. C, pp. 10091-10098, 2015.

[34] C. M. Hansen, "50 Years with solubility parameters—past and future," Progress in Organic Coatings, vol. 51, pp. 77-84, 2004.

[35] X. Su, B. Shi and L. Wang, "Investigation on Three-Dimensional Solubility Parameters for Explanation and Prediction of Swelling Degree of Polydimethylsiloxane Pervaporation Membranes," Journal of Macromolecular Science, vol. 54, p. 1248–1258, 2015.

[36] C. M. Hansen, Hansen Solubility Parameters: A User's Handbook, Boca Raton: CRC Press, 2007.

[37] Y. Kusano, S. Teodoru and C. M. Hansen, "The physical and chemical properties of plasma treated ultra-high-molecular-weight polyethylene fibers," Surface and Coatings Technology, vol. 205, p. 2793–2798, 2011.

[38] J. Bruke, Solubility parameters: theory and application, Harvard, 1984.

[39] H. Soltane, D. Roizard and E. Favre, "Effect of pressure on the swelling and fluxes of dense PDMS membranes in nanofiltration: an experimental study," J. Membr. Sci., vol. 435, p. 110–119, 2013.

[40] F. Handle, J. Füssl, S. Neudl, D. Grossegger, L. Eberhardsteiner, B. Hofko, M. Hospodka, R. Blab and H. Grothe, "The bitumen microstructure: a fluorescent approach," Materials and Structures, vol. 49, no. 1-2, pp. 167-180, 2016.

[41] N. A. Diachun, A. H. Marcus and M. D. Fayer, "Dynamics in Polydimethylsiloxane: The Effect of Solute Polarity," Journal of American Chemical Society, vol. 116, pp. 1027-1032, 1994.

[42] D. J. Campbell and S. B. Rupe, "Solvent Swelling and Optical Rotation Demonstrated on the Overhead Projector," Journal of Chemical Education, vol. 77, no. 7, 2000.

[43] J. G. Kushmeric, M. G. Hankins, M. de Boer, P. J. Clews and R. Carpick, "The influence of coating structure on micromachine stiction," Tribology Letters, vol. 10, no. 1-2, pp. 103-108, 2001.

Chapter 4: Measurement of Solvent Diffusion in Bitumen

As discussed in chapter 3, PDMS micromodel was not applicable in pore-scale study of heavy oil and bitumen. Therefore, glass was selected as the best potential material for micromodel fabrication during the work.

4.1. Introduction

World energy demand along with limited conventional oil resources, are bringing more attempts to find potential resources and transform them into commercial field. Discoveries lead to find unconventional resources like bitumen and heavy oils with different properties compared with light oils [1]. The main difference is their high viscosity that challenges production and transportation [2]. There are different heavy oils and bitumen recovery methods including miscible displacement, chemical flooding and thermal recoveries. Application of horizontal well drilling with these methods or combination of them improves in-situ recovery. There is an extremely high viscosity of the reservoir oil (exceeds 1 million cP [3]) that causes to wide application of thermal methods to take advantages of temperature dependency of heavy oil viscosity.

SAGD is the most well-known thermal technique. However, high energy consumption and CO_2 emission are the main disadvantages of this method [4]. Butler [5] suggested a new recovery method analogue of SAGD based on solvent injection and dilution instead of heating for viscosity reduction. Dilution of the bitumen in solvent based methods causes deasphaltene and in-situ upgrading, consequently. This process has two horizontal well pairs with the injection

A version of this chapter is Accepted to publish at Fuel journal.

well where solvent dissolves into the bitumen and mobilized diluted bitumen drain down into production well [6, 7]. As a result, active diffusion mechanism in heavy oils can be Fickian diffusion in which molecules pass each other freely or Single File diffusion. These heavy oil resources are made up of a fluid phase and a nanodispersed asphaltene rich phase where molecules cannot bypass each other [8, 9]. Mass transfer plays a critical role in such process designs where molecular diffusion is the dominant mechanism in solvent based method [10]. Diffusion coefficient determine dissolution rate of the solvent into heavy oil. Therefore, it is necessary to have a reliable understanding of that for reliable solvent based method design and simulation prediction.

However, measurement of mass transfer coefficient is always challenging due to difficulties in concentration measurement [11]. There are different methods for measuring diffusion of gas or liquid into the liquid such as pressure decay method [12], concentration profile measurement [13], Hele-Shaw cell [14] for gas-liquid and Nuclear Magnetic Resonance (NMR) [15], laser refraction [16], X-ray for liquid-liquid binary system [17]. Tharanivasan et al. [18] applied pressure-decay method to measure molecular diffusivities of carbon dioxide, methane, and propane in heavy oil. Pressure in the solvent phase inside a high-pressure diffusion cell were measured and compared with numerically calculated pressures. Oballa and Butler [19] measured concentration dependent mutual diffusion coefficient of toluene-Cold Lake bitumen in a glass diffusion cell using laser transmission imaging method. Salama and Kantzas applied X-ray computer assisted tomography to study mass transfer of solvents in heavy oil and calculation of diffusion coefficient using Boltzmann-Matano approach. In all of the publications diffusion is assumed to be Fickian. Only recently Alizadehgiashi and Shaw [20] and Pourmohammadbagher [21] showed that Single File diffusion or sorption by nanodispersed domains in heavy oils

(asphaltenes) can play a role in diffusion in addition to Fickian behavior. They observed that in diffusion of light hydrocarbons in heavy oils, at high mass fractions of heavy oil, Single File diffusion is present and as mass fraction of solvent increases, diffusion mechanism shifts towards Fickian diffusion. In addition, they observed that n-alkanes are a better choice for solvents because it precipitates asphaltenes and results in faster diffusion. However, possible effects of accumulation of precipatetes in micro/nano channeled reservoir rocks are poorly understood.

Micromodels are two-dimensional network models that simulate natural process. This elegant approach proved useful in various fields of energy and fuel [22]. They are compatible with many visualization techniques and can provide a unique opportunity to evaluate a process in real time at the same length scale of pore-level. They give insight to the pore-scale interplay of various aspects of transport phenomena. In recent years micromodels, have proven to be an easy, fast and economical tool for conducting small-scale experiments that provide the opportunity to discover yet unrecognized processes and enhance the understanding of existing theories and assumptions.

Fluid behavior in conventional pore-scale methods is not able to monitor properly due to the opaque nature of the rock matrix and information of initial and final stages are the only available data. Some methods such as X-ray computed chromatography (X-ray CT) have developed but there is temporal and spatial resolution. In fact, fluid flow visualization is accompanied by poor resolution in small scale (10^{-3}m). Microfluidics offers direct optical visualization to observe transport mechanisms and bulk transport properties along with pore-level observation with the aid of microscope [23]. In our previous work, flow of diluted bitumen in treated and untreated microchannels were evaluated and compared with Washburn model [24]. Application of microchannel enabled us to monitor the bitumen flow and compare the effect of surface

hydrophilicity and hydrophobicity in contact with bitumen. Moreover, Cuthiell et al. [25] used a 2D model microchannel to study mass transfer of toluene in bitumen. They also evaluated viscous fingering and internal mixing of the solvent in bitumen using CT-scanner and X-ray. In the presented work, we measure diffusion of hexane into Athabasca bitumen using microfluic and x-ray scanning approaches. Interface of solvent bitumen is monitored over the time and images are analyzed to calculate concentration profile of the solvent at different elevations. The goal of this work is to calculate mutual diffusion coefficient for both methods and compare the two techniques in terms of active diffusion mechanism, asphaltene precipitation and study the possible effect of channel/pore size on diffusion.

4.1.1. Identification of Diffusion Mechanism

Based on mathematics investigated in detail elsewhere [20], diffusion composition profiles can be superimposed if plotted against $\text{distance}/\text{time}^{n_w}$, where distance is defined from interface and n_w is the fitting parameter and ranges between 0.25 and 0.5. Two extreme values of 0.25 and 0.5 correspond to single file and Fickian diffusion respectively and any values in between correspond to a mixed diffusion. Determination of values of the fitting parameter and their uncertainty is explained in detail elsewhere [20].

4.2. Experimental Section

4.2.1. Materials and Fabrication Method

Research grade hexane (99.5%) with a density of 655 $kg.m^{-3}$ at room temperature, sulfuric acid, and hydrogen peroxide were purchased from Sigma-Aldrich. Athabasca bitumen (Alberta,

Canada) with a density of 1012 $kg.m^{-3}$ and a viscosity of 517.3 $kg.m^{-1}.s^{-1}$ at room temperature was received from Alberta InnoTech and used with no further treatment.

T-shaped micro-channel was fabricated using 4 inch × 4 inch × 0.043 inch borofloat (81% SiO_2, 13% B_2O_2, 4% Na_2O/K_2O, 2% Al_2O_3) glass wafer. Wafers were cleaned using piranha solution (H_2SO_4 and H_2O_2 with 3:1 volume ratio) and then rinsed using de-ionized water. Layers of Cr (75 nm) and Au (180 nm) were coated on the wafer (masking layer). HPR 504 photoresist was spun onto the wafer and baked for 30 minutes and then exposed to light to transfer the designed pattern. Au and Cr layers on photomask pattern were removed with Potassium Iodide (KI). Borofloat glass was then wet etched using hydrofluoric acid (HF) for the specific time (etching rate was around 1.4 μm/min) to obtain desired channel depth. Finally, the patterned wafer and top substrate with reservoir holes were cleaned and pressed together to form interfacial temporary bonding due to pure Van der Waals forces [26].

According to our measurement and literature, bitumen density at room temperature lies between 1.01 to 1.04 g/cm^3 [27]. Asphaltene, as the insoluble fraction of bitumen in hexane, precipitates during the diffusive mass transfer mechanism [27]. They have a density of 1.15 gr/cm^3 at room temperature [28]. The effect of asphaltene on bitumen density was evaluated with density measurements. For this purpose, bitumen was separated into asphaltenes and maltenes using hexane with the bitumen/hexane volume ratio of 1/40. The mixture was then shaken for 30 minutes at 14000 rpm and filtered to separate asphaltene. Maltene was recovered by evaporation of solvent. Densities of original bitumen and maltene were 1.024 and 0.996 gr/cm^3, respectively that expressed a little difference. Therefore, bitumen density was applied for numerical simulations.

4.2.2. Experimental Platform

4.2.2.1. T-shaped Microchannel

As shown in Figure 4.1a, microchannel (600 µm width, 50 µm depth, and 12 mm length) was slowly loaded with bitumen using a glass syringe. Hexane was injected from the inlet pushing the air towards the outlet of the channel. All the experiments were carried out under ambient pressure and room temperature (23±0.5 °C). Consistency of the temperature was monitored using a surface-mounted thermocouple (CO 1, Cement-on Thermocouple, Omega Engineering Inc., USA). A white light optical microscope (ZESIS Axio Lab.A1) coupled with a high-speed CCD camera (ZESIS AxioCam 105 Color) was used to record the images at bitumen-hexane interface every second for 1600 seconds, and images were transferred to a computer for analysis. Figure 4.1b represents T-shaped glass microchannel with the region of image used for the image analysis. High width to depth ratio of the channel led to one-dimensional diffusion of the hexane into bitumen and enabled us to calculate mass fraction of solvent in bitumen with focus on a small area of the interface.

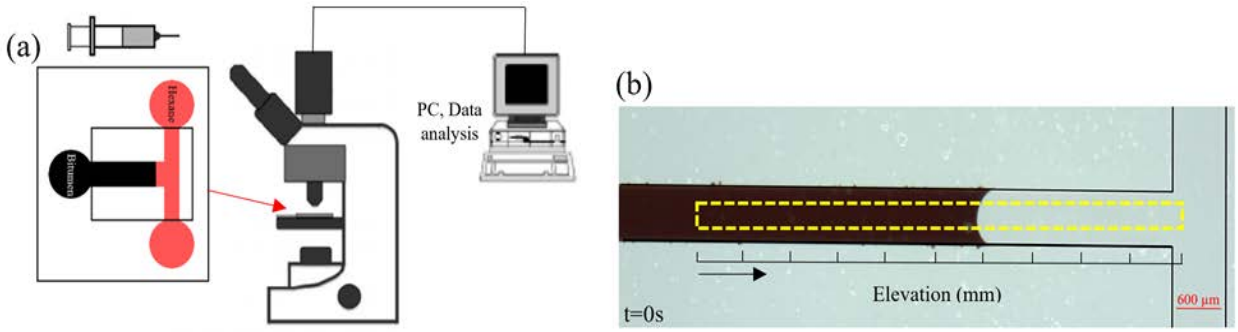

Figure 4.1. Schematic of microfluidic setup for hexane-bitumen diffusion mass transfer. (b) bitumen-hexane interface at t=0s with the area of the image used for diffusion mass transfer study (dashed yellow rectangle) at different elevations from left (bitumen-rich side) to right (solvent-rich side).

4.2.2.2. X-ray Scanning Technique

X-ray technique was developed around 20 years ago and was used to study diffusion and phase behaviour of various mixtures. X-ray beam would be sent through the sample and a camera would process the intensity into black and white images. Here we used an X-ray view-cell with a resolution of 150 μm/pixel and frame capture speed of 300 images/s. X-rays are sent by a tungsten source and passed through the vial and then intensified with an image intensifier and picked up by a video camera. The source, vial and camera are placed inside an isolated cabinet with a thermostat that enables constant room temperature measurements without any disturbance. Details and workflow of the apparatus are explained elsewhere [29] . Bitumen was first heated and then poured into a glass vial with a diameter of 20 mm and a length of 60 mm. The sample was left overnight inside the cabinet to reach equilibrium with the surrounding. Solvent was then injected on top and images were taken until a maximum of 12hr. Figure 4.2a shows a sample of vial inside which diffusion of hexane in Athabasca bitumen is occurring and Figure 4.2b shows the black and white digital image taken by the camera.

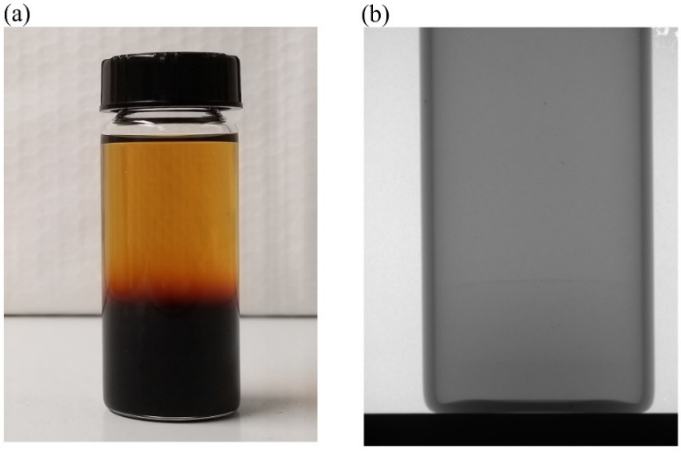

Figure 4.2. Sample of vial for x-ray scanning of bitumen-hexane diffusion

4.3. Theory

A sharp boundary was noticed between hexane and bitumen initially (t = 0). Dilution of bitumen and composition change was captured through the variation of transmitted light intensities as shown in Figure 4.3. Smoothed and averaged values of the intensities were calculated at each elevation to minimize the noise effects. Over time intensity of the bitumen side is increasing and solvent's is decreasing. It is noteworthy to mention that asphaltene precipitation was noticed and recorded during the diffusion process.

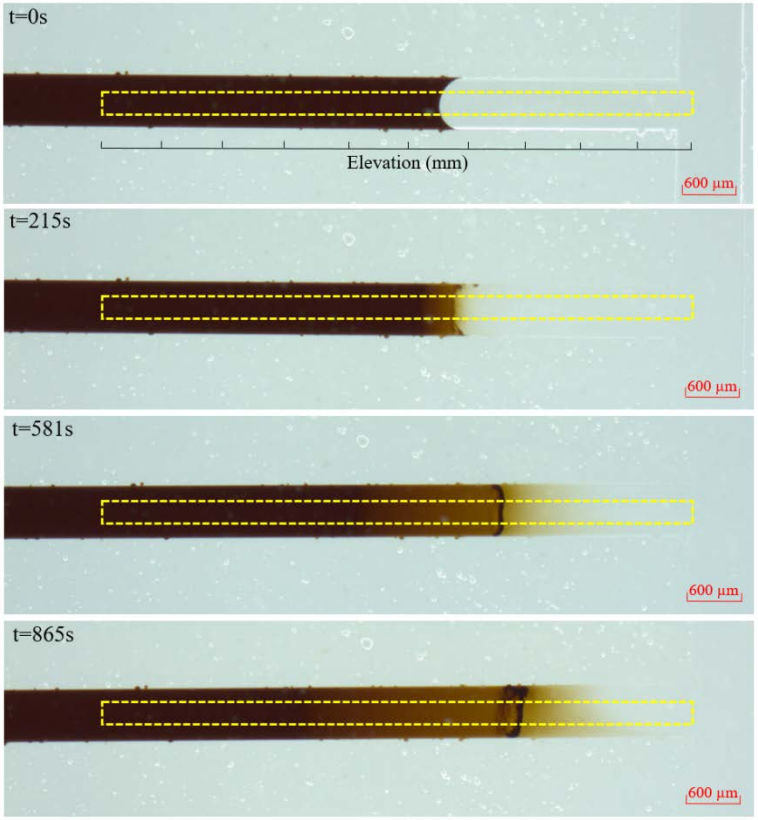

Figure 4.3. Time-lapsed images for hexane bitumen interface in T-shaped micro-channel before the injection of hexane (t=0), and mutual diffusion of hexane and bitumen over time.

Local intensities of captured images are transferred to solvent mass fraction with the Beer-Lambert law. As mentioned by Zhang et al. [13], it relates intensity of the transmitted light to the

absorbance (ε), density (ρ), and thickness of the sample (Δx) for a fixed incident intensity (I_0) as below:

$$I = I_0 \exp(-\rho \varepsilon \Delta x) \qquad (4-1)$$

In a non-reactive mixture, where volume of the mixing is zero, local density of the mixture at different elevations is a function of mass fraction as:

$$\rho = w_{hex}\rho_{hex} + (1 - w_{hex})\rho_{bit} \qquad (4-2)$$

Combining Eq. (4-1) with Eq. (4-2), the local mass fraction of solvent at different elevations is related to transmitted intensities of pure solvent (I_{hex}) and bitumen (I_{bit}) and local intensity of the mixture (I) as shown in Eq. (4-3) [30]:

$$w_{hex} \approx \ln\frac{I}{I_{bit}} \Big/ \ln\frac{I_{hex}}{I_{bit}} \qquad (4-3)$$

As mentioned by Bird et al. [30], the fundamental equation for diffusion is continuity equation that would be simplified to Eq. (4-4) with the assumption of diffusive dominated and one directional mass transfer:

$$\frac{\partial(\rho_w . w)}{\partial t} = \frac{\partial}{\partial x}\left(\rho_w D \frac{\partial w}{\partial x}\right) \qquad (4-4)$$

Where t is time, x is distance, D is the mutual diffusion coefficient, w is the mass fraction of solvent, and ρ is the density. Fadaei et al. [32] used a calibration curve for correlation of mass and light intensity. They represented a concentration crossover around 0.5 during the time as expected for Eq. (4-5) as the solution of diffusion-based mass transfer equation for constant diffusion coefficient in a semi-infinite boundary condition [33].

$$\frac{C(x,t)}{C_0} = \frac{1}{2}\left(1 - \text{erf}\left(\frac{x}{\sqrt{4Dt}}\right)\right) \qquad (4-5)$$

They used toluene as solvent that dissolves bitumen entirely. Other widely used and preferred solvents are n-alkanes such as pentane and hexane which result in asphaltene precipitation. A few studies have investigated diffusion of different solvents in heavy oils a summary of which is surveyed in table 4.1, however, they could not detect asphaltene precipitation due to their large cell dimensions while crossover point and diffusion could be affected by presence of asphaltene [34].

Table 4.1. Literature regarding diffusion of n-alkanes in heavy oils

Mixture	Equipment	Cell diameter (mm)	Reference
Pentane + Athabasca bitumen	X-ray scanning	37	[30, 13]
Toluene + Cold Lake bitumen	Laser Transmission Imaging	100	19
Pentane + Athabasca atmospheric residue	X-ray scanning	37	29
Pentane and Heptane + Athabasca bitumen	Spinning Disk Technique	N/A	34
Heptane + Cold Lake bitumen	X-ray scanning	50	36
Heptane and Hexane + Cold Lake bitumen	Nuclear Magnetic Resonance	25	37
Pentane + Athabasca bitumen	X-ray scanning	50	36

There are some reports for an averaged value of diffusion coefficient instead of concentration dependent coefficient. Fu and Philips [38] measured diffusion coefficient of solvents like pentane, hexane, and heptane into deasphalted bitumen solution. A linear relation between concentration and $t^{-0.5}$ was reported and diffusion coefficient was calculated from the slope of the line. Diffusion coefficient is a function of composition, temperature and pressure. However, the

reported values for diffusion coefficient of solvents in bitumen confirms that it is in the order of 10^{-11} to 10^{-8} $m^2.s^{-1}$ [13] and not a big number with high variation. Therefore, having a true average value seems to be reasonable enough for some rough calculations and modeling. On the other hand, some researchers have reported diffusion coefficient as a function of concentration [37, 39, 40]. As mentioned by Oballa and Butler [19], concentration dependent diffusion coefficient using Boltzman's transformation at constant density can be derived as the following equation:

$$D_{C_1} = -\frac{1}{2t}\left(\frac{\int_0^{C_1} x\, dC}{(dC/dx)_{C_1}}\right) \qquad (4-6)$$

Where C_1 is any concentration between 0 and initial concentration of solvent. This approach is applied for semi-infinite system where physical boundaries of T-shape microchannel and X-ray techniques are large enough to satisfy.

4.4. Results and Discussions

Figure 4.4. represents applied steps to calculate transmitted intensities at various elevations from the image at one of the time-steps (t=0) (see the supporting video (s1) for hexane diffusion in bitumen in T-shaped microchannel).

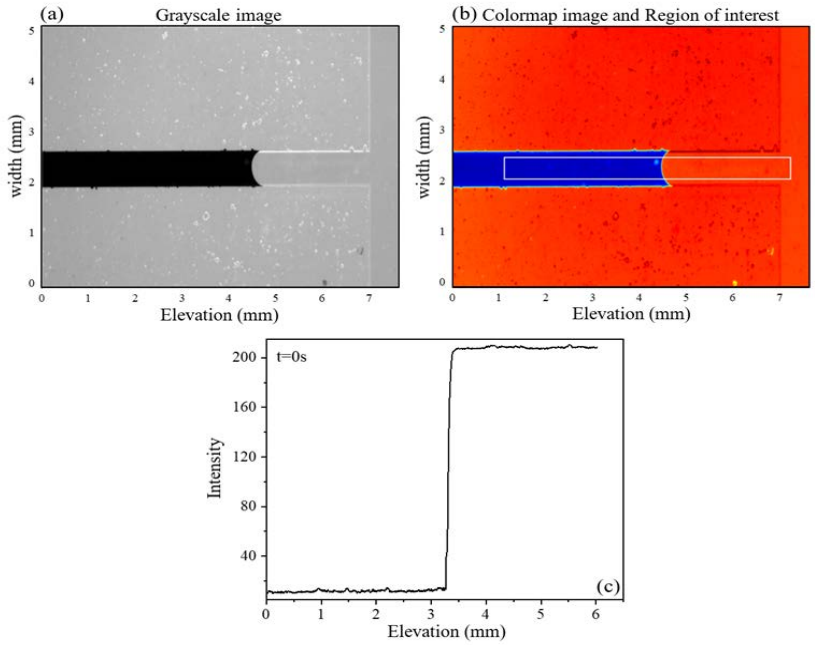

Figure 4.4. (a) Grayscale image of bitumen-solvent interface. (b) colormap image and selected region for intensity measurement. (c) Light intensity at t=0s before diffusion process for bitumen (right side) and hexane (left side).

Mass fraction of hexane was calculated using Eq. (3) and intensities captured from the images. Figure 4.5 shows time-lapsed mass fraction profiles as a function of elevation for T-shaped microchannel (figure 4.5a) and X-ray technique (figure 4.5b). A sudden reduction of intensity (concentration) at the interface was noticed in the range of 0.6 to 0.8 hexane mass fraction that is above the critical solvent:bitumen ratio where asphaltene starts to aggregate and precipitate [41].

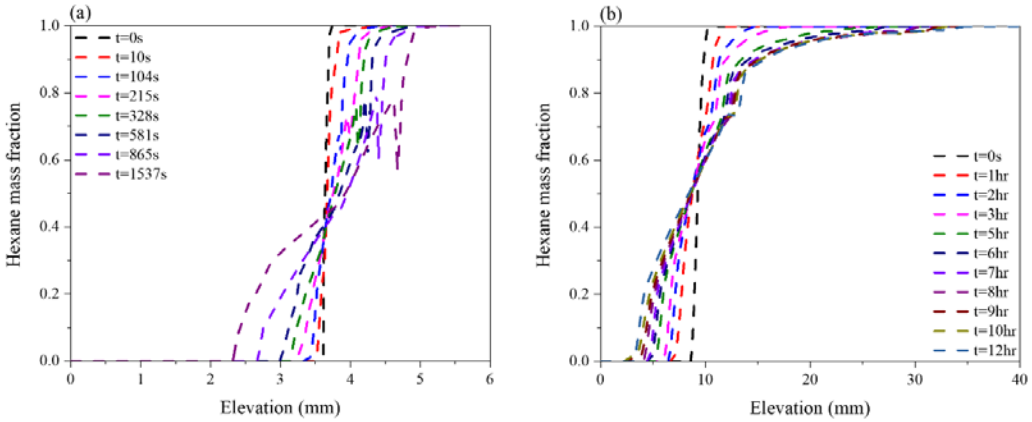

Figure 4.5. Time-lapsed hexane mass fraction as a function of elevation in (a) T-shaped microchannel and (b) X-ray technique

4.4.1. n_w Values for T-shaped Microchannel and X-ray Methods

The optimum values of n_w for each mass fraction was evaluated to understand the diffusion mass transfer mechanism. Figure 4.6 shows local values of n_w against hexane mass fraction for microfluidic (figure 4.6a) and X-ray (figure 4.6b) approaches. Values of n_w are around 0.5 at almost all hexane mass fractions which shows dominance of Fickian behavior as an accurate estimation for both methods.

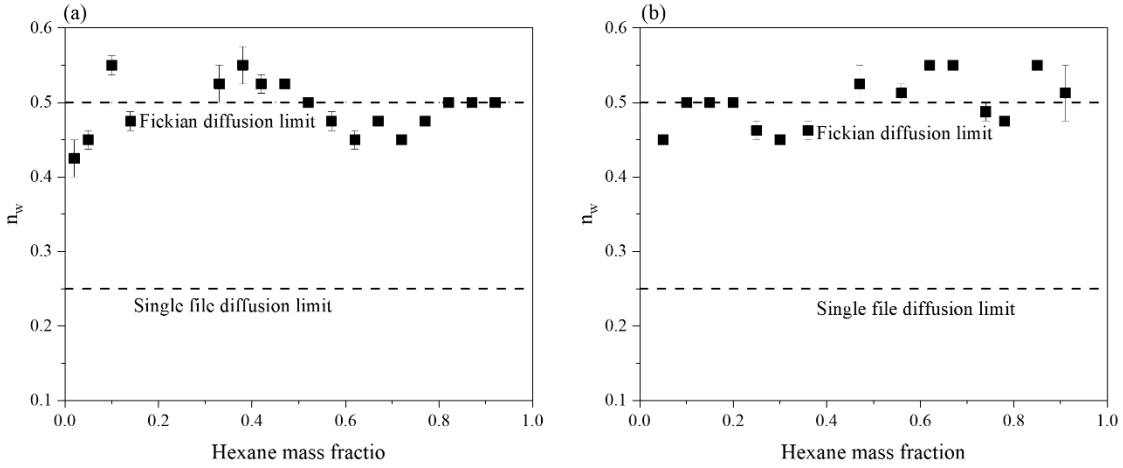

Figure 4.6. T-shaped microchannel (a) and X-ray technique (b) exponent values for Athabasca bitumen + hexane mutual system

As illustrated in Figure 4.7, superimposition of composition profiles plotted against elevation/time$^{0.5}$ also confirmed the accuracy of Fickian mass transfer mechanism for micro-channel and X-ray approaches. Fadaei et al. [32] showed divergence in composition profiles at low solvent concentrations (i.e. < 0.2). This was attributed to complex nature of bitumen and its semisolid structure. While bitumen has diverse interactions with different solvent, Fickian diffusion was the only mass transfer mechanism considered in their work. Bitumen has nano-sized structural spaces that remains unaffected in presenct of aromatic solvents such as toluene [20]. This means diffusion mass transfer mechanism could be Single-File diffusion or a

combination of Single-File and Fickian diffusion. Therefore, assumption of just Fickian diffusion increased the deviation of superimposed data at lower concentrations. In case of addition of n-alkane solvents like hexane to bitumen, aggregation happens in large volume with growth of nano structured fractions to micro sized aggregates [42] as depicted in Figure 4.3. This is in accordance with n_w values of our experiments that confirms Fickian mass transfer mechanism during the addition of hexane to bitumen.

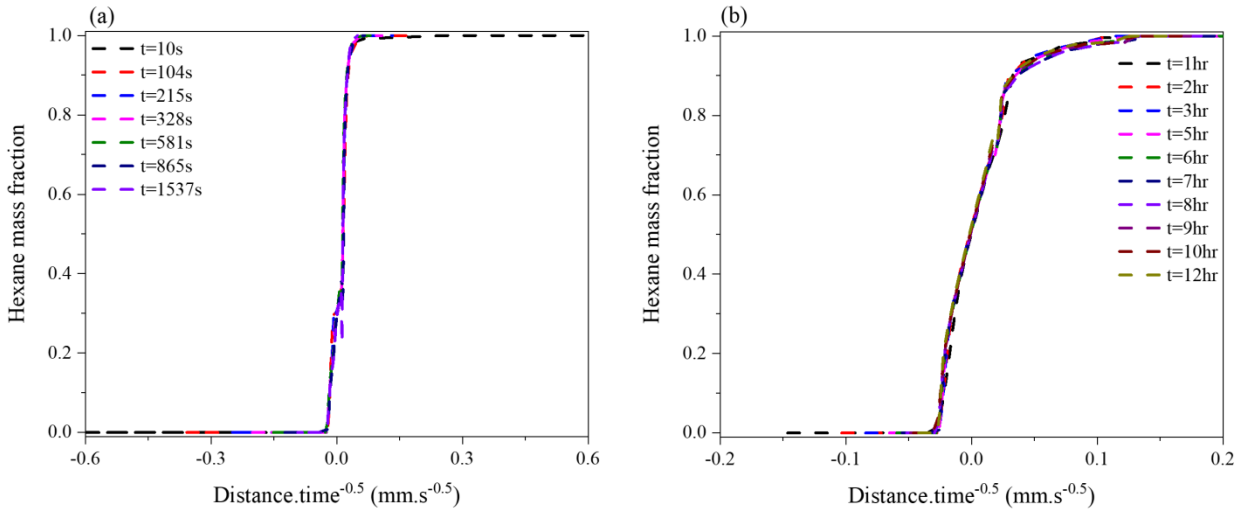

Figure 4.7. Superposition of time-lapsed hexane concentration profile in T-shaped microchannel (a) and X-ray technique (b) versus distance.time$^{-0.5}$

4.4.2. Constant and Variable Diffusion Coefficients

4.4.2.1. Constant Diffusion Coefficient

After evaluation of diffusion mass transfer mechanism, diffusion coefficient was evaluated using numerical solution of the Fickian diffusion equation. It is worth mentioning that due to the small size of microchannel, the effect of gravity is neglected while gravity is effective is real reservoir condition. For the first section, diffusion coefficient was calculated as a constant value

based on the minimum deviation between experimental and simulation results. Deviation was minimized using Average Absolute Relative Deviation (AARD) as shown below:

$$\text{AARD}\ (\%) = \frac{100}{N}\sum_{i=1}^{N}\left|\frac{x_{exp}^2 - x_{calc}^2}{x_{exp}^2}\right| \qquad (4-7)$$

Here N is the number of data points, x_{exp} is the experimental mass fraction of hexane and x_{calc} is the numerical simulation mass fraction. The optimum values of diffusion coefficients for T-shaped microchannel and X-ray were 2×10^{-10} and 1.8×10^{-10} $m^2.s^{-1}$, respectively. Figure 4.8 shows the experimental and simulation concentration profiles as a function of elevation for X-ray technique. There is a good agreement between experimental and simulation data based on optimum diffusion coefficient. Deviation is observed at very low and very high mass fractions of solvent which is due to slow rates of diffusion in pure bitumen and higher diffusion rates in deasphalted oil respectively. In figure 4.9, different values of diffusion coefficients are considered and one experimental concentration data is compared with simulation data as an example. The maximum deviation is around the dark aggregated asphaltene section where the sharp intensity/concentration reduction was not recognized by Fickian mass transfer equation. While Fickian mass transfer is the dominant mechanism at that area, optical measurement limitations such as 2D top view of the camera did not represent diffusion around the precipitants.

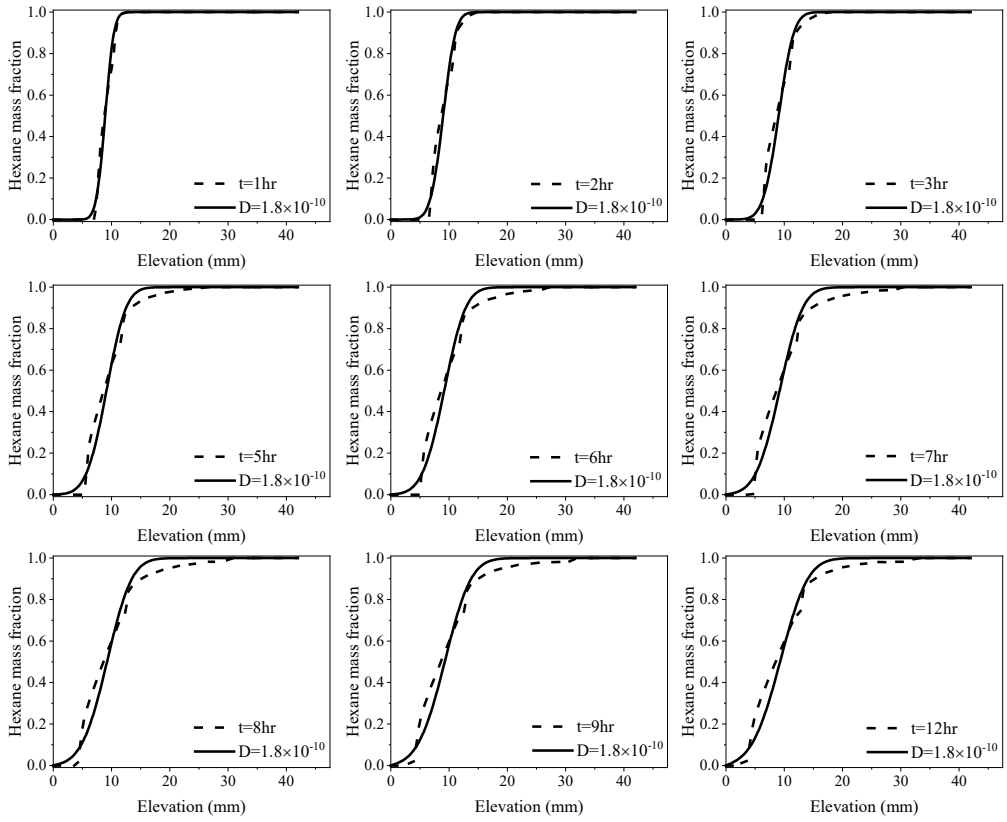

Figure 4.8. Time-lapsed comparison between experimental and simulation concentration versus elevation for X-ray technique

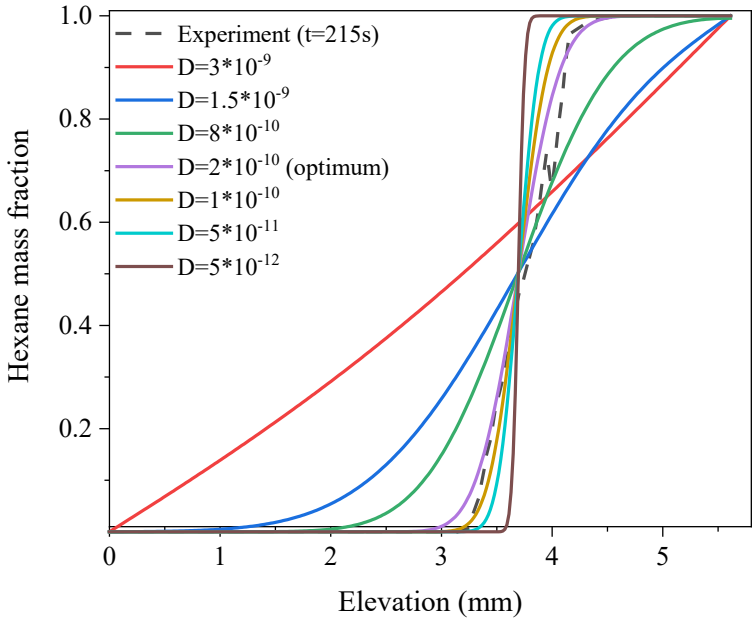

Figure 4.9. Comparison of microfluidic experimental data at t=215s and simulation composition profiles with different diffusion coefficient values.

4.4.2.2. Validation of Simulation

In the next section, mutual diffusion coefficient is determined as a function of solvent mass fraction. The accuracy of numerical simulation was evaluated with diffusion coefficient calculation of a sample concentration profile. For this purpose, equation 4-5 was used to calculate the concentration profile at an arbitrary time with a constant diffusion coefficient of 1.6×10^{-10} $m^2.s^{-1}$(Figure 4.10a). Optimum diffusion coefficients at different concentrations were evaluated that showed a constant value of 1.6×10^{-10} $m^2.s^{-1}$ for the coefficients as expected (Figure 4.10b).

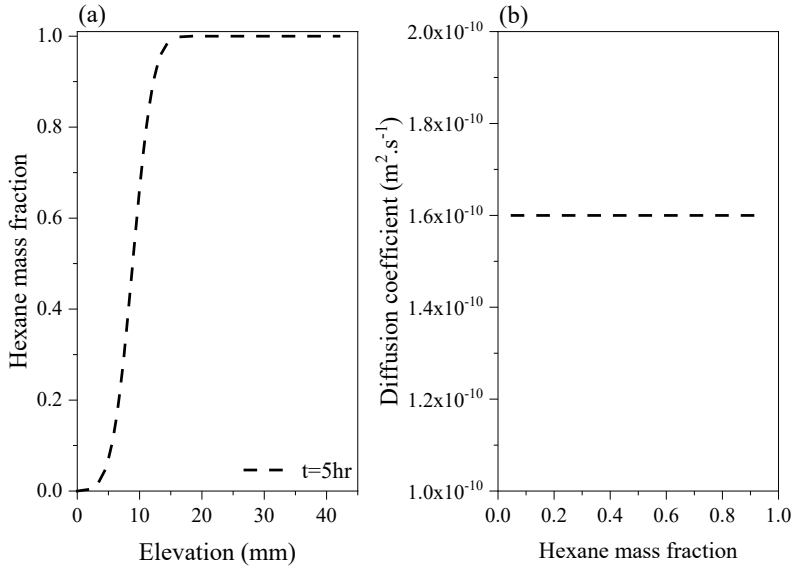

Figure 4.10. (a) Concentration profile based on diffusion dominated mass conservation equation (b) and diffusion coefficient as a function of concentration based on calculated concentration profile.

4.4.2.3. Concentration Dependant Diffusion Coefficient

Diffusion coefficient as a function of hexane concentration is represented in figure 4.11a for T-shaped and figure 4.11b for X-ray technique. The optimum values of diffusion coefficient were calculated based on minimum difference between experimental and simulation concentration data at each concentration point. According to the results, diffusion coefficient is

independent of experiment scale and time frame and both have the same order of magnitude. Calculated diffusion coefficients ranged from 1×10^{-12} to 3.6×10^{-10} $m^2.s^{-1}$ that shows diffusion coefficient is a strong function of concentration and a constant diffusion coefficient assumption cause a large deviation in simulation results. These values are in good agreement with previously reported diffusion coefficients [13, 19, 29, 32]. Bitumen has a large, complex, and semisolid nature compared with hexane molecules, therefore, mutual diffusion is easier at high concentrations of solvent rather than bitumen. This explains the increase in the values of mutual diffusion coefficient for both methods until it reaches a maximum and then it drops the reason to which demands further investigation regarding molecular interactions. This critical point, which has high industrial applications as it possesses the highest diffusion rate, happens at ~0.5 solvent mass fraction for X-ray and at somewhat higher mass fraction for microfluidic approach. This bell-shaped structure has been reported by other authors as well [19, 32]. A high uncertainty of diffusion coefficient was noticed at very low (0-0.1) and high (0.9-1) hexane concentrations because concentration profiles would almost overlap at those regions and calculation of optimum diffusion coefficients was not possible.

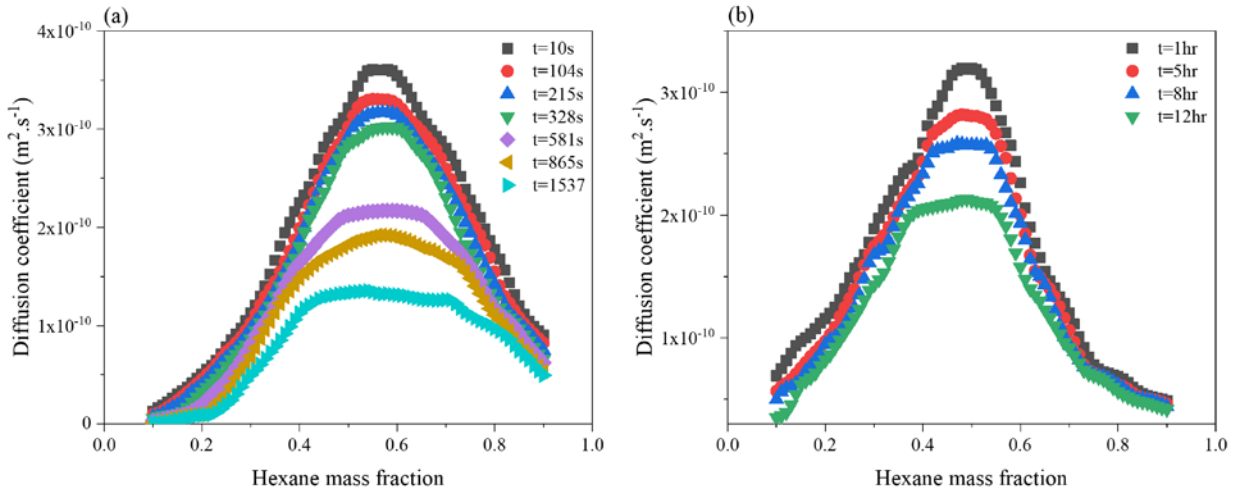

Figure 4.11. Bitumen-hexane mutual diffusion coefficient as a function of concentration for (a) T-shaped microchannel and (b) X-ray technique.

4.5. Conclusion

Understanding of mutual diffusion coefficient and mass transfer mechanism is critically important in solvent based bitumen extraction methods. Two experimental methods with image processing technique were applied to calculate diffusion coefficient and mechanism of diffusion for a careful data processing. Values of mutual diffusion coefficient for both methods fell under the same range. It confirmed that at the same temperature mutual diffusion coefficient is primary dependent on solvent concentration and time scale and size of channel are at most secondary parameters. Hexane, an n-alkane solvent, affects the structure of bitumen by aggregation of nanoasphaltene precipitants and formation of micro structures in bitumen resulting in Fickian mass transfer mechanism. Values of n_w in addition to superimposition of data confirmed Fickian diffusion for both techniques. T-shaped micro-channel enables us to measure binary diffusion coefficient of various solvents and bitumen samples in a faster (less than an hour) and cheaper way than other common methods. This could be very useful for industrial applications towards a better understanding of bitumen extraction with potential solvents.

References

[1] O. V. Trevisan, A. C. L. Lisboa, F. A. França, W. Trindade, “Oil production in offshore fields: an overview of the Brazilian technology development,” World Heavy Oil Conf. 13-15 November, Beijing, China, 2006.

[2] R. M. Butler, “Thermal recovery of oil and bitumen,” Old Tappan, NJ: Prentice Hall Inc., 1991.

[3] J. K. Fairbridge, E. Cey, I. D. Gates, “Impact of intraformational water zones on SAGD performance,” J. Pet. Sci. Technol., 82, 187-97, 2012.

[4] M. Keshavarz, R. Okuno, T. Babadagli, “Efficient oil displacement near the chamber edge in ES-SAGD,” J. Pet. Sci. Eng., 118, 99-113, 2014.

[5] R. M. Butler, I. J. Mokrys, “Recovery of heavy oils using vaporized hydrocarbon solvents: further development of the VAPEX process,” SPE Annu Tech Conf Exhib., 7-9 October, Regina, Canada, 2011.

[6] B. Zhao, M. Becerra, J. M. Shaw, “On asphaltene and resin association in Athabasca bitumen an Maya crude oil,” Energy & Fuels, 23, 4431-37, 2009.

[7] B. Zhao, J. M. Shaw, “Composition and size distribution of coherent nanostructures in Athabasca bitumen and Maya Crude oil,” Energy & Fuels, 21, 2795-2804, 2007.

[8] H. Jobic, K. Hahn, J. Karger, M. Bee, A. Tuel, M. Noack, I. Girnus, G. Kearley, “Unidirectional and Single-File diffusion of molecules in one-dimensional channel system A quasi-elastic neutron scattering study,” J. Phys. Chem., 101, 5834-41, 1997.

[9] K. Hahn, J. Kärger, V. Kukla, “Single-File diffusion observation,” Phys. Rev. Lett., 76, 2762, 1996.

[10] S. Gupta, S. Gittins, P. Picherack, “Insights into some key issues with solvent aided process,” J. Can. Pet. Technol., 43, 54-61, 2003.

[11] S. R. Etminan, “Determination of mass transfer parameters in solvent-based oil recovery processes,” SPE Annu. Tech. Conf. Exhib., 8-10 October, San Antonio, USA, 2012.

[12] M. R. Riazi, “A new method for experimental measurement of diffusion coefficients in reservoir fluids,” J. Pet. Sci. Eng.,14, 235-50, 1996.

[13] X. Zhang, M. Fulem, J. M. Shaw, “Liquid-phase mutual diffusion coefficients for Athabasca bitumen + pentane mixtures,” J. Chem. Eng. Data, 52, 691-94, 2007.

[14] S. K. Das, R. M. Butler, “Diffusion coefficient of propane and butane in Peace river bitumen,” Can. J. Chem. Eng., 74, 985-92, 1996.

[15] S. Bobroff, R. J. Philips, A. Shekarriz, “Nuclear magnetic resonance measurement of ammonia diffusion in dense solid-liquid slurries,” Pacific Northwest National Laboratory, 1997.

[16] M. E. King, R. W. Pitha, S. F. Sontum, “A laser refraction method for measuring liquid diffusion coefficients,” J. Chem. Educ., 66, 787, 1989.

[17] Y. Wen, A. Kantzas, G. J. Wang, “Estimation of diffusion coefficients in bitumen solvent mixtures using X-ray CAT scanning and low field NMR,” 5th Can. In. Petrol., June 8-10 Calgary, Canada, 2004.

[18] A. K. Tharanivasan, C. Yang, Y. Gu, “Measurements of molecular diffusion coefficients of carbon dioxide, methane, and propane in heavy oil under reservoir conditions,” Energy & Fuels, 20, 2509-18, 2006.

[19] V. Oballa, R. Butler, “An experimental-study of diffusion in the bitumen-toluene system,” J. Can. Pet. Technol., 28, 63-90, 1989.

[20] M. Alizadehgiashi, J. M. Shaw, “Fickian and non-Fickian diffusion in heavy oil + light hydrocarbon mixtures,” Energy & Fuels, 29, 2177-89, 2015.

[21] M. Pourmohammadbagher, “Fickian to Single-File diffusion transition in nano-colloids,” MSc Thesis, University of Alberta, Edmonton, Canada, 2018.

[22] V. Berejnov, N. Djilali, D. Sinton, “Lab-on-chip methodologies for the study of transport in porous media: energy applications,” Lab-on-a-Chip, 8, 689-93, 2008.

[23] J. Wan, J. L. Wilson, “Visualization of the role of the gas-water interface on the fate and transport of colloids in porous media,” Water Resour. Res., 30, 11-23, 1994.

[24] K. Keshmiri, S. Mozaffari, P. Tchoukov, H. Huang, N. Nazemifard, “Using microfluidic device to study rheological properties of heavy oil,” AIChE Annu. Meet. San Francisco, USA, 2016.

[25] D. Cuthiell, C. Mccarthy, T. Frauenfeld, S. Cameron, G. Kissel, “Investigation of the VAPEX process using CT scanning and numerical simulation,” J. Can. Petrol. Technol., 42, 41-49, 2003.

[26] H. Moriceau, F. Rieutord, F. Fournel, Y. Le Tiec, L. Di Cioccio, C. Morales, A. M. Charvet, C. Deguet, “Overview of recent direct wafer bonding advances and applications Advances in Natural Sciences,” Nanoscience and Nanotechnology, 1(4), 043004, 2010.

[27] D. Lesueur, “The colloidal structure of bitumen: consequences on the rheology and on the mechanisms of bitumen modification,” Adv. Colloid Interface. Sci., 145, 42-82, 2009.

[28] L. Corbett, “Composition of asphalt based on generic fractionation, using solvent deasphaltening, elution-adsorption chromatography and densimetric characterization,” Anal. Chem., 41, 576-79, 1969.

[29] S. J. Abedi, H. Y. Cai, S. Seifaie, J. M. Shaw, Simultaneous phase behavior, elemental composition and density measurement using x-ray imaging, 158-160, 775-781, 1999.

[30] X. Zhang, J. M. Shaw, “Liquid-phase mutual diffusion coefficients for heavy oil + light hydrocarbon mixtures,” Pet. Sci. Technol., 25, 773-90, 2007.

[31] R. B. Bird, W.E. Stewart, E. N. Lightfoot, “Transport Phenoena,” 2nd ed. New York: Wiley, 2002.

[32] H. Fadaei, J. M. Shaw, D. Sinton, “Bitumen-toluene mutual diffusion coefficients using microtluidics,” Energy & Fuels, 27, 2042-48, 2013.

[33] J. Crank, “The Mathematics of Diffusion,” 2nd ed. London: Oxford University Press, 1975.

[34] M. Ghanavati, H. Hassanzadeh, J. Abedi, “Critical review of mutual diffusion coefficient measurements for liquid solvent bitumen/heavy oil mixtures,” Can. J. Che. Eng., 92, 1445-66, 2014.

[35] E. W. Funk, “Behavior of tar sand bitumen with paraffinic solvents and its application to separations for athabasca tar sands,” Can. J. Chem. Eng., 57, 333-41, 1979.

[36] Y. W. Wen, A. Kantzas, “Monitoring bitumen-solvent interactions with low-field nuclear magnetic resonance and X-Ray computer-assisted tomography,” Energy & Fuels, 19, 1319-26, 2005.

[37] B. Afsahi, A. Kantzas, “Advances in diffusivity measurement of solvents in oil sands,” Can. Int. Petrol. Conf., Calgary, Canada, 2006.

[38] B. C. H. Fu, C. R. Phillips, “New technique for determination of diffusivities of volatile hydrocarbons in semi-solid bitumen,” Fuel, 58, 557-60, 1979.

[39] U. E. Guerrero Aconcha, A. Kantzas, “Diffusion of hydrocarbon gases in heavy oil and bitumen,” Latin American Caribbean Petrol. Eng. Conf., Cartagena de Indias, Colombia, 2009.

[40] A. Fayazi, S. Kryuchkov, A. Kantzas, “Evaluating diffusivity of toluene in heavy oil using nuclear magnetic resonance imaging,” Energy & Fuels, 31, 1226-34, 2017.

[41] A. Yeung, T. Dabros, J. Czarnecki, J. Masliyah, “On the interfacial properties of micrometre–sized water droplets in crude oil,” Proc. Royal Soc. London Ser. A: Math. Phys. Eng. Sci., 455, 3709-23, 1999.

[42] B. Long, M. Chadakowski, J. M. Shaw, “Impact of liquid-vapor to liquid-liquid-vapor phase transitions on asphaltene-rich nanoaggregate behavior in Athabasca vacuum residue + pentane mixtures,” Energy & Fuels, 27, 1779-90, 2013.

Chapter 5: Capillary Flow Analysis using Microfluidic Platform

Asphaltene precipitation and deposition along with dilution of bitumen was represented in chapter 4. Diluted bitumen that was upgraded due to asphaltene deposition is flowing though the porous media toward the production well. Visualization of bitumen flow in microchannel improves pore-scale knowledge of heavy oil and bitumen recovery.

5.1. Introduction

Application of solvents in bitumen and heavy oil recovery are potential methods for the next recovery generation. Solvent based methods have advantages such as less energy consumption and environmental impacts as well as in-situ upgrading compared with present methods like SAGD. Despite high potential of solvent and solvent-steam methods in laboratory scale, main mechanisms, performance and economic aspects are not well-understood [1]. Understanding of these challenges improves the mathematical modeling and numerical simulation with reliable predictions of process. Ambiguities can be categorised into micro-level and macro-level. Although macro-scale success of a recovery technique is largely affected by micro-level events, physics of the process at pore-level are not truly evaluated yet.

Solvent based processes are affected by three main forces including capillary, viscous and gravity forces [2]. Understanding of these forces and related parameters such as interfacial tension, wettability and pore sizes are critically important to analyze these methods.

A version of this chapter presented in Proceedings of the ASME 5th Joint US-European Fluids Engineering Summer Conference FEDSM2018.

Generally, capillary action drives fluid motion in microchannel without external driving forces and capillary interface [3]. Oil sand reservoirs have pore sizes in order of ten to hundred microns and understanding fluid flow in these pores is critically important to have higher recovery in macro-scale. However, flow of liquid in porous media is one of the main challenges in both conventional and unconventional oil recovery. This topic is still not cleared due to the experimental challenges in visualizing this phenomenon.

In recent years, micromodels have proven to be an easy and economical representative tool for conducting small-scale experiments which provide an opportunity to discover yet unrecognized processes and enhance the understanding of existing theories and assumptions [4]. Micro and nanofluidic devices have received attention during the last two decades due to the fast and cheap fabrication, possibility of working at high temperature and pressure, and monitoring of fluid flow [5]. They have a wide range of application in different fields of science such as energy, oil recovery, biomedical [6], etc. More realistic representation of porous media can be shown by periodically constricted capillary microchannels. There are interconnected narrow and wide spaces between the particles to show expansion and constriction effects on capillary-driven flow. Sharma and Ross [7] studied the kinetic of silicon oil into a single sinusoidal tube and derived an equation to study liquid penetration. More recently, Berthier et. Al [8] worked on capillary flow in piecewise varying cross section microchannels and developed an analytical model for dynamic of capillary filling.

Modification of surface properties has been applied in lots of processes such as organic electronics [9], oil recovery [10], nonaqueous phase liquid contaminant transport [11] geological carbon sequestration [12], etc. Surface modification alters the wettability that is an important parameter on capillary flow and displacement process in porous media [13]. Organosilane

compounds can change surface energy and surface wettability. Extend of surface coverage, residual unreacted groups and silane distribution are the most important factors on hydrophobic surface formation [14]. In this study, glass etched microchannels with the depth of 10 μm and width of 30 μm were fabricated to monitor the capillary-driven flow of different liquids and the results were compared with the theoretical model. In fact, the size of the microchannel is close to the size of real oil sand porous media in Alberta, Canada. Therefore, it can be used as a suitable model to study and monitor heavy oil and bitumen flow.

Moreover, a periodically constricted capillary was fabricated to study the diluted bitumen capillary flow in non-uniform microchannels. Effects of non-uniformity on fluid flow was evaluated and compared with numerical simulation. Dynamic contact angles were measured and compared with theoretical contact angles. Untreated (hydrophilic), Hexamethyldisilazane (HMDS) treated (less hydrophilic), and Trichloro (1H,1H,2H,2H-perfluorooctyl) silane (PFOCTS) treated (hydrophobic) microchannels were used to study surface modification effect on capillary filling of various liquids.

5.2. Experimental Section

5.2.1. Materials

Pure methanol (HPLC grade, Fisher Scientific), hexane (HPLC grade, Fisher Scientific), toluene (HPLC grade Fisher Scientific) were used to study capillary-driven flow in microchannel. Athabasca bitumen was also provided by Alberta InnoTech. HMDS and PFOCTS were purchased from Sigma-Aldrich for surface treatment purposes.

5.2.2. Microchannel Fabrication and Characterization

Photolithography methods were implemented for microchannels fabrication on 4 inches × 4 inches × 0.043 inches borofloat (81 % SiO_2, 13 % B_2O_2, 4 % Na_2O/K_2O, 2 % Al_2O_3) glass wafers. Wafers were cleaned using piranha solution (H_2SO_4 and H_2O_2 with 3:1 volume ratio) and rinsed with de-ionized water. Layers of Cr (75 nm) and Au (180 nm) were coated on the wafers that acts as the masking layer. Photoresist (HPR 504) was spun onto the wafer and baked for 30 min. Photoresist was exposed to light through a photomask that was previously designed using L-edit software for transferring the designed patterns. Then Au and Cr layers were wet etched with Potassium Iodide (KI) etchant based on photomask pattern. Borofloat glass was etched using Hydrofluoric acid (HF) for the specific time to obtain desired channel depth (etching rate was around 1.4 µm/min). The remaining Au, Cr, and photoresist layers were removed from the wafer. Finally, the etched and unpatterned substrates were cleaned using piranha solution and pressed together to form temporary bonding. The advantage of using temporary bonding is that it enables us to reuse the fabricated channels and reduce the cost of fabrication, accordingly. A general schematic of the fabrication process is illustrated in figure 5.1 [15].

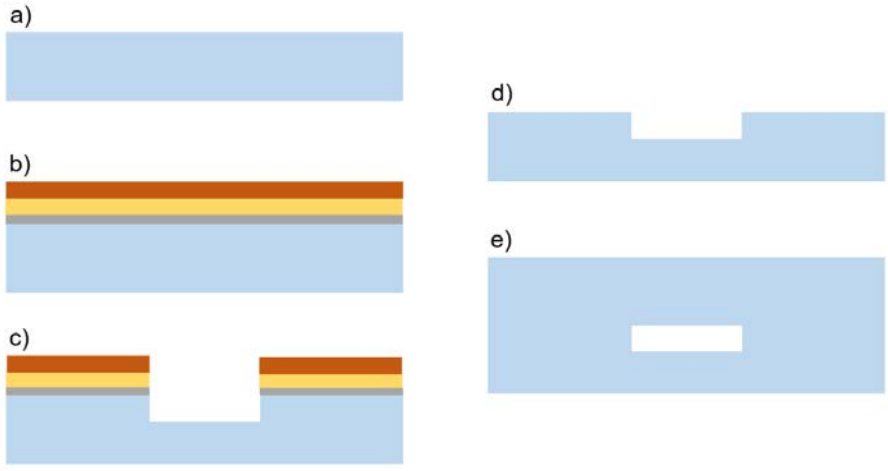

Figure 5.1. Microchannel fabrication process, a) Piranha cleaning, b) Metal layer (Cr and Au) and photoresist coating, c) Development the photoresist, etching the metals and borofloat, d) Removing the metal layers, and photoresist, e) Glass-glass temporary bonding.

Fabricated microchannels were used to measure capillary filling speed and dynamic contact angle for hexane, methanol, toluene, and water as well as bitumen hexane solutions (10% to 60%) using optical microscope with a digital charged coupled device (CCD) camera. In addition to single microchannels, six parallel microchannels were fabricated to evaluate repeatability and reproducibility of the measurements. The schematic of the experiment platform is represented in figure 5.2.

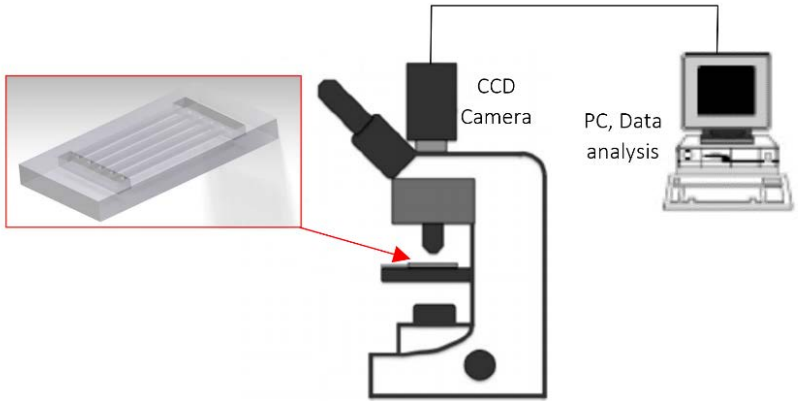

Figure 5.2. Schematic of experimental setup.

5.2.3. Surface modification

Degree of hydrophilicity/hydrophobicity was measured based on water static contact angle as the reference liquid. The coating process for untreated microchannel to less hydrophilic microchannel was conducted in YES HMDS vacuum oven. HMDS and nitrogen directed into the oven (150ºC) with glass substrate to form a monolayer of chemically bonded $Si(CH_3)_3$ which forms hydrophobic property of the wafer surface. HMDS is a monofunctional silane with only bonding to the glass surface with intermediate wetting properties. The water static contact angle increased from 15.4^o on untreated glass to 69.1^o on treated surface as illustrated in figure 5.3.

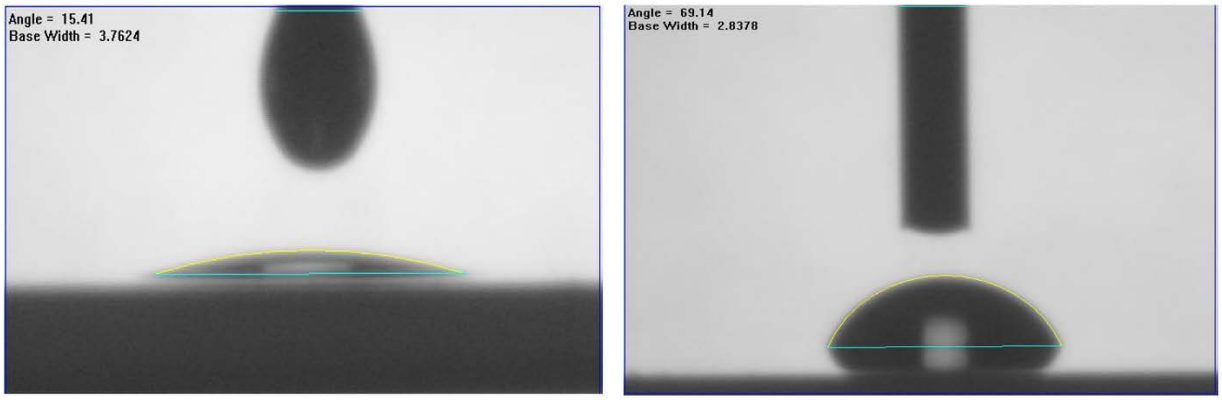

Figure 5.3. Contact angle of untreated (15.4^o) and HMDS treated glass surface (69.14^o)

In addition, glass microchannel was treated using PFOCTS by chemical vapor deposition (CVD) in a vacuum chamber to change the surface chemistry from hydrophilic to hydrophobic. Water contact angle on treated glass wafer was around 115° that is large enough to as a hydrophobic medium (figure 5.4).

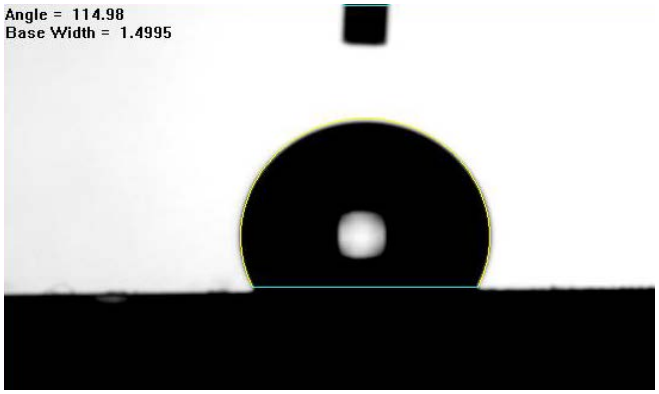

Figure 5.4. Water static contact angle on PFOCTS treated glass wafer.

5.2.4. Characterization

In this study depth, width, and roughness of the microchannels were measured using Zygo Optical Profilometer (NewView 7300, Zygo corporation, Middlefield, CT). The width and depth

for the straight channels were 30.6 µm and 9.8 µm respectively. Periodically constricted capillary has the minimum and maximum width of 14.5 µm and 47.5 µm and depth of 9.8 µm as shown in figure 5.5.

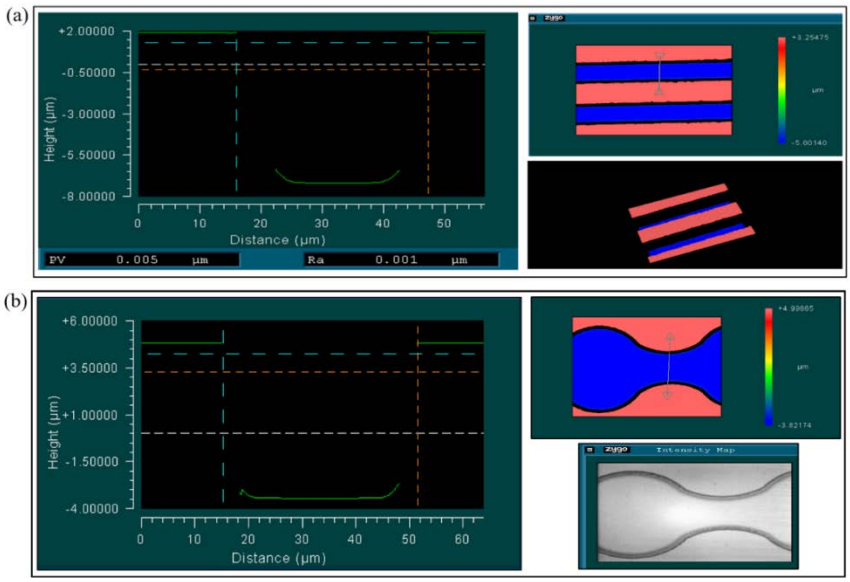

Figure 5.5. Surface profilometer images of (a) parallel microchannel and (b) periodically constricted microchannel

5.2.5. Viscosity, Contact Angle, and Surface Tension Measurement

Viscosity of diluted bitumen samples and pure liquids was measured using rheometer (Rheolab QC, Anton Paar, Austria) equipped with a double gap measurement system. Shear rate was ranged from 1 to 1000 s^{-1}. Measurement for each sample was repeated at least three times and temperature was maintained at 22 ± 0.5 ºC. Bulk contact angle measurements were carried out on a glass surface with the same surface properties as microchannel (i.e. hydrophilicity or hydrophobicity) using FTA 200 equipped with a camera and image analytical program. Same system (FTA 200) was used for measuring air-liquids surface tension (using symmetric pendant drop). Bulk contact angles and surface tensions were measured three times at the room temperature (22 ± 0.5 ºC).

5.3. Theory

5.3.1. Uniform Cross-Section Microchannel

Fluid flow in small-scale channel is different with macro-scale. It is characterized with laminar or stokes flow with low Reynolds number and high impact of capillary forces [16]. As depicted in figure 5.6, capillarity is defined as the surface tension at the solid-fluid interface that minimizes the surface area of the liquid and hence minimizes the energy of the fluidic system [17].

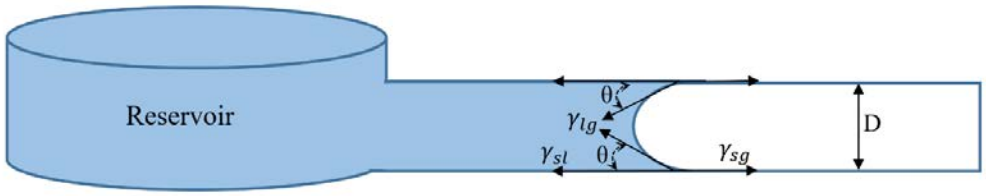

Figure 5.6. Schematic of a single rectangular microchannel

Where θ is the dynamic contact angle, γ_{sg}, γ_{lg}, and γ_{sl} are the solid/gas, liquid/gas, and solid/liquid surface forces, respectively. Yang et al. [17] considered four terms for estimating the total surface energy of the capillary channel including the vacant front area of the microchannel multiplied by γ_{sg}, wetting area multiplied by γ_{sl}, surface energy of the filling reservoir E_0, and surface of capillary meniscus front multiplied by γ_{lg}. Neglecting the last term, the total energy of the capillary microchannel is expressed as,

$$E_t = E_0 + 2(h + w).\left(l \times \gamma_{sg} - x\left(\gamma_{sg} - \gamma_{sl}\right)\right) \qquad (5-1)$$

Where h is the depth and w is the width of rectangular microchannel. Derivative of total energy with respect to flow direction (x) as capillary force leads to Laplace pressure drop equation,

$$F_{ca} = \frac{dE_t}{dx} = 2(h + w).\left(\gamma_{sg} - \gamma_{sl}\right) = \Delta P_{lg}.w.h \qquad (5-2)$$

Considering hydraulic radius of rectangular microchannel ($r = w.h/(w + h)$), Laplace pressure drop across the interface is shown by,

$$\Delta P_{ca} = \frac{2.\gamma_{lg}.\cos\theta}{r} \qquad (5-3)$$

Capillary pressure equation shows the pressure drop increases across the liquid-gas interface when the channel size gets smaller. Experimental analysis of capillary filling kinetic of heavy oil in microchannels and further comparison with the theoretical models improves our understanding of micro-scale fluid transport and wettability phenomena [18]. Fluid-fluid and fluid-surface interaction, geometry, wettability (oil-wet to water-wet), and surface tension are among the important parameters in analyzing of the filling process. Liquids with a wide range of polarity indexes are applied here to see the effect of surface modification on different liquids. Flow of heavy oil in the presence of solvent (live oil) and its time-dependence capillary filling in microchannel as well as dynamic contact angle is evaluated experimentally and compared with classical Lucas-Washburn model [19] that takes both capillary and viscous drag forces into account. Considering dynamic of liquid penetration in the presence of electroosmotic effects along with capillary, gravity, and viscous forces (neglecting inertia term), momentum balance can be written as [20],

$$2\pi r\gamma_{lg}\cos\theta + \rho\pi r^2 g_z l + F_{sh} + F_e = 0 \qquad (5-4)$$

Where l is the liquid penetration in tube, g_z is the z component of acceleration of gravity, $F_{sh}$is the shear force exerted by wall, and F_e is the electroosmotic force. Analytical solution of the momentum balance equation and neglecting the gravitational and eletroosmotic forces, along

with governing equation for laminar flow (Eq. 5-5) leads to Lucas-Washburn equation (Eq. 5-6) as [21],

$$-\frac{\partial P}{\partial x} = -\mu \frac{\partial^2 V_x}{\partial y^2} \qquad (5-5)$$

$$x = \sqrt{\frac{\gamma r \cos\theta\, t}{2\mu}} \qquad (5-6)$$

Where p is the pressure in the fluid, V_x the velocity of the fluid, and μ the viscosity of the fluid. In previous researches, static contact angle has been used in Washburn model [22-24] but in this study, dynamic contact angle is applied as contact angle of liquid on the channel walls. Moreover, average filling speed of advancing meniscus as a function of position is estimated by Eq. (5-7).

$$V_x = \frac{r\gamma \cos\theta}{4\mu x} \qquad (5-7)$$

5.3.2. Non-uniform Cross Section Microchannel

As shown in figure 5.7 for flow of 40% diluted bitumen sample, radius of the tube with sinusoidal axial variation is defined with the periodic function of Fourier series as below:

$$r = r_0 + a_1 \sin\left(\frac{2\pi}{\lambda} l\right) \qquad (5-8)$$

Where r_0 is the average radius, a_1 is amplitude of variation, λ is the wavelength of variation.

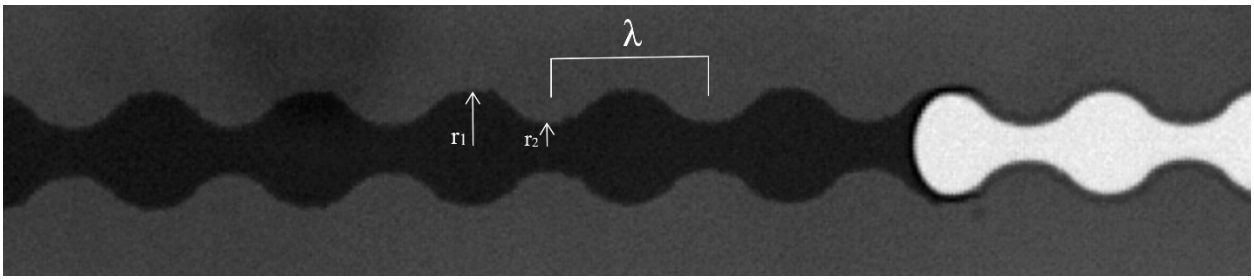

Figure 5.7. Sinusoidal constricted capillary with a pore and pore neck length (λ), maximum (r_1) and minimum (r_2) radius

Assumptions for constricted capillary are: (a) laminar flow with no Haines jump [25], (b) diluted bitumen samples are Newtonian fluid with (c) constant dynamic contact angle as straight microchannel. Meniscus contact angle is modified with the instantaneous slope of the sinusoidal profile as represented in figure 5.8 that total driving capillary pressure can be obtained as,

$$\Delta P_{ca} = \frac{2.\gamma_{lg}}{r}\left[\cos\left(\theta + \tan^{-1}\left(\frac{dr}{dl}\right)\right)\right] \qquad (5-9)$$

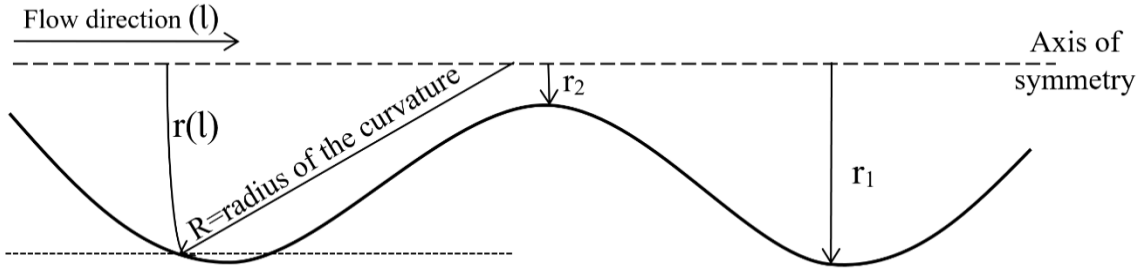

Figure 5.8. Meniscus and effects of contact angle variation

Application of the above consideration to the Navier-Stokes equation gives the inverse of penetration rate of the liquid into sinusoidal constricted capillary as below [7]:

$$\frac{dt}{dl} = \frac{4\mu}{\gamma_{lg}}\left(\frac{r(l)^3 \int_0^l \frac{dx}{r^4(x)}}{\cos\left(\theta + \tan^{-1}\left(\frac{dr}{dl}\right)\right)}\right) \qquad (5-10)$$

This equation is solved numerically to compare experimental and numerical penetration of the liquid as a function of time. In addition, apparent radius r_{app} for the interface at different positions is calculated and experimental and numerical results are compared with theoretical Washburn model using r_{app}. Sharma and Ross [7] solved Washburn equation for t where this solution has the property that:

$$r_{app} = \frac{2\mu}{\gamma_{lg}} \lim_{l\to\infty} \frac{l^2}{t(l)} \qquad (5-11a)$$

Therefore, apparent radius is estimated by,

$$r_{app} = \frac{2}{\cos(\theta)} \left(\frac{1}{\frac{1}{\lambda}\left(\int_0^{\lambda} \frac{r(l)^3}{\cos\left(\theta + \tan^{-1}\left(\frac{dr}{dl}\right)\right)} dl \int_0^{\lambda} \frac{dl}{r^4(l)} \right)} \right) \qquad (5-11b)$$

5.4. Results and Discussion

5.4.1. Reference Fluid

Effect of surface homogeneity of the microchannel on contact angle was evaluated using hexane as a simple pure liquid. Measurement of dynamic contact angle of a reference fluid confirms if the contact angle is constant during the fluid penetration. On that account, surface roughness does not have any obvious impact on contact angle measurements of diluted bitumen as a complicated fluid. As shown in figure 5.9a for hexane flow in parallel hydrophilic microchannles, contact angle is not changing during the capillary flow. In fact, variation of

contact angle was small enough to consider a constant value for theoretical calculations of pure liquids and very diluted bitumen samples (i.e. 10 wt% and 20 wt%). However, according to figure 5.9b, contact angle of 60 wt% bitumen was increasing and flow was slowing down during the penetration. This was confirmed by dynamic contact angle measurement using MATLAB®. In this method, multiple points on the interface edge were selected using an edge detector algorithm and a linear curve was fitted to these points [26]. As an example, contact angle measurement of hexane on hydrophobic glass surface (45°) is shown in figure 5.10.

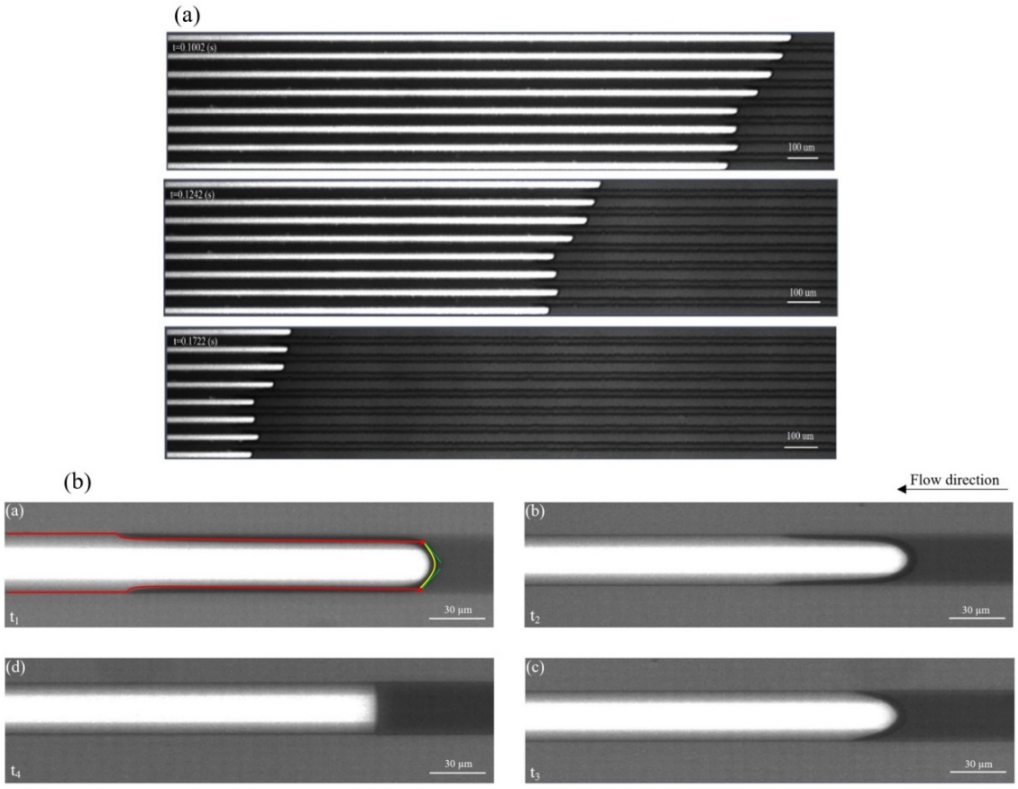

Figure 5.9. Time-lapsed images of capillary flow of (a) hexane and (b) 60 wt% bitumen

Contact angle depends on force balance at contact line that prevails during the capillary filling and therefore, dynamic contact angle is larger than static contact angle [3, 27]. This indicates that application of static contact angle (bulk) for micro and nanochannel fluid flow is not a reliable approach. For instance, Kuo and Lin [3] applied a 23.2° constant static contact

angle in DI water flow in capillary channel using Washburn theory that caused deviation and they mentioned the real dynamic contact angle is different from the static one.

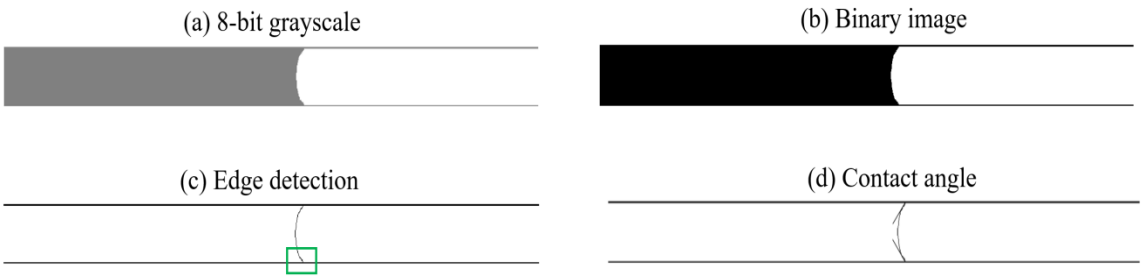

Figure 5.10. Dynamic contact angle measurement using MATLAB

5.4.2. Pure Liquids

Capillary filling kinetic of samples were monitored and recorded at the rate of 45 to 52 frames per second where fluid was injected into a reservoir that is connected to the microchannel. Averaged experimental data for the filling of water, methanol, toluene, and hexane in micro-scale channels were recorded and compared with the theoretical predictions of fluid flow using Washburn equation. The error bars represent 95 percent confidence interval of the average for three experiments at each point. Difference between the experimental and theoretical results were reported in terms of AARD that was mentioned in previous chapter (Eq. 4-7) which x_{exp} is the experimental position of the advancing interface and x_{calc} is the calculated position of advancing interface based on Washburn equation.

The information about the position of moving interface in untreated hydrophilic microchannel was plotted as a function of time and compared with Washburn equation prediction in figure 5.11. For all samples a linear relation between square of propagation distance and time was found as expected in the case of Newtonian fluids and theoretical predictions were

in good agreement with experimental data. However, in the study of capillary-driven flow in nano-confinement geometry, high deviation between experimental results and Washburn theory was reported for water flow by Mozaffari et al. [22]. This deviation was further attributed to the electro-viscous effect and air bubble formation [22]. However, such deviation was not observed in our study herein where microchannels were used. Burgreen and Nakache [28] mentioned that electro-viscous forces are mainly dominant at nano-scale. Moreover, surface conduction and double-layer overlap can affect the flow in nanochannel [29]. Based on recorded images, a thin layer of the fluid is formed in front of the contact line for all the pure liquids moving in the glass system. The formation of thin layer could be due to the evaporation-condensation of the fluid or surface diffusion [21]. This layer confirms what Hardy mentioned [30] about the thin precursor film moves ahead of the contact line. This layer causes advancing contact line moves over a wet surface. However, at high interface velocities, there is not enough time for formation of thin fluid layer and advancing contact line flows over a dry surface [21].

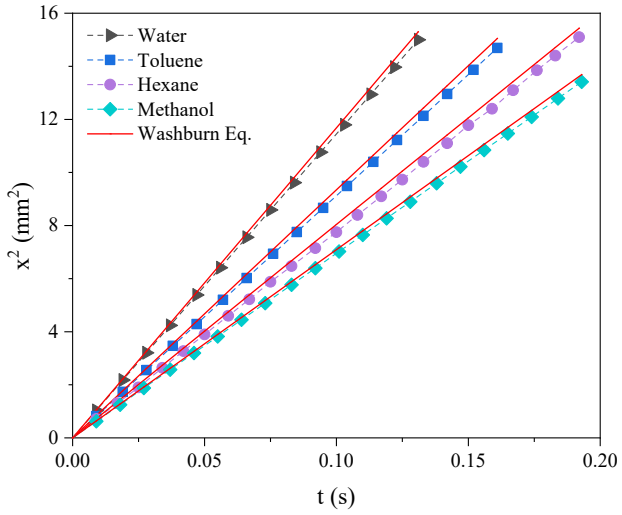

Figure 5.11. Experimental and theoretical comparison of pure liquids filling in microchannel

The position squared of advancing meniscus for different pure liquids as a function of time in HMDS treated microchannel is illustrated in figure 5.12. It shows that all the liquids follow the

linear relation like untreated microchannels. However, the velocity of water in HMDS treated microchannel was found to be lower than the untreated channel. For example, position squared of water interface for untreated microchannel and treated microchannel at t=0.11 s is equal to 12.9 mm^2 and 5.3 mm^2, respectively. This observation agrees with the wetting properties and surface treatment effect on dynamic contact angle and fluid flow, subsequently.

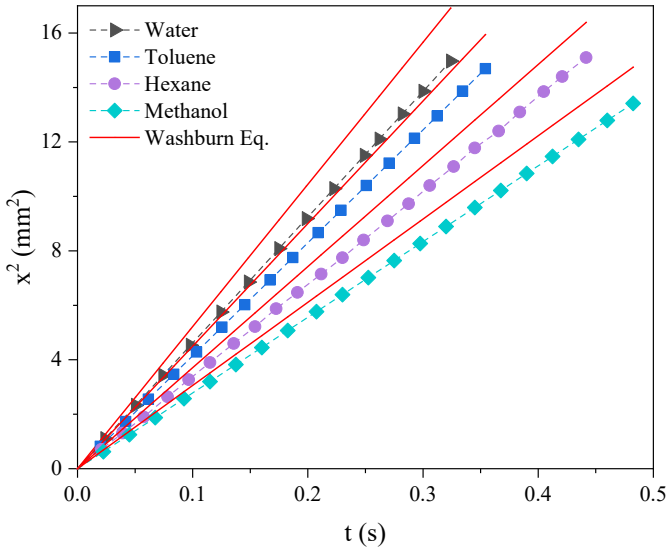

Figure 5.12. Pure liquids penetration in HMDS treated microchannel as a function of time

Although Washburn model (red line) accurately predicted the capillary filling kinetics in the treated microchannel but higher level of deviation was noticed compared with hydrophilic microchannel. In addition to surface treatment, this deviation could be related to the difference between bulk and dynamic viscosity of pure liquids flow in HMDS treated microchannel. In case of water, high level of polarity for untreated microchannel cause to attraction but treatment of microchannel with HMDS reduces the attraction and tendency of water to spread out [31, 32]. Faster penetration of water in untreated microchannel compared with HMDS treated microchannel is represented in figure 5.13.

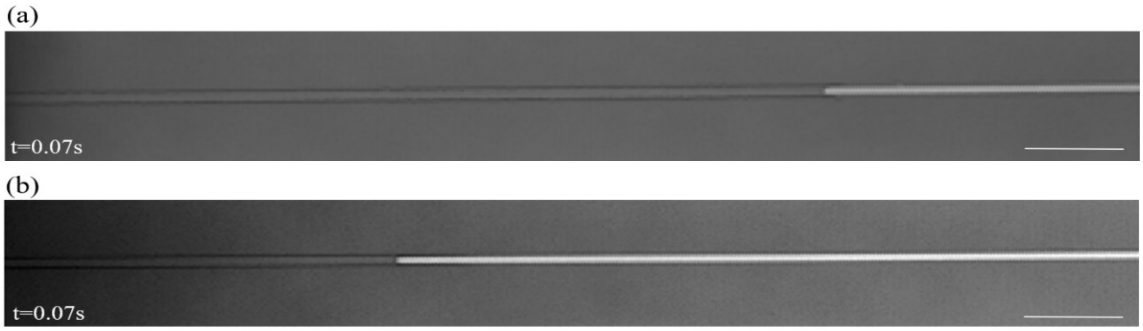

Figure 5.13. Penetration rate of water in (a) hydrophilic and (b) less hydrophilic microchannels at t=0.07s.

Flow of pure liquids in hydrophobic channel was evaluated using PFOCTS coated microchannel. For this section, small droplet of water stayed on the top of the reservoir and did not penetrate in microchannel. This could be related to overcoming the capillary pressure induced by low water wetting [33]. It seems that capillary forces became more dominant that showed the difference between hydrophilic and hydrophobic surfaces. Linear changes of square of position as a function of time is depicted in figure 5.14. However, experimental and theoretical results showed slower fluid flow in PFOCTS microchannel compared with untreated and HMDS treated ones.

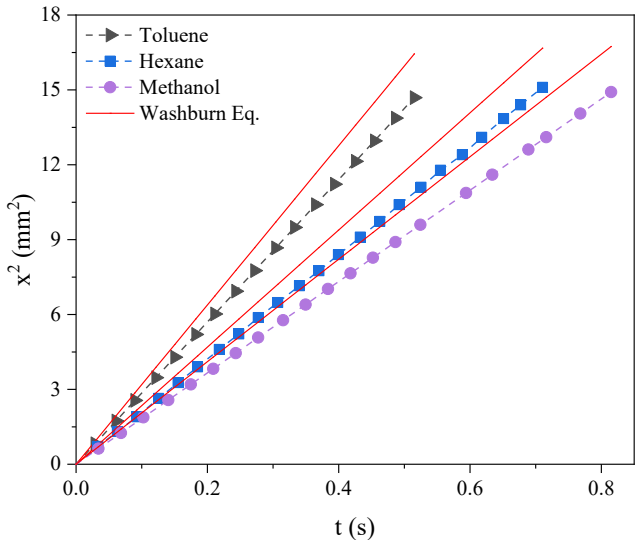

Figure 5.14. Penetration distance of pure liquids in PFOCTS treated microchannel

The higher deviation and slower flow in hydrophobic microchannel could be due to extremely low surface energy of the coated microchannel. All the studied liquids wet the untreated borofloat glass microchannel, indicating that the substrate has a very high surface energy. However, PFOCTS treated microchannel is not wetted by any of the liquids even low polarity ones. This means treated microchannel has an extremely low surface energy. Physical properties, experimental and theoretical contact angles are summarized in table 5.1.

Table 5.1. Pure liquids physical properties, measured, and calculated dynamic contact angles

Liquid	μ[1] (cP)	Surface tension ($mN.m^{-1}$)	Slope ($mm^2.s^{-1}$)			Measured contact angle (θ)			Calculated contact angle (θ)		
			Untreated	HMDS	PFOCTS	Untreated	HMDS	PFOCTS	Untreated	HMDS	PFOCTS
Water	0.96	72.3±0.1	114.5	52.2	-	15	63.5	-	9.5	60	-
Toluene	0.55	28.3±0.2	91.2	41.4	28.5	16	59	69	12.3	55.5	66.4
Hexane	0.3	18.4±0.2	78.6	34.2	21.2	17	63	74	14.5	67.1	71.6
Methanol	0.57	22.6±0.2	69.5	27.8	18.3	13	63	75	11.1	60.3	72.2

[1]Viscosity at room temperature

Pure liquids in untreated, HMDS, and PFOCTS treated microchannels were evaluated. As expected, a decrease in filling speed with penetration of fluid in the channel was recorded. This is due to the constant capillary pressure and an increase in viscous force that act against the flow of the fluid. Washburn equation verifies that viscous drag force increases linearly with the meniscus position and fluid velocity reduces by penetration into the microchannel. However, filling speed of pure liquids is lower than the predicted values obtained from Washburn model. As represented by Kuo and Lin [3], Washburn predicts the flow ideally but there are other

effective forces on capillary flow. Based on velocity profiles, it seems hydrophilicity reduction causes less tendency of wettability and slower fluid flow. As shown in figure 5.15, hexane and water had the highest filling speed in untreated microchannel and it decreased in HMDS, and PFOCTS treated microchannels. For example, hexane velocity at penetration distance of 2.5 mm for untreated microchannel is 15.3 mm/s while it is around 8.6 mm/s and 4.1 mm/s for HMDS and PFOCTS treated microchannels, respectively.

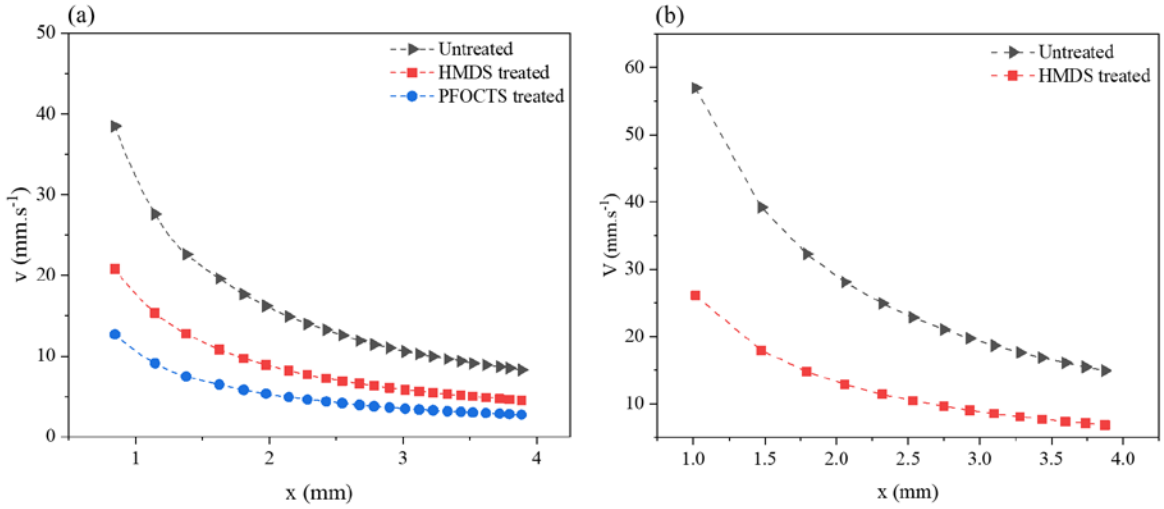

Figure 5.15. (a) Hexane and (b) water filling speed as a function of penetration distance in untreated, HMDS and PFOCTS treated microchannels

5.4.3. Diluted Bitumen Samples

In this section bitumen diluted in hexane (10 wt% to 50 wt%) was used to evaluate the capillary flow in microchannel. Capillary filling of different bitumen samples as a function of time is illustrated in figure 5.16. There is a linear relation between square of position and time. However, as both the bitumen concentration and penetration distance increases the deviation between the theoretical predictions and experimental results increases (e.g. deviation of 14.7%

for 40 wt% and 17.6% for 50 wt% bitumen solution). This could be related to dynamic contact angle constantly changing during the penetration of higher bitumen concentration samples. Previous work in our group [22] reported sharp changes in advancing contact angles for diluted bitumen penetration in nanochannels. This could occur due to the inhomogeneous distribution of very fine residues which alternatively affect the liquid flow and shape of interface at nano-scale. It was also shown that the fluid viscosity in nano-scale can be larger than the measured value of bulk due to the confinement effect [34]; however, such differences are not expected to occur in the micro-scale.

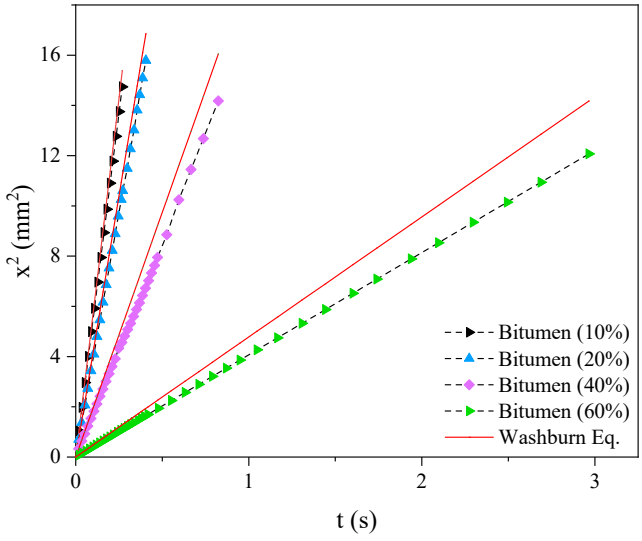

Figure 5.16. Capillary flow of diluted bitumen as a function of time

Advancement of 10% to 60% bitumen diluted in hexane was tracked in HMDS treated microchannel where square of interface position (x^2) changed linearly with time as shown in figure 5.17. Deviation of experimental data from theoretical prediction is increasing with bitumen concentration with the highest deviation of 27.8% for 60% diluted bitumen sample.

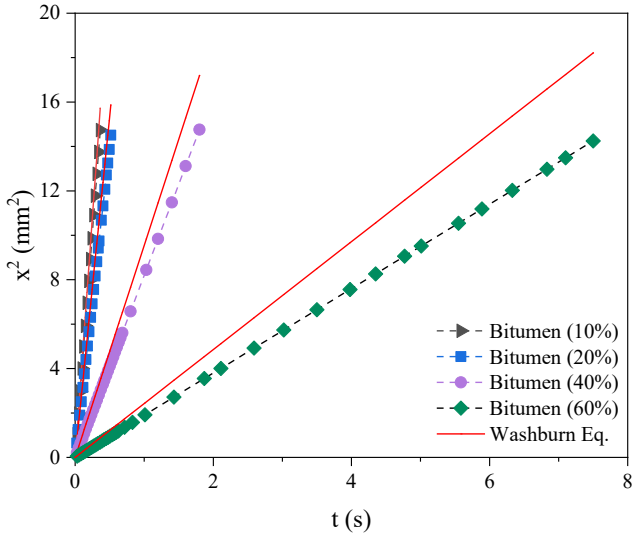

Figure 5.17. Diluted bitumen penetration as a function of time (s) in HMDS treated microchannel

In this section, capillary-driven flow of diluted bitumen in PFOCTS microchannel is evaluated and compared with Washburn model (figure 5.18). Capillary flow of diluted bitumen shows that bitumen concentration enhancement reduces the speed of interface movement and it takes longer time to fill the microchannel. Adhesion of the fluid to the surface is very important specially in higher concentration of bitumen with higher viscosity and higher content of heavy fractions [35]. Another important issue is related to the silane structure. PFOCTS with linear formula of $CF_3(CF_2)_5CH_2SiCl_3$ has a long-fluorinated chain that reduces the surface energy and makes the surface oleophobic and hydrophobic at the same time (i.e. lyophobic) [36]. This explains why diluted bitumen and pure liquids were flowing slower in PFOCTS coated microchannel and they have larger static and dynamic contact angles compared with HMDS treated and untreated microchannels. Details of the physical properties, measure and calculated contact angles are provided in table 5.2.

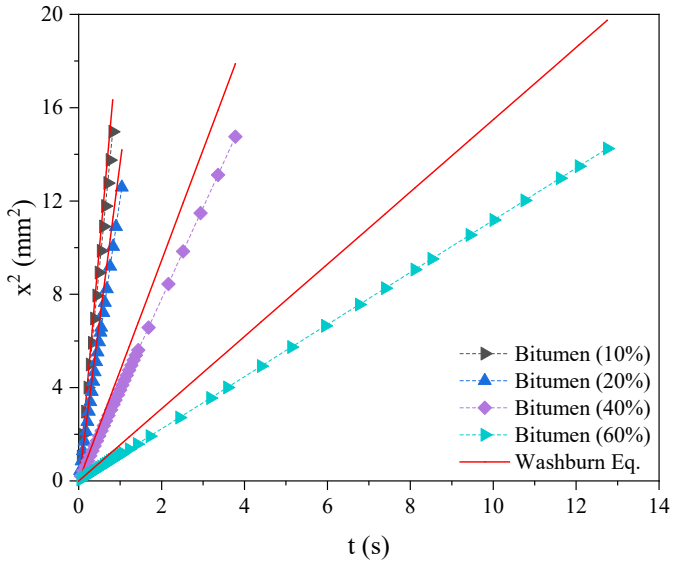

Figure 5.18. Square of meniscus position as a function of time for diluted bitumen

Table 5.2. Physical properties and measured properties of diluted bitumen

Liquid	μ[1] (cP)	Surface tension (mN.m^{-1})	Slope (mm^2.s^{-1})			Measured contact angle (θ)			Calculated contact angle (θ)		
			Untreated	HMDS	PFOCTS	Untreated	HMDS	PFOCTS	Untreated	HMDS	PFOCTS
Bitumen (10%)	0.68	22.3±0.1	54.7	40.5	18.2	13	45	70	10	43.2	67
Bitumen (20%)	1.05	21.5±0.2	38.8	28.1	12.1	17	51	72	12.5	47.4	69.2
Bitumen (40%)	2.1	19.7±0.2	17.1	8.2	3.9	22	59	76	17.4	54.4	71
Bitumen (60%)	3.3	18.8±0.2	4.1	1.9	1.1	28	67	80	24.1	61	74.9

[1]Viscosity at room temperature

Advancing velocity of 40 wt% diluted bitumen as a function of capillary penetration distance by the derivative of the position with time [37] is depicted in figure 5.19. There is a sharp velocity reduction at the entrance due to domination of viscous forces [38] and increasing of drag force with constant capillary force of continues fluid flow following the meniscus front [24], lead

to velocity reduction for all the bitumen samples during the penetration. Resistance forces are in the same order of magnitude in all the microchannels while treated microchannels have slower fluid flow due to lower surface energy and wettability. Comparison of measured dynamic contact angle shows how flow is changing with surface modification. In fact, dynamic contact angle depends on several factors, such as surface roughness, chemistry, and temperature. In the case of monolayer silane modification, the surface roughness is not expected to significantly change. Therefore, contact angle measurement is a function of the surface chemistry.

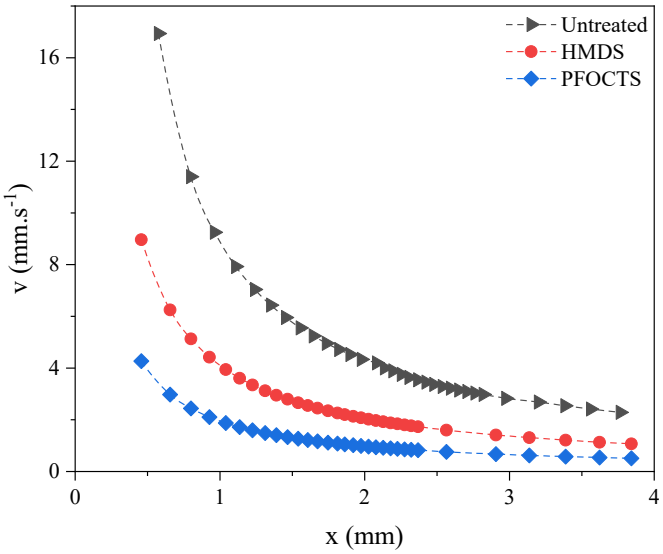

Figure 5.19. 40 wt% diluted bitumen filling speed as a function of penetration distance in untreated, HMDS and PFOCTS treated microchannels

5.4.4. Periodically Constricted Microchannel

To have a more realistic geometrical porous medium, flow of different liquids was evaluated in sinusoidal capillary. Figure 5.20 and figure 5.21 shows the depth of penetration of 40% diluted bitumen in hydrophilic and hydrophobic tubes, respectively. Flow of the liquid in the hydrophilic and hydrophobic periodically constricted microchannels are shown in electronic supplementary information (ESI-1, ESI-2). Meniscus moves faster through the constrictions and this is due to

higher capillary pressure in the constrictions compared with bulges. In fact, capillary pressure is proportional to the curvature of the meniscus and higher velocity at constrictions is related to higher power consumption of the liquid where velocity is proportional to the power consumption [7].

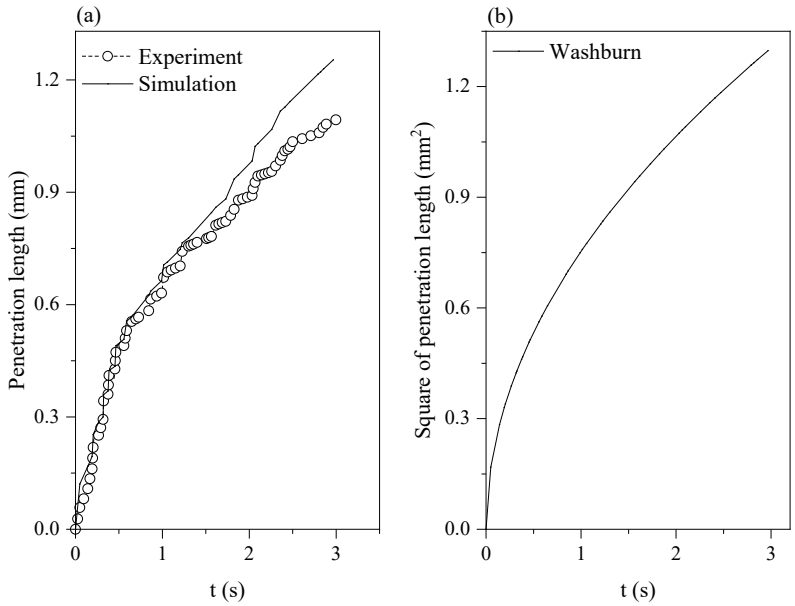

Figure 5.20. Penetration of liquid vs time in hydrophilic microchannel: (a) Experimental data and simulation results using Navier-Stokes equation, (b) Washburn plot (l2 vs t)

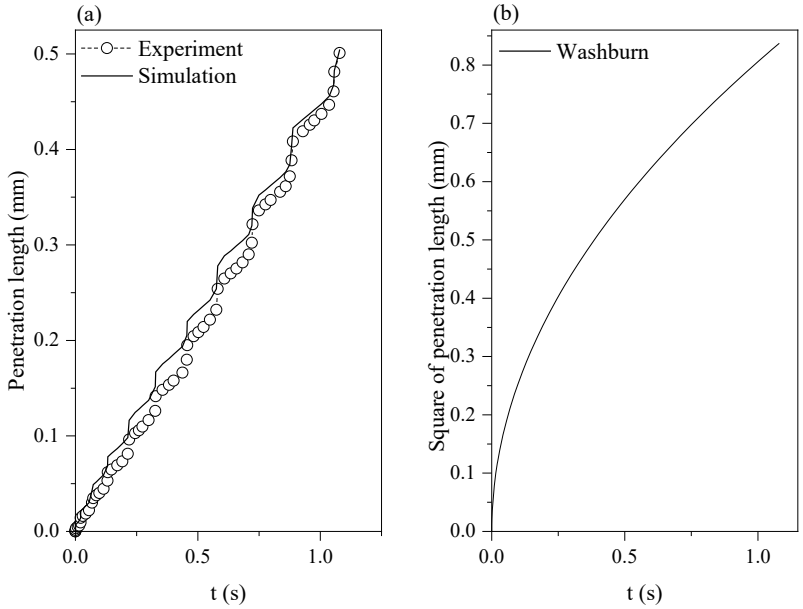

Figure 5.21. Penetration of liquid vs time in hydrophobic microchannel: (a) fluid moves faster through the constrictions for experimental and simulation data, (b) Washburn plot (l^2 vs t)

An average deviation of 11.7% was recorded between experimental and simulation results for hydrophilic microchannel and 9.2% was the deviation for hydrophobic microchannel. This deviation could be reduced by using real dynamic contact angle at each different triple point contact. In fact, periodically constricted structure leads to different dynamic contact angles compared with straight microchannel. Dynamic contact angle of fluid in straight microchannel was used for Washburn model (figure 5.20b and figure 5.21b) which a high curvature degree at the early stages was noticed. As Huffman [39] mentioned, this could be due to higher velocities at the beginning of the flow that comes with larger contact angles and higher capillary pressure reduction. Deviation of 29.5% and 23.4% between the experimental data and Washburn model, using constant apparent radius for hydrophilic and hydrophobic microchannels, shows that this model is not accurate enough for variable geometries and high viscosity liquids. However, numerical simulation was in good agreement upon the application of real radius for sinusoidal constricted capillary. Noteworthy to mention that resistance to capillary flow is related to the smallest radius but driving force of the capillary flow is proportional to the largest diameter. These two paradoxical phenomena result in slow rate of capillary flow in periodically constricted capillary microchannel [40].

In accordance to previous sections, flow of the liquid was faster in hydrophilic microchannel compared with hydrophobic microchannel as shown in figure 5.22. The first interface of the liquid in hydrophilic microchannel is at the constriction where higher velocity is recorded compared with the rest of the microchannel (figure 5.22a). However, the first capture of interface in hydrophobic microchannel is in bulge and velocity was increasing to reach the maximum at the constriction (figure 5.22b).

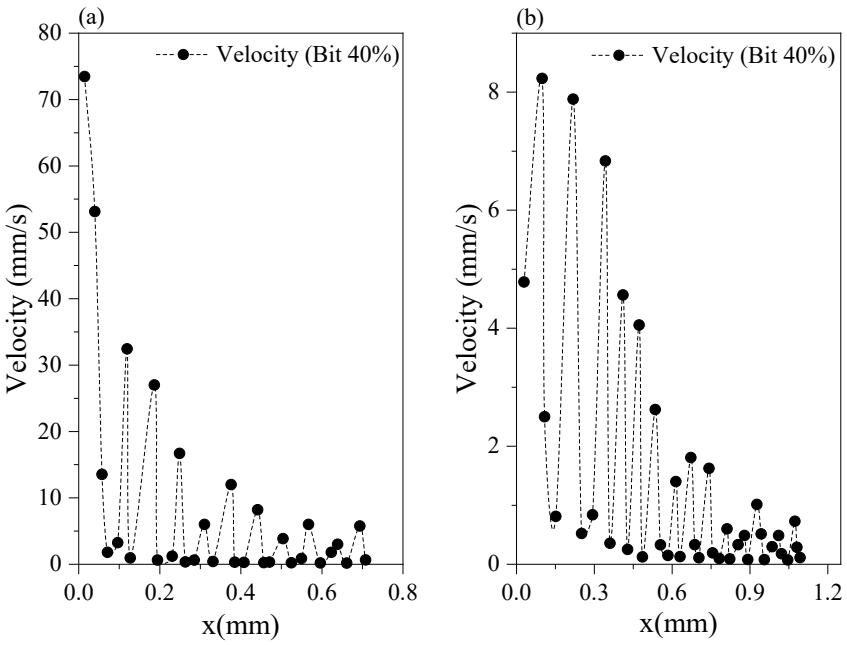

Figure 5.22. Velocity of the bitumen (40%) as a function of distance in (a) hydrophilic, (b) hydrophobic microchannel

5.5. Conclusion

This study carried out an experimental evaluation on the capillary-driven flow of the pure liquids and diluted bitumen in straight and periodically constricted glass based untreated, HMDS treated, and PFOCTS treated microchannels (10 μm depth and 40 μm width). For straight microchannels, the results show that square of interface position changes linearly with time. Interface images confirm that contact angle is almost constant during the pure liquids and diluted bitumen (i.e. 10% and 20%) flow in microchannel and a constant contact angle assumption is acceptable for this work. However, advancing contact angle is different compared with bulk static contact angle that is mostly applied in simulation and fluid flow calculations. This means that application of static contact angle causes larger deviation between experimental data and theoretical prediction. In addition, dynamic contact angle of higher concentration of bitumen

(40% and 60%) represents an increasing of contact angle during the penetration. Experimental results are in good agreement with theoretical Washburn model for untreated and HMDS treated microchannels. However, there was an increasing deviation between the experimental and model results for PFOCTS coated microchannel. In fact, diluted bitumen and pure liquids flow slower in PFOCTS treated microchannel that is related to very low surface energy of the treated surface. Capillary filling speed reduces during the fluid flow with a sharp reduction at the entrance of the microchannel.

Washburn model was not able to predict the experimental penetration of the liquids in sinusoidal capillary. Therefore, experimental data were simulated using Navier-Stokes equation that AARD was reduced from 29.5% for Washburn to 11.69%. It confirms that considering geometry on contact angle improves the simulation compared with a single contact angle in Washburn model. Capillary-driven flow of 40% diluted bitumen was stopped as expected for spontaneous flow in presence of external forces. Therefore, due to the importance of fluid flow in modeling of liquid penetration in porous media, energy analysis of the surface and liquid will be studied in the future work.

References

[1] S. Gupta, S. Gittins and P. Picherack, "Insights into some keyissues with solvent aided process," J. Can. Petrol. Technol., vol. 43, p. 54–61, 2003.

[2] B. Rostamin, S. R. Etminan, A. Soleimani and R. Kharrat, "Effect of Capillarity and Surface Tension on the performance of VAPEX Process," Canadian International Petroleum Conference, 2007.

[3] J. N. kuo and Y. K. Lin, "Capillary-Driven Dynamics of Water in Hydrophilic Microscope Coverslip Nanochannels," Japanese Journal of Applied Physics, p. 51, 2012.

[4] D. Sinton, "Energy: the microfluidic frontier," Lab Chip, pp. 3127-3134, 2014.

[5] J. C. Mcdonal, D. C. Duffy, J. R. Anderson, D. T. Chiu, H. Wu, O. J. Shueller and G. M. Whitesides, "Fabrication of microfluidic systems in poly(dimethylsiloxane)," Electrophoresis, vol. 21, no. 1, pp. 27-40, 2000.

[6] D. N. Breslauer, P. J. Lee and L. P. Lee, "Microfluidics-based systems biology," Mol. Biosys, vol. 2, p. 97–112, 2006.

[7] R. Sharma and D. S. Ross, "Kinetics of Liquid Penetration into Periodically Constricted Capillaries," J. CHEM. SOC., vol. 87, no. 4, pp. 619-624, 1991.

[8] J. Berthier, D. Gosselin, A. Pham, F. Boizot, G. Delapierre, N. Belgacem, D. Chaussy, “Spontaneous capillary flows in piecewise varying cross section microchannels” Sensor Actuat B-Chem, 223, 868-877, 2016.

[9] j. Bauer, G. Drescher and M. Illig, "Surface tension, adhesion and wetting of materials for photolithographic process," J. Vac. Sci. Technol., B, Microelectron. Nanometer Struct. Process. Meas. Phenom, vol. 14, no. 4, p. 2485, 1996.

[10] W. G. Anderson, "The Effects of Wettability on the Electrical Properties of Porous Media," Journal of Petroleum Technology, vol. 38, p. 1371–1378, 1986.

[11] V. Dwarakanath, R. E. Jackson and G. A. Pope, "Influence of wettability on the recovery of NAPLs from alluvium," Environ. Sci. Technol., vol. 36, no. 2, p. 227–231, 2002.

[12] S. M. Benson and D. R. Cole, "sequestration in deep sedimentary formations," Elements, vol. 4, p. 325–331, 2008.

[13] Abdallah, W., et al, "The fundamentals of wettability," Oilfield Rev., vol. 19, pp. 44-63, 2007.

[14] K. L. Mittal, "The Role of Polarity in the Structure of Silanes Employed in Surface Modification," in Silanes and Other Coupling Agents, CRC Press, pp. 51-64, 2009.

[15] K. Keshmiri, S. Mozaffari, P. Tchoukov, H. Huang and N. Nazemifard, "Using Microfluidic Device to Study Rheological Properties of Heavy Oil," in American Institute of Chemical Engineering (AIChE), San Francisco, 2016.

[16] G. Hu, D. Li, “Multiscale phenomena in microfluidics and nanofluidics” Chem. Eng. Sci., 62 (13), 3443-3454, 2007.

[17] L. J. Yang, T. J. Yao and Y. C. Tai, "The marching velocity of the capillary meniscus in a microchannel," J. Micromech. Microeng., vol. 14, p. 220–225, 2004.

[18] S. V. Garimella and C. B. Sobhan, "Transport in microchannels – A critical review," Annu. Rev. Heat Transfer, vol. 13, p. 1–50, 2003.

[19] E. W. Washburn, "The Dynamics of Capillary Flow," Physical Review, vol. 17, p. 273, 1921.

[20] R. Chebbi, "Electroosmotic-capillary penetration in circular microchannels," Journal of Colloid and Interface Science, vol. 361, pp. 639-642, 2011.

[21] N. R. Tas, J. Haneveld, H. V. Jansen, M. Elwenspoek and A. van den Berg, "Capillary filling speed of water in nanochannels," Appl Phys Lett, pp. 3274-3276, 2004.

[22] S. Mozaffari, P. Tchoukov, A. Mozaffari, J. A. J. Czarnecki and N. Nazemifard, "Capillary driven flow in nanochannels – Application to heavy oil rheology studies," Colloids and Surfaces A: Physicochem. Eng. Aspects, p. In Press, 2016.

[23] J. Kuo and W. Wang, "Capillary Filling Speed of Ferrofluid in Hydrophilic Microscope Slide Nanochannels," Microfluidic Nanofluidic, vol. 18, pp. 57-64, 2015.

[24] A. Saha, S. K. Mitra, M. Tweedie, S. Roy and J. McLaughlin, "Experimental and numerical investigation of capillary flow in SU8 and PDMS microchannels with integrated pillars," Microfluidic Nanofluidic, vol. 7, pp. 451-465, 2009.

[25] S. Levine, J. Lowndes and R. Reed, ""Two-Phase Fluid Flow and Hysteresis in a Periodic Capillary Tube," J. Colloid Interface Sci., 77, 253-263, 1980.

[26] A.F. Stalder, G. Kulik, D. Sage, L. Barbieri, and P. Hoffmann, "A Snake-based approach to accurate determination of both contact points and contact angles", Colloids Surf. A, 286, 92-103, 2006.

[27] P. G. de Gennes, "Wetting: statics and dynamics," Reviews of Modern Physics , vol. 57, no. 3, 1985.

[28] D. Burgreen and F. R. Nakache, "Electrokinetic Flow in Ultrafine Capillary Slits," The Journal of Physical Chemistry , vol. 68, no. 5, 1964.

[29] J. C. T. Eijkel, J. Bomer, N. R. Tas and A. van den Berg, "1-D nanochannels fabricated in polyimide," Lab Chip, vol. 4, pp. 161-3, 2004.

[30] W. P. Hardy, "The spreading of fluids on glass," Philos. Mag., pp. 38-49, 1919.

[31] M. Ledyastuti, Y. Liang, M. Kunieda and T. Matsuoka, "Asymmetric orientation of toluene molecules at oil-silica interfaces," The Journal of Chemical Physics, vol. 137, 2012.

[32] K. M. Davisa, A. Agarwala, M. Tomozawa and K. Hiraob, "Quantitative infrared spectroscopic measurement of hydroxyl concentrations in silica glass," Journal of Non-Crystalline Solids, vol. 203, pp. 27-36, 1996.

[33] S. Knaust, M. Andersson, K. Hjort and L. Klintberg, "Influence of surface modifications and channel structure for microflows of supercritical carbon dioxide and water," The Journal of Supercritical Fluids, vol. 107, pp. 649-656, 2016.

[34] J. V. Alsten, and S. Granick,, "Shear rheology in a confined geometry: polysiloxane melts," Macromolecules, vol. 23, pp. 4856-4862, 1990.

[35] R. C. R. da Silva, R. S. Mohamed and A. C. Bannwart, "Wettability alteration of internal surfaces of pipelines for use in the transportation of heavy oil via core-flow," Journal of Petroleum Scienec and Engineerign , vol. 51, pp. 17-25, 2006.

[36] P. Fabbri, M. Messori, F. Pilati, R. Taurino, C. Tonelli, M. Toselli, “Hydrophobic and oleophobic coatings based on perfluoropolyether/silica hybrids by the sol-gel method” Adv. Polym. Tech.,2007, 26 (3), 182-190.

[37] Y. F. Chen, F. G. Tseng, S. Y. C. Chien, M. H. Chen, R. J. Yu and C. C. Chieng, "Surface tension driven flow for open microchannels with different turning angles," Microfluidic Nanofluidic, vol. 5, no. 2, pp. 193-203, 2008.

[38] H. J. Barraza, S. Kunapuli and E. A. O’Rear, "Advancing Contact Angles of Newtonian Fluids During “High” Velocity, Transient, Capillary-Driven Flow in a Parallel Plate Geometry," J. Phys. Chem. B, vol. 106, pp. 4979-4987, 2002.

[39] R. L. Hoffman, "A study of the advancing interface," J Colloid Intertace Sci, vol. 50, p. 228, 1975.

[40] F. A. L. Dullirn, M. S. El-Sayed and V. K. Batra, “Rate of Capillary Rise in Porous Media with Nonuniform Pores,” J. Colloid Interface Sci., 1977, 60, 497.

Chapter 6: Asphaltene precipitation in Solvent-Based Bitumen Recovery

In addition to diluted bitumen capillary flow, asphaltene precipitation and deposition is the second result of solvent diffusion in bitumen. Although asphaltene deposition reduces the viscosity and improves the quality of bitumen, it can also block the pores and reduce the oil recovery. In fact, micro-scale study of asphaltene precipitation is critically important for potential application of solvent-based methods in future.

6.1. Introduction

Canada has the largest heavy oil and bitumen resources that is mostly available in Alberta and Saskatchewan. According to Canadian Association of Petroleum Producers, more than 80% of heavy oil and bitumen reservoirs exist in-situ where surface mining recovery method is not applicable. In fact, extremely high viscosity along with asphaltene content of heavy oil and bitumen makes the conventional oil recovery methods not applicable and alternate methods with the viscosity reduction are the main target of in-situ recovery techniques. Thermal recovery methods such as SAGD are currently being used commercially in the fields where viscosity can dramatically reduce by taking advantage of hot steam. However, thermal methods are energy intensive with serious environmental issues and require high volume of water. Considering the drawbacks, solvent-based methods such as enhanced solvent extraction (N-Solv^{TM}) seems superior to thermal methods.

A Version of this chapter is submitted to the Fuel journal and is under review for publication

Solvent-based extraction methods have higher energy efficiency, lower environmental challenges and in-situ upgrading. Lu and Gu [1] reported up to twenty orders of magnitude heavy oil viscosity reduction by reducing the asphaltene content from 16% to zero using n-pentane as precipitant. Deasphalting may cause undesired effects due to asphaltene flocculation and precipitation like pore-throat plugging, permeability and oil production reduction [2, 3]. Asphaltene is the dark brown to black friable non-volatile end of the crude oil [4, 5]. Asphaltenes are mainly defined as the soluble fraction of bitumen in aromatics such as toluene and insoluble in n-alkanes (e.g. n-pentane) [6, 7]. The molecular weight of asphaltenes differs as much as a factor of 10 depending on the measurement method. Vapor pressure osmometry produced molecular weight of 4000 gr/mol while field ionization mass spectroscopy estimated the molecular weight of 700 gr/mol. The large difference confirms the effect of particle aggregation on molecular weight. Asphaltene contains 2-6 polynuclear aromatics, small amount of sulfur, nitrogen, oxygen and trace amount of the nickel and vanadium [8]. The aromatic is surrounded by alkyl chains of average length of 6 carbon atoms [9]. “Archipelago” model has been proposed to describe the dominant molecular structures of asphaltenes that aromatic islands linked together by aliphatic chains [10].

Asphaltenes are complex with variable structure including polar functionalities which structural properties lead to irreversible aggregation of asphaltene particles. They have soluble and insoluble fractions that modification in fundamental groups alter their solubility and precipitation may occur [11]. Effective parameters on asphaltene precipitation are temperature, pressure, and adjustment of reservoir oil composition with solvent or CO_2 injection. Asphaltene molecules tend to form nanoaggregates based on aromatic interaction between asphaltene aromatic cores. Size and shape of nanoaggregates is affected by aliphatic chains due to steric

repulsion [12]. In colloidal point of view, resins are considered as stabilizer agents that adsorb on the surface of asphaltene and act as a steric stabilizing layer [13]. In fact, solubilization of asphaltene with resins keeps the asphaltene molecules soluble in the bitumen and desorption of resins from asphaltene surface causes precipitation.

According to Small-Angle Neutron Scattering (SANS) [14] and molecular dynamic calculation [15], hydrogen, π-π, and van der Waals are the main interactions in association mechanism. Stachowiak et al. [8] introduced van der Waals interaction, "induced conformational changes", and molecular orientation between the chains of n-alkanes and asphaltenes as the main driving force for self assembling of asphaltenes. Hamaker constant shows the strength of van der Waals forces between asphaltene particles based on polar-polar (Kaesom force), nonpolar-polar (Debye force), and nonpolar-nonpolar (London dispersion force) interactions. Van der Waals forces are dominated by nonpolar-nonpolar interactions [13]. Addition of n-alkanes to the bitumen increases nonpolar-nonpolar interactions and the attractive interaction force between asphaltene particles. Moreover, addition of carbon number of n-alkane increases the polarity index of solvent and reduces nonpolar-nonpolar interaction and causes less precipitation. For instance, pentane precipitates less polar with lower molecular weight asphaltenes compared with decane with heavier and polar ones.

It is worth mentioning that asphaltene precipitation is the formation of asphaltene particle in crude oil. Precipitated particles aggregate and form larger particles (i.e. flocs) in flocculation process [16]. However, deposition is the settling process of flocs from solution phase to the rock surface [17]. In order to detect the asphaltene and its related damages, it is critically important to know the onset point of asphaltene precipitation that defined as the minimum amount of solvent to precipitate asphaltene out of the crude oil [18]. There are several methods to detect the onset

point of precipitation such as interfacial tension measurement [19], asphaltene and solvent solubility parameter difference [20], refractive index measurement, and capillary viscometer [21].

Asphaltene precipitation and deposition in macroscopic-scale has been extensively studied [22-24]. Rassamdana et al [25] measured asphaltene precipitation using n-alkanes with carbon number between 5 to 10 at various pressure and temperatures. It was found that precipitated asphaltene was decreasing as carbon number of n-alkane was increasing and there was a certain solvent to oil ratio (i.e. onset point) to start the precipitation. Buenrostro-Gonzalez et al. [26] reported P-T diagram (i.e. asphaltene precipitation envelope) of oil samples as well as a series of titration experiments to determine the precipitation onset composition. In addition to the experiments, the asphaltene deposition has been modeled using different theories and assumptions. Soulgani et al [27] modeled the asphaltene deposition by introducing a new surface deposition term to asphaltene deposition model in porous media previously introduced by Wang and Civan [28]. Taherpour et al. investigated a novel Fuzzy C-Means algorithm to predict deposited asphaltene as a function of dilution ratio, carbon number of solvent, and temperature [29]. Mohebbinia et al. [30] used thermodynamic model in a compositional reservoir simulator to model the asphaltene precipitation. Although macroscopic effects of asphaltene precipitation are widely studied, pore-throat clogging and precipitation patterns in pore-scale has not monitored and studied thoroughly.

Microfluidic platform, as the science that handles extremely tiny amount of fluids, is recently applied in heavy oil and bitumen extraction. They mimic the porous structure at reservoir condition with direct visualization of pore-scale phenomena. Chatsiz [31] studied pore-scale events of mass transfer during the VAPEX process using glass etched micromodels. He observed

a hierarchical manner of diluted bitumen drainage displacement mechanism and interplay of gravity and capillary forces. Farzaneh et al. [32] investigated oil recovery during solvent based injection methods using five-spot glass microchannels with rock look-alike and network-pattern structures. Pore-scale phenomena such as viscous fingering, solvent diffusion in heavy oil, and entrapment of solvent and oil were also studied. In our previous work [33], capillary flow of pure liquids and diluted bitumen were studied in hydrophilic and hydrophobic straight and constricted microchannels. During the liquid penetration, dynamic contact angles were measured using image processing techniques and experimental liquid penetration data were compared with theoretical models.

Microfluidic apparatus is recently used for measurement of asphaltene properties, onset of asphaltene precipitation as well as deposition [6, 34-37]. Micromodel has a pore and pore-throat size close to the size of real oil sand porous media and is a suitable mimic of the real asphaltene deposition. Sieben et al. [38] performed asphaltene yield measurements on crude oil and compared the microfluidic results with available methods. They determined the asphaltene content of the oil sample based on absorbance values of maltene and the crude sample with substantial reduction in time and consumables compared with conventional methods. Hu et al. [39] represented asphaltene deposition in a transparent packed-bed microreactor, bridging macromolecular science with microsystems. They revealed that lower Reynolds number led to higher asphaltene deposition, porosity loss, and permeability reduction. More recently, Lin et al. [34] studied dynamic of asphaltene deposition in porous media using microfluidic device. They have also measured the precipitation onset point using indirect method described by Tavakoli et al. [18]. A synthetic oil and n-heptane flowed through the chip and deposition was analyzed as a function of solubility that is related to particle size and Peclet number. Pore scale velocity profile

and shear rate study showed deposits tendency to grow against the flow direction at low shear zones. Daryani et al. [6] described the onset of asphaltene precipitation in a uniformly patterned micromodel and recognized a critical number of diffused molecules to start the precipitation. They also studied the effect of aromatic to paraffinic ratio on the acceleration of precipitation process.

Surface modification has been applied in various processes such as biomedical [40], oil recovery [41], and geological carbon sequestration [42]. Surface modification alter the wettability based on the type of application. For example, wettability is an important parameter on capillary flow and displacement process in porous media to enhance the secondary oil recovery [43]. The reservoirs are usually intermediate-wet due to the variation of mineral types. Attempts to generalize the wettability concept of reservoirs have been unsuccessful so far. Organosilane compounds can improve the oil recovery by altering surface energy and wettability from water-wet to oil-wet [44]. Important parameters on formation of hydrophobic surface are extend of surface coverage, residual unreacted groups, and silane distribution [45]. Alboudwarej et al. [46] studied asphaltene adsorption on metal surfaces and reported to be dependent on the source of asphaltene. Dean and McAtee [47] concluded asphaltene adsorption depends more on the surface properties such as wettability and roughness. Zahabi and Gray [48] reported that the amount of deposited asphaltene on hydrophilic and hydrophobic micromodels was almost identical.

In this study, dynamic of asphaltene deposition was visualized using pure n-alkanes precipitants in untreated (hydrophilic) and Trichloro(1H,1H,2H,2H-perfluorooctyl)silane (PFOCTS) treated 2D micromodels and damaged area was quantitatively evaluated by optical microscopy. In addition, the asphaltene precipitation point was detected and its concentration

was calculated using image processing technique in less than 30 minutes and 20 μL of solvent. Moreover, precipitated asphaltene was characterized using Helium Ion Microscopy (HIM). TIRF microscope tomography was also applied to reveal asphaltene morphology and Axial Super-Resolution Evanescent-wave Tomography (AxSET) technique, developed in our group [49], was used to get 3D reconstruction of asphaltene particles.

6.2. Materials and Methods

6.2.1. Materials

Athabasca bitumen was provided by InnoTech Alberta. n-Pentane and n-decane (HPLC grade, Fisher Scientific) was used for asphaltene deposition experiments. PFOCTS was purchased from Sigma-Aldrich for surface treatment purpose. The bitumen molecular weight, density, and viscosity at room temperature (i.e. 22 ºC) were 601.4 g/mol, 1.012 g/cm^3, and 5.2×10^5 cP, respectively. The asphaltene content of the bitumen was measured using American Society of Testing Materials (ASTM) D2007-80 standard for n-pentane and n-decane. The bitumen was added to 40-fold excess of solvent and mixture was shaken thoroughly and left to equilibrate for 1 day. Asphaltene was separated using a filter paper (0.22 μ) inside a funnel cup connected to the glass flask. When vacuum pump was connected to the flask, filter was washed with precipitant to remove maltenes that may adsorb on the asphaltene. The solvent was removed and asphaltene was stored in a glass vial. Asphaltene precipitated with n-pentane and n-decane was 20% and 12%.

6.2.2. Micromodel fabrication

A homogeneous two-dimensional porous network of circular posts (d_p=100 μm) with pore body width of 100 (±1) μm, pore throat width of 40 (±1) μm, and depth of 15 (±1) μm was etched into glass to study asphaltene precipitation and deposition. There were two patterns of posts with zero and 45-degree to evaluate the hydrodynamic of asphaltene deposition. Although a rock look-alike pattern is a better representative of real unconsolidated oil sands, uniform structure micromodel eliminates the effect of parameters such as various pore geometry, roughness, tortuosity, and variable pore to pore-throat aspect ratios. Porosity is defined as pore volume to total volume of the model. The total volume was calculated knowing the depth, width and length of the micromodel. The pore volume was found from the difference in mass of the model when saturated with water and dried which was around 3μL. The porosity of the zero degree and 45-degree micromodels was around 38% and 42%, respectively. Micromodels were fabricated on 4 inches by 4 inches borofloat glass wafers following the standard photolithography method. A layer of Cr (40 nm) and Au (120 nm) were coated on cleaned wafers then photoresist (HPR 504) was spun onto the wafers. They were exposed to light through a photomask transferring the designed pattern. After removing the Au and Cr, glass was etched with Hydrofluoric Acid (HF). An unpatterned wafer with inlet and outlet holes were pressed to patterned wafer and placed in muffle furnace (650°C) for two hours for permanent glass bonding.

6.2.3. Surface modification and asphaltene characterization

Wettability of the micromodels were altered with a siliconizing fluid. 1 mM solution of silane precursor in toluene was injected in micromodel for 15 minutes to coat the glass microchannel by reacting with silanol groups (Si-OH) on the glass surface. Micromodels were washed with toluene, deionized water, and ethanol and dried in stream of nitrogen. As shown in figure 6.1, Water contact angle on untreated (a) and treated (b) glass wafer was around 12°, and 118°, respectively.

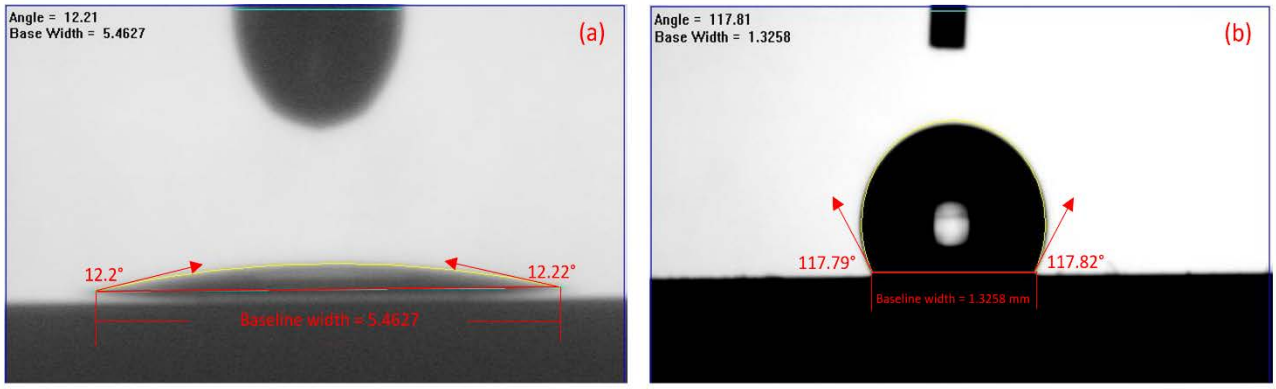

Figure 6.1. Water contact angle on (a) untreated and (b) silane-treated glass wafers.

Fluorescence imaging allows molecules beyond the resolution limit of the light microscope to be visualized. Due to fluorescence nature of asphaltene [50] over a range of emission spectrum, detection of asphaltene can be achieved with techniques involving fluorescence. In TIRF microscopy, a sample is illuminated with evanescent wave generated by total internal reflection at the interface of coverslip and the sample [51]. By changing the incident angle of the excitation laser, the penetration depth of the evanescent wave can be controlled [52]. The illumination profile of the evanescent wave is given by $e^{-\alpha z}$, where α is the attenuation coefficient

of the wave, and the illumination depth is given by $dz = 1/\alpha = \lambda/(2\pi\sqrt{n_c^2 \sin\theta - n_s^2})$, where λ is the wavelength of excitation laser, θ is the incident angle, n_c and n_s are the refractive indexes of the coverslip and the sample [52].

TIRF (Nikon eclipse Ti) microscope equipped with 488 nm laser (Melles Griot) for excitation and 500-550 nm emission filter was used to capture near-surface 2D images. However, the capability of TIRF was improved to acquire high signal-to-noise ratio 3D tomographic images thorough capturing multiple z-stack images [49]. 3D reconstruction is a fast and inexpensive method of particle characterization compared with Scanning Electron Microscope (SEM) or HIM. In addition, HIM and SEM are expensive with potential artifacts due to sample preparation. Also working under vacuum and low temperature may change the sample [53]. Precipitated asphaltene was evaluated using a glass slide with a 10 mm diameter circular aperture drilled in its center. Asphaltene samples were placed in the well that was already glued to a glass coverslip and then sealed on the top with another coverslip to prevent drying or contamination. Noteworthy to mention that for total internal reflection, the refractive index of the sample should be less than that of glass coverslip (1.55). Therefore, water with refractive index of 1.33 was added to the sample and noticed that refractive index is close to that of water.

6.2.4. Experimental Setup

As mentioned earlier, two patterns of zero and 45-degree micromodels were used in this work (figure 6.2a and 6.2b). According to figure 6.2c, the first step was injection of bitumen in micromodel. Experiments were carried out at atmospheric pressure and room temperature (i.e. 23°C) but high viscosity of the bitumen requires high pressure and temperature to inject the

sample into the model. Therefore, a micro-volume glass syringe (Hamilton, Nevada, USA) was half filled with bitumen and placed in oven (80 °C). When acclimatised, the syringe was placed in syringe pump (KDS 200, Holliston, USA) and connected to the microchannel inlet using nanoport connections (IDEX, nanoport assemblies, PEEK 1/16 in). After saturation of half of the micromodel with bitumen, solvent was injected in a constant rate of 10 µL/min (figure 6.2d) and bitumen-solvent diffusion was monitored via white light microscope coupled with a high-speed digital charged coupled device (CCD) camera and images were stored in a computer for further analysis. In order to evaluate the detection point of precipitation, light disturbance is extremely important so the setup was placed in a constant source of light to avoid external light source disturbance. There was a curvature at the solvent-bitumen interface that could deviate the diffusion coefficient measurement from one-dimension assumption but in this work, we are looking for asphaltene precipitation that is after the initial diffusion of solvent and bitumen.

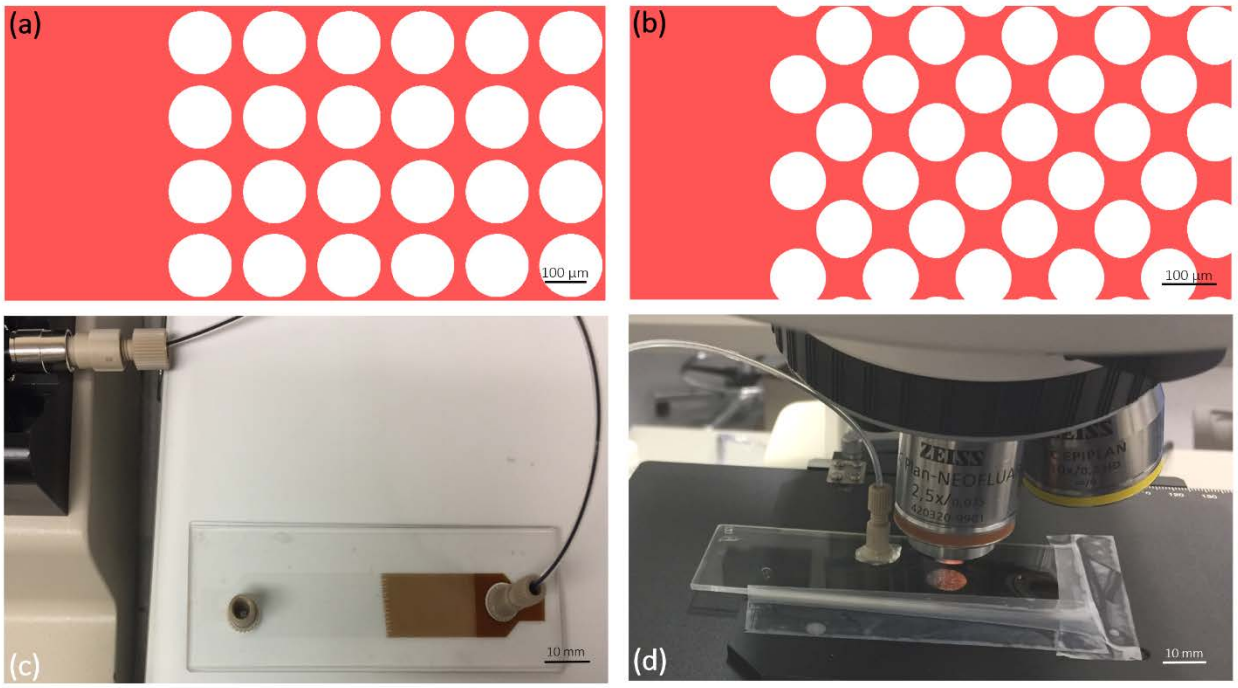

Figure 6.2. (a) Design of porous media parallel posts. (b) Design of porous media 45-degree posts. (c) Injection of bitumen in microchannel. (d) Experimental setup.

6.3. Results and Discussions

6.3.1. Detection of Asphaltene Precipitation

To determine the detection point of asphaltene precipitation, light intensity of the recorded images should convert to solvent concentration. The absorbance of light is related to the number of molecules present in the solution (concentration of solution). As shown in Eq. 4-1, the Beer-Lambert law relates the attenuation of light to the absorbing media which light is passing through [54]. Prior to the experiments, pure solvent and bitumen were separately injected into the micromodel and light transmission intensities were recorded. Light intensity profiles during the solvent-bitumen diffusion as a function of time was recorded in a fixed region of interest. Solvent-bitumen interface in 2D micromodel at t=0 is shown in figure 6.3a. The left side of the interface with darker color and lower transmitted light is the bitumen and the right side with higher transmitted light is the solvent side. As represented in figure 6.3b, concentration gradient across the region of interest (red) is extremely small compared with axial direction. Therefore, an average intensity value at each elevation was calculated (figure 6.3c).

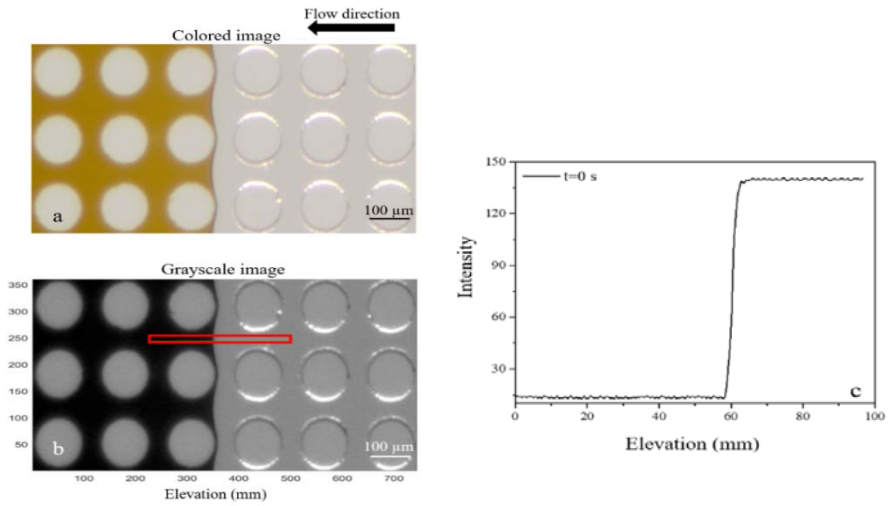

Figure 6.3. Bitumen-solvent interface in 2D miscromodel (a and b). Bitumen-solvent intensities at the interface at t=0 (c). Left side in bitumen and right side is solvent.

Eq. 4-2 was used for local densities and mass fraction of the solvent was calculated based on Eq. 4-3. In addition to Eq. 4-3, a calibration curve was also considered according to Fadaei et al. [46] work. They measured light transmission intensity of each calibration samples with known toluene mass fraction (0.0-1.0) in a T-shaped microchannel and calibration curves were used to convert the light intensity of experiments to solvent mass fraction. However, there was an intensity reduction due to asphaltene aggregation and precipitation at the critical solvent-to-bitumen (S:B) ratio [55] in our work and calibration curve was not able to follow the expected intensities after the detection of precipitation. It was realized that asphaltene precipitation occurred when solvent diffused into the oil and its concentration reached to a critical point. Diffusion of n-pentane into bitumen changed the color of oil from dark brown to lighter color while precipitated asphaltene remained in dark color.

As shown in figure 6.4a, at the beginning of the experiment, sample was uniform with no particles of asphaltene. Around 20 s, some haze that are sub-micrometer particles were precipitated (figure 6.4b). Particles were observed in about 45 s with high potential of flocculation and aggregation (figure 6.4c). Larger sizes of asphaltene particles were detected after 60 s at the same location (figure 6.4d). It is worth mentioning that detection of particles is limited to the resolution of optical microscope. Time-lapsed images of n-pentane-bitumen diffusion (figure 6.5) represent the detection point of asphaltene particles. Asphaltene particles were not detected in lower concentrations of solvent at bitumen-rich side (left side) for the reported times. Precipitation onset time is very sensitive to solvent concentration and varies between a few seconds and several months [56]. However, asphaltene particles were detected between solvent concentrations around 70% to 85% (right side). For concentrations over 85%,

particles of asphaltene were sub-micrometer and not enough to detect with our optical microscope.

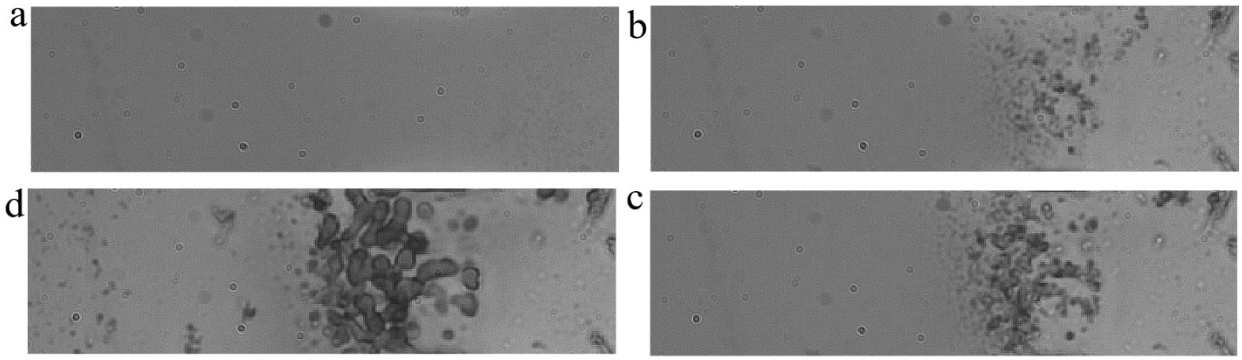

Figure 6.4. Micrographs of asphaltene precipitation at t=0s (a), t=20s (b), t=45s (c), and t=60s.

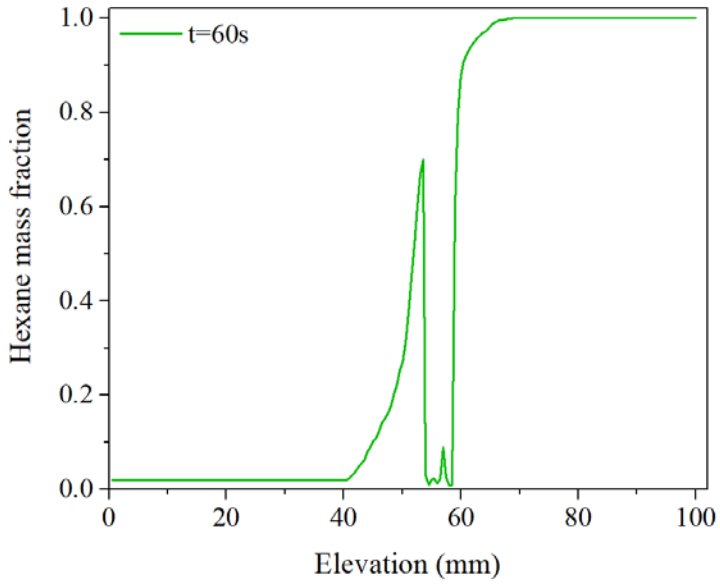

Figure 6.5. Detection point of asphaltene precipitation during the n-pentane-bitumen mutual diffusion.

6.3.2. Characterization of bitumen and asphaltene

Viscosity of the original and deasphalted bitumen was measured using rheometer (Rheolab QC, Anton Paar, Austria). As shown in figure 6.6, viscosity of deasphalted bitumen from n-

pentane is much lower than deasphalted bitumen from n-decane. In fact, n-pentane precipitated higher amount of asphaltene (i.e. 20%) and lower viscosity compared with n-decane (i.e. 12%). The high level of asphaltene precipitation can increase pore throat blockage, clogging and oil recovery reduction during the time.

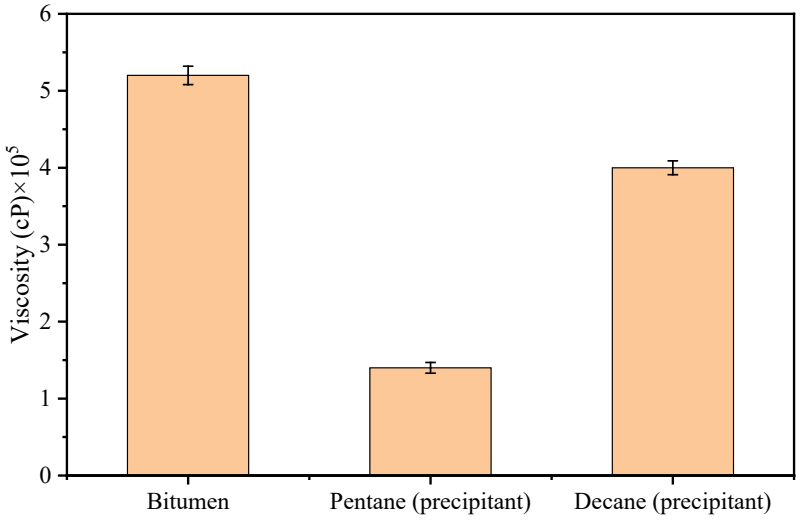

Figure 6.6. Viscosity of original bitumen, deasphalted bitumen with n-pentane and n-decane as precipitant.

HIM images of deposited asphaltene from n-pentane (figure 6.7a) and n-decane (figure 6.7c) are represented. Each solvent produced different asphaltene morphology due to the resins and low molecular weight asphaltene components. Higher flocculation, agglomeration, and deposition in a shorter time of precipitation and deposition were noticed with n-pentane compared with n-decane. As shown in figure 6.7b, n-pentane produced asphaltene with more resins and light components attached to it with amorphous and porous structure that cause polar functional groups cage within the aggregates structure [36, 57]. However, n-decane, with larger number of carbons, precipitated asphaltene with smoothed surface and rigid structure (figure 6.7d). In agreement with other study [57] lighter solvent produced smaller particle sizes with higher cluster formation. TIRF microscope as a potential alternative was used to capture

fluorescence image (figure 6.8). TIRF microscope is mostly utilized to capture 2D images of a sample, we extend the capability of TIRF and use it to acquire 3D tomographic images of precipitated asphaltenes using n-pentane and n-decane by acquiring multiple z-stack images [52].

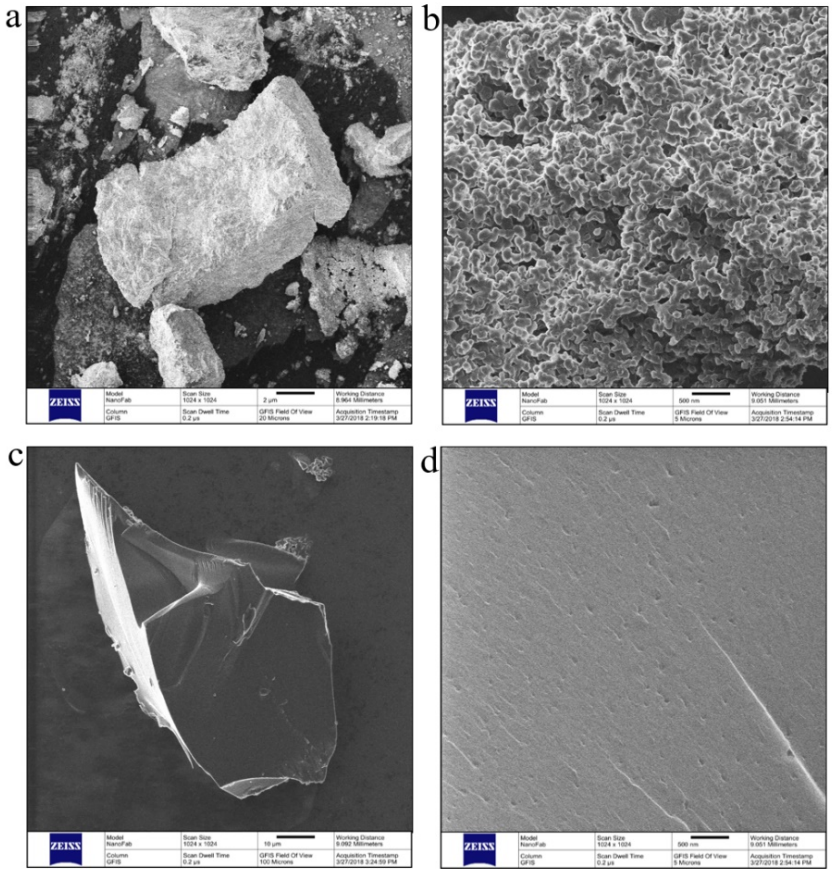

Figure 6.7. Microscopic structure of precipitated asphaltene from n-pentane (a and b) and n-decane (c and d) under the HIM at 1000× (a), 2000× (b) and (d), and 500× (c) magnification.

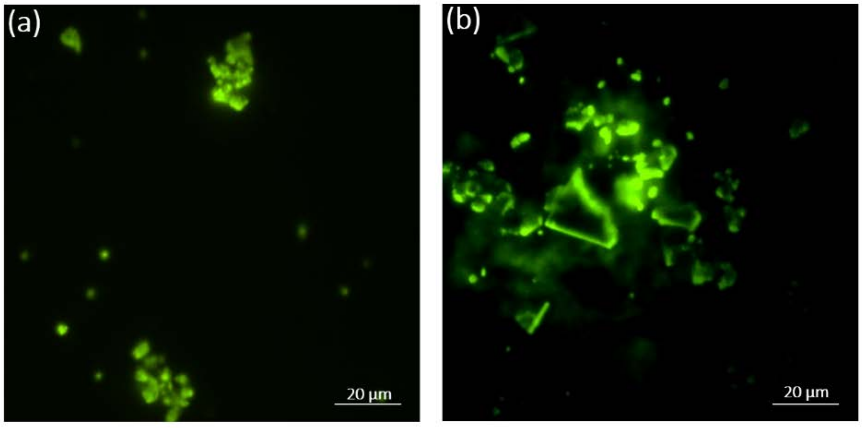

Figure 6.8. TIRF images of precipitated asphlatene from (a) n-pentane and (b) n-decane for an excitation laser of 488 nm and emission filter of 500-550 nm.

As shown in figure 6.9a and 6.10a, three dimensional images of asphaltene samples were acquired by z-stacking multiple focal-plane optical sections. Bright spots show fluorescence from asphaltene visualized using hot colormap. Fig 6.9b and 6.10b show the focal-plane and axial-plain cross-sectional view over selected region of interest of n-pentane and n-decane precipitated asphaltene respectively. 3D tomographic reconstructions of individual particles were created by thresholding and segmenting the image over selected region of interest (figure 6.9c and 6.10c) from three-dimensional image [49]. In agreement with HIM analysis, 3D reconstructed image of precipitated asphaltene from n-pentane was irregular in shape while n-decane produced larger particles with smoothed surface with rigid structure.

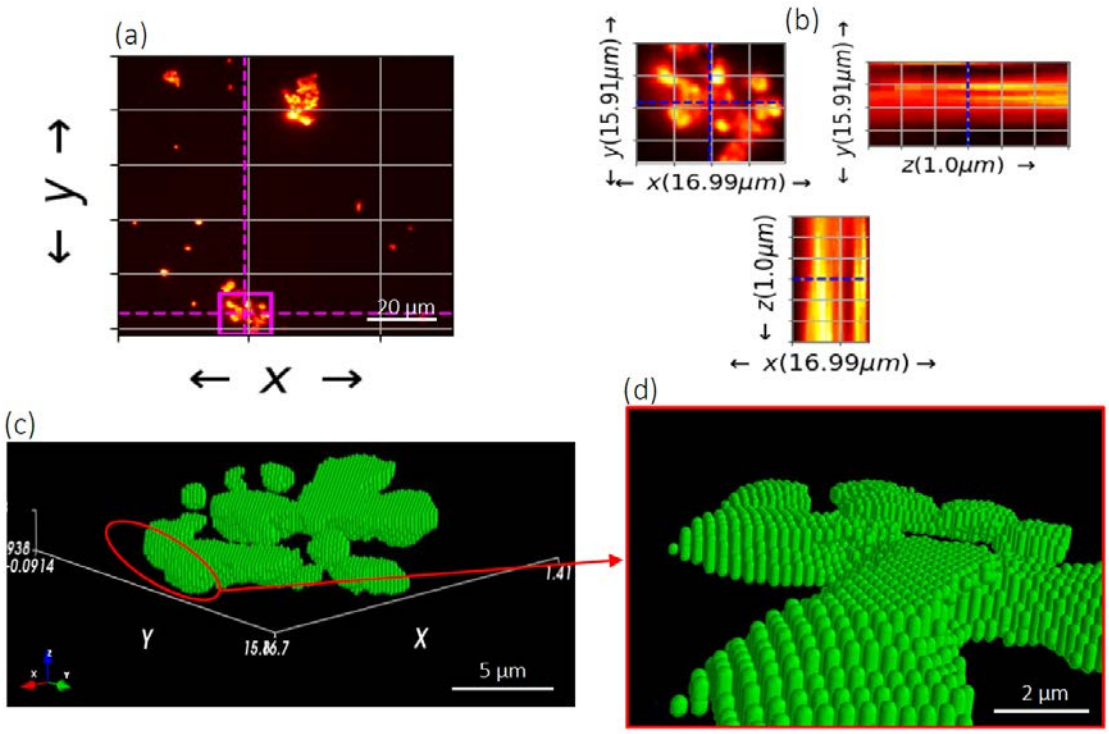

Figure 6.9. (a) optical section of the TIRF z-stack images for n-pentane precipitated asphaltene. (b) different cross sections over region of interest. (c) 3D reconstruction of the precipitate in image (b).

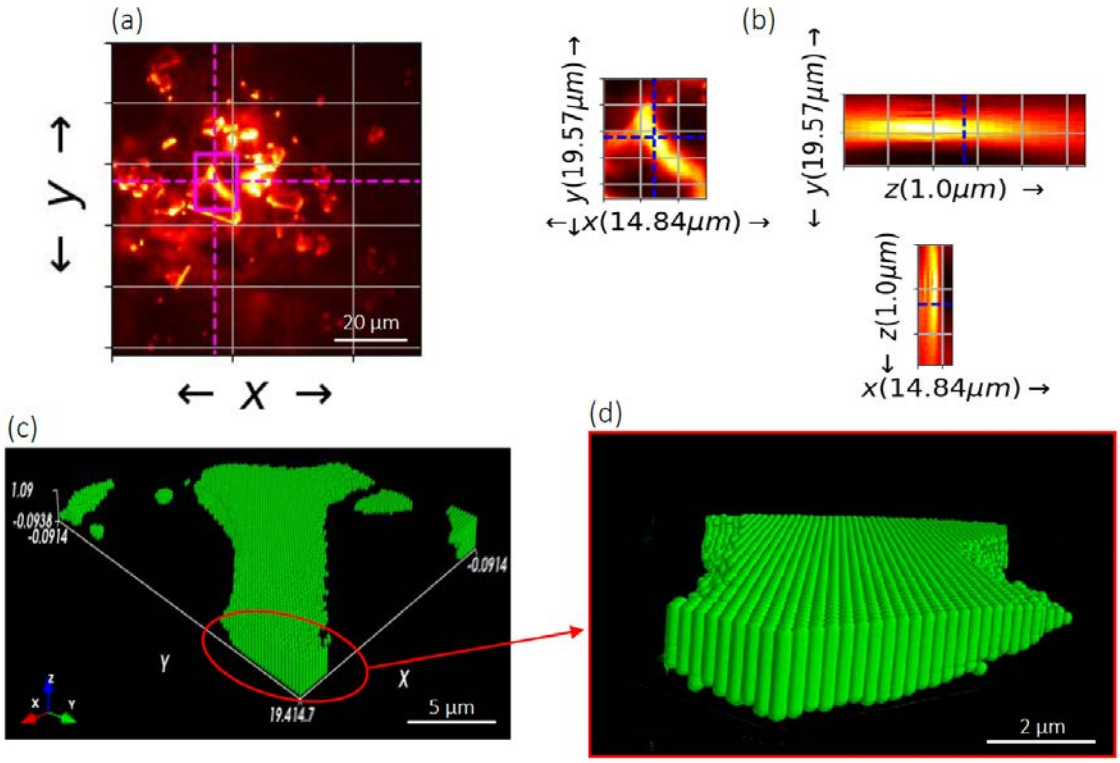

Figure 6.10. (a) optical section of the TIRF z-stack images for n-decane precipitated asphaltene. (b) different cross sections of region of interest. (c) 3D reconstruction of the precipitate in image (b).

6.3.3. Asphaltene Deposition

Figure 6.11 shows deposited asphaltene from n-pentane in zero and 45-degree patterns which black area is occupied by asphaltene. According to optical microscopy images, results of asphaltene deposition for both patterns of pillars were consistent and severe pore blockage and bridging between the posts were noticed in agreement with other studies [34, 36]. Hydrodynamic bridging was significantly occurred between the posts when significant amount of asphaltene was precipitated and deposited during the diffusion process. In fact, initial asphaltene deposition led to further deposition of asphaltene against the solvent direction and in the pore throat. High level of deposition caused permeability reduction and increases the pressure drop across the porous media, accordingly [34].

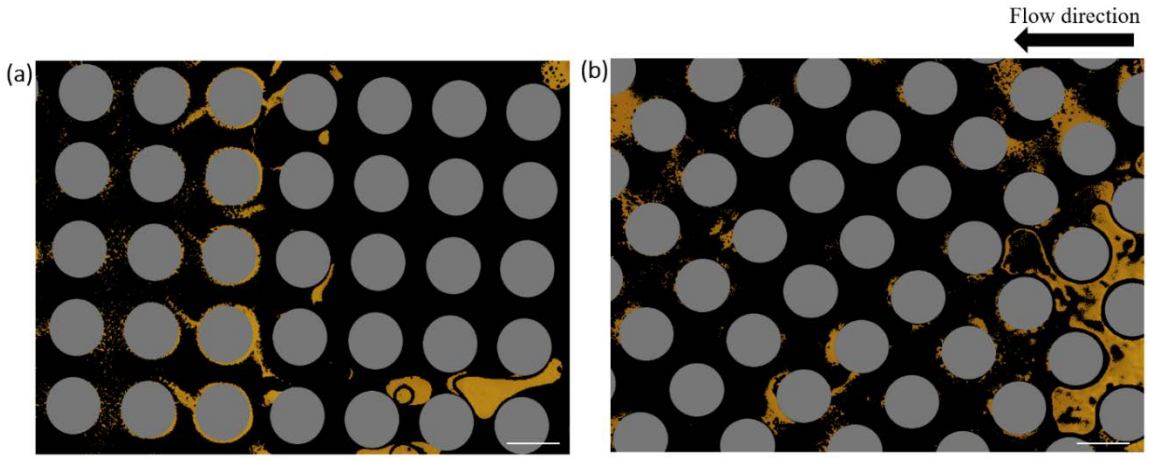

Figure 6.11. Original image of deposited asphaltene with n-pentane at (a) zero degree and (b) 45-degree micromodels. Black area is covered with bitumen and yellow sections are void spaces. White scale bar is 100 µm.

Figure 6.12 illustrates deposited asphaltene from n-pentane and n-decane in hydrophilic (figure 6.12 a and c) and hydrophobic (figure 6.12 b and d) micromodels which higher asphaltene precipitation was noticed in hydrophilic model. Asphaltene deposition around the posts was recognized with image thresholding which the black areas show precipitated asphaltene. Solvent flowed from right to left and precipitated sub-micrometer particles moved around the posts and clumped together and flocculation produced larger aggregates. Asphaltene growth at the pore throat led to blocking the flow path over the time. While n-pentane produced higher deposition and severe reservoir damage, n-decane had lower amount of asphaltene precipitation and deposition and higher oil recovery. In other words, lighter solvent has higher in-situ upgrading but less recovery. Hydrophilic micromodel had higher precipitation than hydrophobic porous media but they both exhibited the same deposition structure.

Driving force of primary asphaltene deposition is related to interaction of polar components of bitumen and silanol groups (Si-OH) of piranha cleaned micromodel [58]. In fact, active sites of silica are critically important for asphaltene adsorption and reduction of Si-OH groups

decreases the amount of deposition. Jouault et al. [59] studied adsorption of asphaltene on hydrophilic and hydrophobic silica powder. They revealed higher interaction potential between asphaleten and hydrophilic surface but similar mechanism of adsorption for both cases were monitored. In this study, slower asphaltene deposition was monitored in hydrophobic structure but asphaltene coagulation and agglomeration rate and bridging was similar. It seems that deposition is related to surface properties and asphaltene concentration of bitumen sample but precipitation of asphaltene is mostly related to bitumen chemical composition (i.e. polyaromatics and polycyclic ring containing nitrogen, oxygen and sulfur), resins concentration and characteristic size of asphaltene aggregates in bitumen.

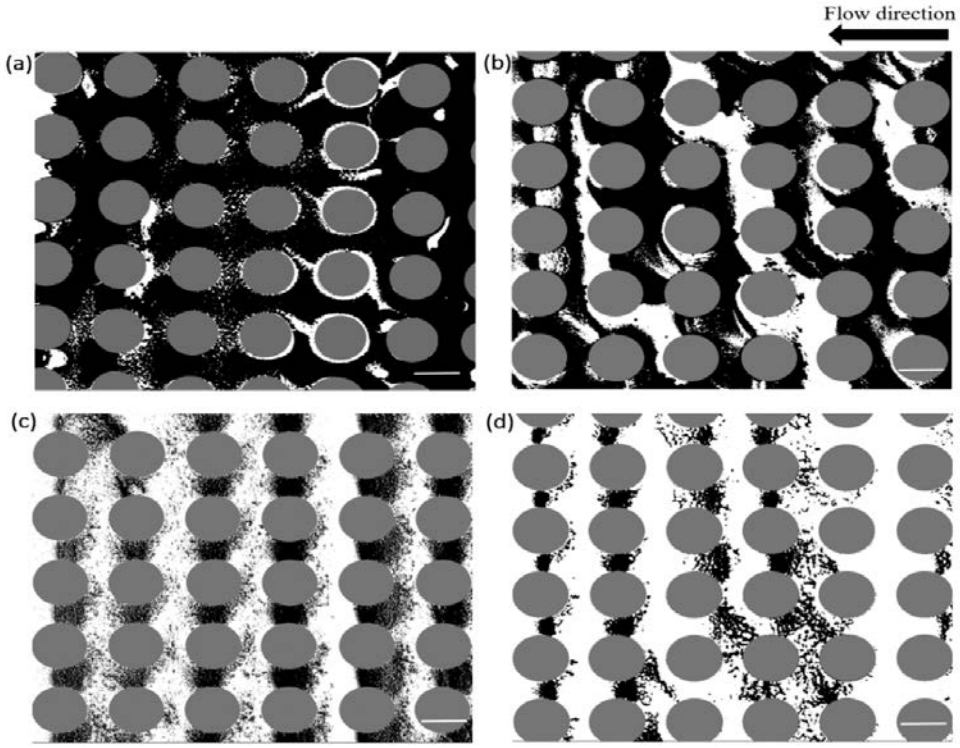

Figure 6.12. Deposited asphaltene in hydrophilic (a and c) and hydrophobic (b and d) micromodels for n-pentane (a and b) and n-decane (c and d). Black area is covered with bitumen and white area is void space. Scale bar is 100 µm.

Deposition of asphaltene was started around the pillars where there was a barrier towards the flow of diluted bitumen and precipitated asphaltene (figure 6.13a). The other precipitated

asphaltene particles attached to deposited layers causing flow path blockage and hydrodynamic bridging at pore throats (figure 6.13b). Dynamic of deposition growth, as a physical process, was very faster than precipitation, as a thermodynamic process [6]. This was confirmed with time-lapsed images of asphlatene deposition and growth presented in figure 6.13. Looking to the second column of pillars, there were no deposited particles at figure 6.13b. Dilution of bitumen and diffusion of solvent commenced deposition of asphaltene (figure 6.13c) and increased the clusters of asphaltene precipitates that attached together (figure 6.13d) and continued to the next column (figures 6.13e and 6.13f).

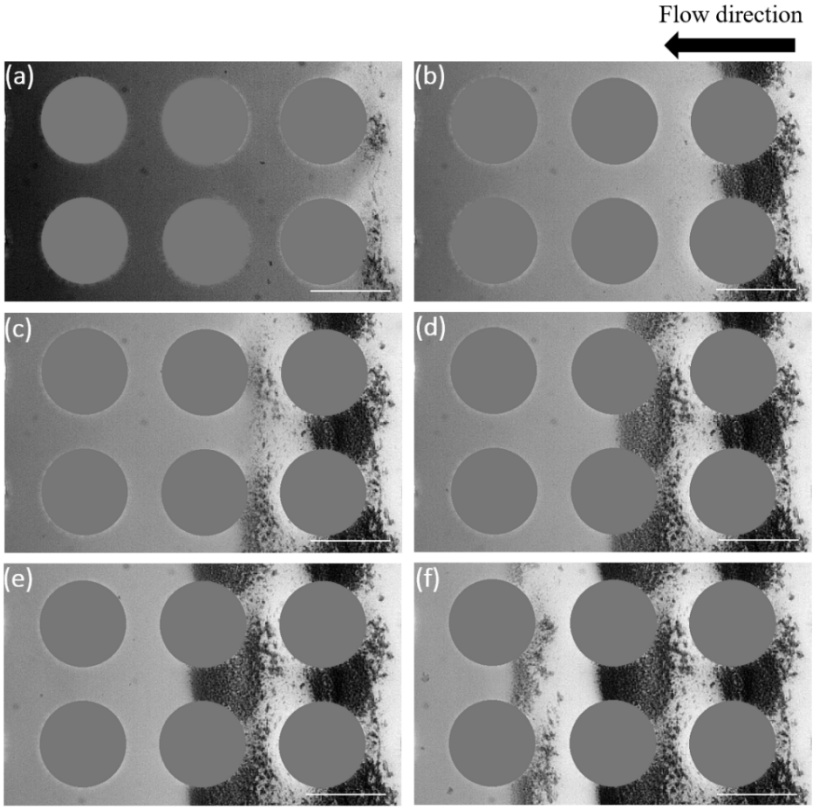

Figure 6.13. Aggregation and deposition of precipitated asphaltene from n-decane at (a) early stages of asphaltene deposition; (b) 20 s; (c) 30 s; (d) 45 s; (e) 60 s; and (f) 70 s. Solvent flow from right to left. Scale bar is 100 µm.

To quantify damaged area and pore blockage, experimental images of asphaltene deposition in porous media were analyzed using ImageJ®. Threshold segmentation were imposed on each

image and turned image into binary using Otsu's method and pixels of asphaltene deposition were counted. Pixels were then converted to area using a standard stage micrometer (10 µm per smallest division) and multiplied by depth of microchannel to calculate asphaltene deposition volume [26]. Damaged area was estimated based on deposited asphaltene versus porous area as shown in figure 6.14 for hydrophilic, zero-degree micromodel after equilibrium condition when no more changes was monitored in porous media. As represented in figure 6.12, n-pentane caused extreme damage to the reservoir and most of the pore throats and paths were blocked.

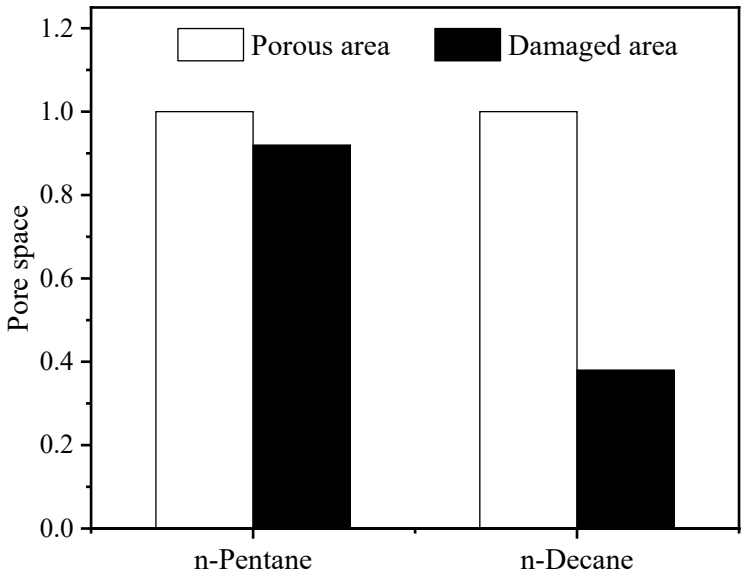

Figure 6.14. Total porous area (white) compared with damaged area (black) for n-pentane and n-decane in zero-degree pattern microchannel after equilibrium.

6.4. Conclusion

The effects of solvents and surface wettability on asphaltene deposition were evaluated using two heterogeneous micromodels. Understanding the formation damage, structure of asphaltene, and deposition dynamic improves solvent-based heavy oil recovery methods. The following conclusions are the main findings of the present study:

- The detection point of asphaltene precipitation was evaluated using image processing technique. Faster precipitation was recorded for lighter solvent (n-pentane) at diluted bitumen region.
- The structure and morphology of precipitated asphaltene changed with solvent. Higher level of agglomeration and deposition was monitored using by n-pentane compared that caused lower viscosity of produced bitumen from n-pentane.
- The process of asphaltene deposition was faster than precipitation especially at pore throats of the matrix which deposition is perpendicular to the flow direction. In this constricted area slow solvent diffusion is the dominant flow mechanism and once the deposit was formed, fast deposition growth and severe pore throat blockage was noticed.
- Hydrophilic micromodel had higher level of deposition compared with hydrophobic one. Surface energy level of hydrophobic microchannel was extremely low and asphaltene had less active surfaces to attach to form deposition. Similar deposition dynamic and formation damage was recorded for zero and 45-degree micromodels.

References

[1] P. Luo and Y. Gu, "Effects of Asphaltene Content and Solvent Concentration on Heavy Oil Viscosity," SPE International Thermal Operations and Heavy Oil Symposium, 1-3 November 2005.

[2] A. Firoozabadi, Thermodynamics of Hydrocarbon Reservoirs, McGraw-Hill, New York, 1999.

[3] A. B. Demir, I. H. Bilgesu and B. Hascakir, "The Effect of Brine Concentration on Asphaltene Stability," in SPE Annual Technical Conference and Exhibition, September, Dubai, UAE, 2016.

[4] O. Mohammadzadeh Shanehsaz, "Experimental Studies Focused on the Pore-Scale Aspects of Heavy Oil and Bitumen Recovery Using the Steam Assisted Gravity Drainage (SAGD) and Solvent-Aided SAGD (SA-SAGD) Recovery Processes," University of Waterloo, Waterloo, Ontario, Canada, 2012.

[5] J. G. Speight, "The Chemical and Physical Structure of Petroleum: Effects on Recovery Operations," Journal of Petroleum Science and Engineering, vol. 22, pp. 13-15, 1999.

[6] H. Doryani, M. R. Malayeri and M. Riazi, "Visualization of asphaltene precipitation and deposition in a uniformly patterned glass micromodel," Fuel, vol. 182, pp. 613-622, 2016.

[7] F. M. Vargas, D. L. Gonzalez, J. L. Creek, J. Wang, J. Buckley and G. J. Hirasaki, "Development of a General Method for Modeling Asphaltene Stability," Energy & Fuels, vol. 23, no. 3, pp. 1147-1154, 2009.

[8] C. Stachowiak, J Viguie, J. E. Grolier, M. Rogalski, Effect of n-Alkanes on Asphaltene Structuring in Petroleum Oils, Langmuir 2005, 21, 4824-4829.

[9] S. I. Andersen, J. G. Speight, Thermodynamic Models for Asphaltene Solubility and Precipitation, Journal of Petroleum Science and Engineering, 1999, 22, 53-66.

[10] Murgich, J.; Abanero, J. A.; Strausz, O. P. Molecular recognition in aggregates formed by asphaltene and resin molecules from the Athabasca oil sand. Energy Fuels 1999, 13, 278–286.

[11] S. I. Anderson, J. G. Speight, Thermodynamic models for asphaltene solubility and precipitation, Journal of Petroleum Science and Engineering, 1999, 22, 53-66.

[12] C. Jian, T. Tang, S. Bhattacharjee, Probing the effect of side-chain length on the aggregation of a model asphaltene using molecular dynamics simulations, Energy & Fuels, 2013, 27, 2057-2067.

[13] Z.Yang, S. Chen, H. Peng, M. Li, M. Lin, Z. Dong, J. Zhang, Y. Ji, Effect of precipitating environment on asphaltene precipitation: precipitant, concentration, and temperature, Colloids and Surfaces A: Physicochemical and Engineering Aspects, 2016, 497, 327-335.

[14] D. Fenistein, L. Barre, D. Brosseta, D. Espinat, A. Livet, J. N. Roux, M. Scarsella, Viscosimetric and neutron scattering study of asphaltene aggregates in mixed toluene/heptane solvents, Langmuir 1998, 14, 1013.

[15] I. N. Evdokimov, N. Y. Eliseev, B. R. Akhmetov, Initial stages of asphaltene aggregation in dilute crude oil solution: studies of viscosity and NMR relaxation, Fuel 2003, 82, 817.

[16] A. S. Al-Qasim and M. Alasker, "Asphaltenes: what do we know so far," ASME 2017 36th International Conference on Ocean, Offshore and Arctic Engineering, pp. Trondheim, Norway, 25-30 June 2017.

[17] ECLIPSE Technical Description, "The asphaltene option," pp. 89-102, 2009.

[18] M. Tavakkoli, M. R. Grimes, X. Liu, C. K. Garcia, S. C. Correa, Q. J. Cox and F. M. Vargas, "Indirect Method: A Novel Technique for Experimental Determination of Asphaltene Precipitation," Energy & Fuels, vol. 29, pp. 2890-2900, 2015.

[19] Y. Kazemzadeh, R. Parsaei and M. Riazi, "Experimental study of asphaltene precipitation prediction during gas injection to oil reservoirs by interfacial tension measurement," Colloids and Surfaces A: Physicochemical and Engineering Aspects, vol. 466, pp. 138-146, 2015.

[20] N. Silva, V. d. R. Oliveira, M. Souza, Y. Guerrieri and G. Costa, "New method to detect asphaltene precipitation onset induced by CO_2 injection," Fluid Phase Equilibria, vol. 362, pp. 355-364, 2014.

[21] J. X. Wang and J. S. Buckley, "An experimental approach to prediction of asphaltene flocculation," in Proceedings of the SPE International Symposium on Oilfield Chemistry, Houston, TX, Feb 13−16, 2001.

[22] J. Taheri-Shakib, A. Shekarifard and H. Naderic, "Experimental investigation of the asphaltene deposition in porous media: Accounting for the microwave and ultrasonic effects," Journal of Petroleum Science and Engineering, vol. 163, pp. 453-462, 2018.

[23] N. I. Papadimitriou, G. E. Romanos, G. C. Charalambopoulou, M. E. Kainourgiakis, F. K. Katsaros and A. Stubos, "Experimental investigation of asphaltene deposition mechanism during oil flow in core samples," Journal of Petroleum Science and Engineering, vol. 57, no. 3-4, pp. 281-293, 2007.

[24] A. Memon, C. Borman, O. Mohammadzadeh, M. Garcia, D. J. R. Tristancho and J. Ratulowski, "Systematic evaluation of asphaltene formation damage of black oil reservoir fluid from Lake Maracaibo, Venezuela," Fuel, vol. 206, pp. 258-275, 2017.

[25] H. Rassamdana, B. Dabir, M. Nematy, M. Farhani and M. Sahimi, "Asphalt Flocculation and Deposition: I. The Onset of Precipitation," AIChE Journal, vol. 42, p. 3318, 1996.

[26] E. Buenrostro-Gonzalez, C. Lira-Galeana, A. Gil-Villegas and J. Wu, "Asphaltene Precipitation in Crude Oils: Theory and Experiments," AIChE Journal, vol. 50, no. 10, pp. 2552-2570, 2004.

[27] B. S. Soulgani, B. Tohidi, M. Jamialahmadi and D. Rash, "Modeling formation damage due to asphaltene deposition in the porous media," Energy & Fuels, vol. 25, no. 2, pp. 753-761, 2011.

[28] S. Wang and F. Civan, "Productivity Decline of Vertical and Horizontal Wells by Asphaltene Deposition in Petroleum Reservoirs," SPE International Symposium on Oilfield Chemistry, 13-16 February 2001.

[29] A. Taherpour, A. Cheshmeh Sefidi and A. Bemani, "Application of Fuzzy c-means algorithm for the estimation of Asphaltene precipitation," Petroleum Science and Technology, vol. 36, no. 3, pp. 239-243, 2018.

[30] S. Mohebbinia, K. Sepehrnoori, R. T. Johns and A. Kazemi Nia Korrani, "Simulation of asphaltene precipitation during gas injection using PC-SAFT EOS," Journal of Petroleum Science and Engineering, vol. 158, pp. 693-706, 2017.

[31] I. Chatzis, "Pore Scale Mechanisms of Heavy Oil Recovery using the VAPEX Process," in Proceedings: International Symposium of Society of Core Analysts, Monterey, CA, 2002.

[32] S. A. Farzaneh, A. A. Dehghan, M. H. Ghazanfari and R. Kharrat, "A Comparative Study on WAS, SWAS, and Solvent-Soak Scenarios Applied to Heavy-Oil Reservoirs Using Five-Spot Glass Micromodels," Journal of Canadian Petroleum Technology, vol. 51, no. 5, pp. 383-392, 2012.

[33] K. Keshmiri, S. Mozaffari, P. Tchoukov, H. Huang and N. Nazemifard, "Using Microfluidic Device to Study Rheological Properties of Heavy Oil," AIChE Annual Meeting and Conference, 13-18 November 2016.

[34] Y.-j. Lin, P. He, M. Tavakkoli, N. T. Mathew, Y. Y. Fatt, J. C. Chai, A. Goharzadeh, F. M. Vargas and S. L. Biswal, "Examining asphaltene solubility on deposition in model porous media," Langmuir, vol. 32, pp. 8729-8734, 2016.

[35] A. Telmadarreie and J. Trivedi, "Dynamic Behavior of Asphaltene Deposition and Distribution Pattern in Fractured Porous Media during Hydrocarbon Solvent Injection: Pore-Level Observations," Energy & Fuels, vol. 31, no. 9, pp. 9067-9079, 2017.

[36] Z. Qi, A. Abedini, A. Sharbatian, Y. Pang, A. Guerrero and D. Sinton, "Asphaltene Deposition during Bitumen Extraction with Natural Gas Condensate and Naphtha," Energy & Fuels, vol. 32, no. 2, pp. 1433-1439, 2018.

[37] Y.-J. Lin, P. He, M. Tavakkoli, N. T. Mathew, Y. Y. Fatt, J. C. Chai, A. Goharzadeh, F. M. Vargas and S. L. Biswal, "Characterizing Asphaltene Deposition in the Presence of Chemical Dispersants in Porous Media Micromodels," Energy & Fuels, vol. 31, pp. 11660-11668, 2017.

[38] V. J. Sieben, A. K. Tharanivasan, J. Ratulowski and F. Mostowfi, "Asphaltenes yield curve measurements on a microfluidic platform," Lab on a Chip, vol. 15, p. 4062, 2015.

[39] C. Hu, J. E. Morris and R. L. Hartman, "Microfluidic investigation of the deposition of asphaltenes in porous media," Lab on a Chip, vol. 14, pp. 2014-2022, 2014.

[40] X. Liu, P. K. Chu and C. Ding, "Surface modification of titanium, titanium alloys, and related materials for biomedical applications," Materials Science and Engineering: R: Reports, vol. 47, no. 3-4, pp. 49-121, 2004.

[41] S. Li, M. Genys, K. Wang and O. Torsæter, "Experimental study of wettability alteration during nanofluid enhanced oil recovery process and its effect on oil recovery," in SPE

Reservoir Characterisation and Simulation Conference and Exhibition, Abu Dhabi, UAE, 2015.

[42] X. Sun, C. Dai, Y. Sun, M. Du, T. Wang, C. Zou and J. He, "Wettability alteration study of supercritical CO_2 fracturing fluid on low permeability oil reservoir," Energy & Fuels, vol. 31, no. 12, p. 13364–13373, 2017.

[43] P. P. Jadhunandan and N. Morrow, "Effect of wettability on waterflood recovery for crude-oil/brine/rock systems," Society of Petroleum Engineers, vol. 10, no. 1, 1995.

[44] M. Khishvand, A. H. Alizadeh, I. O. Kohshour, M. Piri and R. S. Prasad, "In situ characterization of wettability alteration anddisplacement mechanisms governing recovery enhancementdue to low-salinity waterflooding," Water Resources Research, vol. 53, p. 4427–4443, 2017.

[45] K. L. Mittal, Silanes and other coupling agents, CRC Press, Leiden, 2009.

[46] H. Alboudwarej, D. Pole, W. Y. Svrcek and H. W. Yarranton, "Adsorption of asphaltenes on metals," Industrial & Engineering Chemistry Research, vol. 44, no. 15, p. 5585, 2005.

[47] K. R. Dean and J. L. McAtee Jr, "Asphaltene adsorption on clay," Applied Clay Science, vol. 1, no. 4, pp. 313-9, 1986.

[48] A. Zahabi and M. R. Gray, "Kinetics and Properties of Asphaltene Adsorption on Surfaces," Energy & Fuels, vol. 26, p. 1009−1018, 2012.

[49] S. Pendharker, S. Shende, W. Newman, S. Ogg, N. Nazemifard, Z. Jacob, “Axial super-resolution evanescent wave tomor,” Opt. Lett., 41, 5499-5502, 2016.

[50] H. T. Zhang, R. Li, Z. Yang, C. X. Yin, M. R. Gray, C. Bohne, “Evaluating steady-state and time-resolved fluorescence as a tool to study the behavior of asphaltene in toluene.” Photochem. Photobiolog. Sci., 13, 917-928, 2014.

[51] Axelrod D. Total internal reflection fluorescence microscopy. Methods Cell Biol 2008;89:169–221.

[52] Shen H, Huang E, Das T, Xu H, Ellisman M, Liu Z. Tirf microscopy with ultrashort penetration depth. Opt Express 2014;22(9):10728–34.

[53] Hooshiar, A.; Uhlik, P.; Ivey, D. G.; Liu, Q.; Etsell, T. H. Clay minerals in nonaqueous extraction of bitumen from Alberta oil sands: Part 2. Characterization of clay minerals. Fuel Process. Technol. 2012, 96, 183−194.

[54] H. Fadaei, J. M. Shaw and D. Sinton, "Bitumen-Toluene Mutual Diffusion Coefficients Using Microtluidics," Energy & Fuels, vol. 27, pp. 2042-2048, 2013.

[55] M. M. Shadman, A. H. Saeedi Dehaghani and M. H. Badizad, "How much do you know about the methods for determining onset of asphaltene precipitation?," Petroleum, vol. 3, pp. 287-291, 2017.

[56] T. Maqbool, A. T. Balgoa, H. S. Fogler, “Revisiting asphaltene precipitation from crude oils: a case of neglected kinetic effects,” Energy & Fuels, vol. 23, pp. 3681-3686, 2009.

[57] F. Trejo, J. Ancheyta, M. S. Rana, “Structural characterization of asphaltene obtained hydroprocessed crude oils by SEM and TEM” Energy & Fuels, 23, 429–439, 2009.

[58] J. Wang, Q. Shi, Z. Huang, Y. Gu, L. Musango, Y. Yang, “Experimental investigation of particle size effect on agglomeration behaviors in gas-solid fluidized beds” Ind. Eng. Chem. Res., 54, 12177−12186, 2015.

[59] N. Jouault, Y. Corvis, F. Cousin, J. Jestin, L. Barre, “Asphaltene Adsorption Mechanisms on the Local Scale Probed by Neutron Reflectivity: Transition from Monolayer to Multilayer Growth above the Flocculation Threshold,” Langmuir, 25, 3991-3998, 2009.

Chapter 7: Concluding Remarks and Future Works

7.1. Concluding Remarks

The focus of this doctoral research is mainly on application of microfluidic platforms on energy sector and more precisely on bitumen extraction. It was first understood that glass is the most suitable substance of micromodel fabrication for heavy oil and bitumen studies. Using etched glass micromodels, three main topics related to solvent-based heavy oil and bitumen extraction were investigated. Summary of remarkable findings based on this thesis are provided below:

- Application of PDMS as a cost and time-effective material in bitumen studies was evaluated first. Different PDMS slabs (curing agent to base ratio) were fabricated and compared based on swelling ratio in pure solvents and bitumen. High swelling of PDMS slabs submerged in solvents and bitumen makes it inappropriate for evaluation of heavy oil and bitumen flow during the solvent-based extraction. Effect of surface modification on resistivity of PDMS slabs confirmed that silanization was not able to decrease the swelling and deformation in presence of solvent and bitumen. In addition to deformation of PDMS microchannel, transparency was also decreased as bitumen penetrated in microchannel and the quality of visualization of the process in not qualitatively accepted. TIRF microscopy showed fast bitumen concentration growth on PDMS surface and transparency of the microchannel was decreased accordingly.

- First a T-shaped microchannel was fabricated to measure diffusion coefficient of hexane into bitumen. Single-file and Fickian diffusion mass transfer mechanisms were evaluated

and superimposition of n_w values of different concentrations confirms the Fickian mechanism of solvent diffusion in bitumen. Detection point of asphaltene precipitation was also calculate, relating the image intensities to solvent concentration and the first point of intensity reduction was considered as detection point when the color of solvent-rich section became darker due to the asphaltene particles. Constant and concentration dependent diffusion coefficients were determined and experimental concentration results were compared with simulation data.

- After evaluation of solvent diffusion in bitumen, capillary-driven flow of diluted bitumen and pure liquids in straight and periodically constricted microchannels were evaluated. Interface position of pure liquids, 10%, and 20% diluted bitumen as a function of time followed the Washburn theoretical model prediction for hydrophilic and HMDS treated microchannels. Dynamic contact angles were different from constant static contact angles that are mostly used in simulation. In fact, static contact angle causes higher deviation between experimental and simulation results. PFOCTS treated microchannel had an increasing deviation between experiment and model results for diluted bitumen because of extremely low surface energy and absence of silanol groups at the channel.

- Sinusoidal capillary was simulated using Navier-Stokes equation while Washburn model was not able to predict the experimental results. High accuracy of simulation confirms the importance of geometry on dynamic contact angle while theoretical models like Washburn are not suitable in reservoir simulation with complicated structure.

- Asphaltene precipitation and deposition from n-alkane solvents in 2D microchannels was studied as the second phenomena of solvent diffusion in bitumen. In addition to detection of asphaltene precipitation that was previously mentioned, structure of asphaltene precipitated from different solvents were analyzed and compared with a 3D reconstruction of the fluorescence images of asphaltene. It was noticed that lighter solvent (n-pentane) produced more asphaltene with high level of agglomeration and coagulation. Moreover, higher formation damage and pore blockage was noticed for n-pentane. Surface wettability had a minor effect on asphaltene deposition with higher degree of deposition on hydrophilic microchannel.

7.2. Future Works

There are many aspects of this work for future investigation that might help to answer some uncovered questions and a few of them are mentioned below:

- Diffusion of gaseous solvent in bitumen is another important phenomenon in solvent-based extraction methods. In fact, solvent vapor diffuses into the bitumen and condenses on the bitumen interface and reduces viscosity through heat conduction and mass transfer. Experimental observation of heat transfer together with mass transfer provides direct evidence of how both phenomena interact to improve the solvent extraction techniques. Evaluation of tertiary solid-like phase during the diffusion with different solvent expected to be different and even more complicated in cases with lower precipitation rate compared with hexane. Experimental diffusion mass transfer mechanism of various solvents should be further investigated. Improvement of simulation

results depends on different parameters such as assumptions in the mathematical model and boundary conditions. Each of the assumptions and boundary conditions are recommended to evaluate individually rather than a combination of parameters.

- Although image processing technique is an indirect method of concentration profile measurement, accuracy of this method could be easily disturbed. It would be desirable to compare this results with other well-known methods such CT-scanner.

- A powerful mathematical model for the capillary filling of microchannel with variable cross-section is essential to accurately predict the fluid flow. Bitumen flow in 2D microchannel is a more complicated case of study for modeling of multi-phase flow in porous media. In addition to capillary-drive flow study, evaluation of pressure-driven flow is essential for fluid flow in bitumen extraction. A comparison between hydrophobic microchannel treated with silane and microchannel wetted with oil before the injection of pure liquids and diluted bitumen will help to analyze the effect of surface energy and wettability alteration in different approaches.

- Dynamic of asphaltene precipitation and deposition is different based on injected solvent. Simulation of precipitation, flocculation, and deposition of asphaltene particle in porous media can improve reservoir simulation.

- Temperature affects the stability and kinetics of deposition. A thorough visualization of combined effective parameters is recommended. In addition, hydrodynamic effects on deposition was not considered here. Although larger solvent flow rate caries asphaltene

particles and deposition is lower, higher flow rate causes larger pressure drop that is not desired. Water is always present in reservoir and effect of water on asphaltene precipitation and most probably on asphaltene deposition is challenging. Surfactant effects of asphaltene stabilize the water-in-oil emulsion and presence of asphaltene particles in water-oil interface means less asphaltene available for deposition. Therefore, it is crucial to investigate water contribution on asphaltene deposition.

Bibliography

Chapter 1

[1] L. A. James, Mass Transfer Mechanisms during the Solvent Recovery of Heavy Oil (Doctoral dissertation), Waterloo: Retrieved from ProQuest Dissertations & Theses Global, 2009.

[2] Oil and Gas Journal, Alberta Energy Regulator and Canadian Association of Petroleum Producers, 2015.

[3] O. V. Trevisan, A. C. L. Lisboa, F. A. França and W. Trindade, "Oil production in offshore fields: An overview of the Brazilian technology development," in World Heavy Oil Conference, Pequim, 2006.

[4] A. K. Mehrotra, "A model for the viscosity of bitumen/bitumen fractions-diluent blends," Journal of Canadian Petroleum Technology, vol. 31, no. 9, pp. 28-32, 1992.

[5] R. M. Butler, Thermal Recovery of Oil and Bitumen, Englewood Cliffs, NJ: Prentice Hall, 1991.

[6] M. Keshavarz, R. Okuno and T. Babadagli, "Efficient oil displacement near the chamber edge in ES-SAGD," Journal of Petroleum Science and Engineering, vol. 118, pp. 99-113, 2014.

[7] R. M. Butler and I. J. Mokrys, "Recovery of Heavy Oils Using Vaporized Hydrocarbon Solvents: Further Development of the VAPEX Process," in etroleum Conference of The South Saskatchewan, Regina, 1992.

[8] R. Luhning, S. Das, L. Fisher, J. Bakker, J. Grabowski, J. Engleman, S. Wong, L. Sullivan and H. Boyle, "Full Scale VAPEX Process-Climate Change Advantage and Economic Consequences," Journal of Canadian Petroleum Technology, vol. 42, no. 2, pp. 31-34, 2003.

Chapter 2

[1] BP, "BP Statistical Review of World Energy," http://bp.com/statisticalreview2016, 2017. [Online].

[2] D. Sinton, "Energy: the microfluidic frontier," Lab on a Chip, vol. 14, p. 3127, 2014.

[3] C. J. Campbell and J. H. Laherr`ere, "The end of cheap oil," Scientific American, 1998.

[5] J.-N. Jaubert, L. Avaullee and J.-F. Souvay, "A crude oil data bank containing more than 5000 PVT and gas injection data," Journal of Petroleum Science and Engineering, vol. 34, no. 1-4, pp. 65-107, 2002.

[6] P. Nguyen, D. Mohaddes, J. Riordon, H. Fadaei, P. Lele and D. Sinton, "Fast Fluorescence-Based Microfluidic Method for Measuring Minimum Miscibility Pressure of CO_2 in Crude Oils," Analytical Chemistry, vol. 87, pp. 3160-3164, 2015.

[7] H. Fadaei, B. Scarff and D. Sinton, "Rapid Microfluidics-Based Measurement of CO_2 Diffusivity in Bitumen," Energy & Fuels, pp. 4829-4835, 2011.

[8] C. A. Conn, K. Ma, G. J. Hirasaki and S. L. Biswal, "Visualizing oil displacement with foam in a microfluidic device with permeability contrast," Lab on a Chip, vol. 14, no. 20, pp. 3968-77, 2014.

[9] M. A. Modestino, D. F. Rivas, S. M. H. Hashemi, J. G. E. Gardeniers and D. Psaltis, "The potential for microfluidics in electrochemical energy systems," Energy & Environmental Science , vol. 9, p. 3381, 2016.

[10] P. P. Edwards, V. L. Kuznetsov, W. I. F. David and N. P. Brandon, "Hydrogen and fuel cells: Towards a sustainable energy future," Energy Policy, vol. 36, no. 12, pp. 4356-4362, 2008.

[11] J. Lee, K. G. Lim, G. T. R. Palmore and A. Tripathi, "Optimization of Microfluidic Fuel Cells Using Transport Principles," Analytical Chemistry, vol. 79, pp. 7301-7307, 2007.

[12] E. Kjeang, N. Djilali and D. Sinton, "Microfluidic fuel cells: A review," Journal of Power Sources, vol. 186, p. 353–369, 2009.

[13] O. Morton, "Solar energy: A new day dawning?: Silicon Valley sunrise," Nature, vol. 443, pp. 19-22, 2006.

[14] S. S. Ahsan, A. Gumus and D. Erickson, "Redox mediated photocatalytic water-splitting in optofluidic microreactors," Lab on a Chip, vol. 13, p. 409, 2013.

[15] Z. Meng, X. Zhang and J. Qin, "A high efficiency microfluidic-based photocatalytic microreactor using electrospun nanofibrous TiO2 as a photocatalyst," Nanoscale, vol. 5, no. 11, pp. 4687-4690, 2013.

[16] S. C. Roy, O. K. Varghese, M. Paulose and C. A. Grimes, "Toward Solar Fuels: Photocatalytic Conversion of Carbon Dioxide to Hydrocarbons," ACS Nano, vol. 4, no. 3, p. 1259–127, 2010.

[17] S. Haldrup, J. Catalano, M. R. Hansen, M. Wagner, G. V. Jensen, J. S. Pedersen and A. Bentien, "High Electrokinetic Energy Conversion Efficiency in Charged Nanoporous Nitrocellulose/Sulfonated Polystyrene Membranes," Nano Letters, vol. 15, pp. 1158-1165, 2015.

[18] V. A. Lifton, "Microfluidics: an enabling screening technology for enhanced oil recovery (EOR)," Lab on a Chip, vol. 16, p. 1777, 2016.

[19] P. Nguyen, D. Mohaddes, J. Riordon, H. Fadaei, P. Lele and D. Sinton, "Fast fluorescence-based microfluidic method for measuring minimum miscibility pressure of CO_2 in crude oils," Analytical Chemistry, vol. 87, no. 6, p. 3160–3164, 2015.

[20] M. H. Schneider, V. J. Sieben, A. M. Kharrat and F. Mostowfi, "Measurement of asphaltenes using optical spectroscopy on a microfluidic platform," Analytical Chemistry, vol. 85, p. 5153–5160, 2013.

[21] S. G. R. Lefortier, P. J. Hamersma, A. Bardow and M. T. Kreutzer, "Rapid microfluidic screening of CO_2 solubility and diffusion in pure and mixed solvents," Lab on a Chip, vol. 12, no. 18, pp. 3387-3391, 2012.

[22] M. Buchgraber, A. R. Kovscek and L. M. Castanier, "A study of microscale gas trapping using etched silicon micromodels," Transport Porous Media, vol. 95, no. 3, pp. 647-668, 2012.

[23] A. Danesh, PVT and phase behavior of petroleum reservoir fluids, ElsevierScience, 1998.

[24] S. Molla and F. Mostowfi, "Microfluidic PVT-saturation pressure and phase -volume measurement of black oil," in SPE Annual Technical Conference and Exhibition, Amsterdam, 2014.

[25] O. V. Trevisan, A. C. L. Lisboa, F. A. França and W. Trindade, "Oil production in offshore fields: An overview of the Brazilian technology development," in World Heavy Oil Conference, Pequim, 2006.

[26] R. M. Butler, Thermal Recovery of Oil and Bitumen, Englewood Cliffs, NJ: Prentice Hall, 1991.

[27] R. M. Butler and I. J. Mokrys, "Recovery of heavy oils using vaporized hydrocarbon solvents: further development of the VAPEX process," in Technical Meeting / Petroleum Conference of The South Saskatchewan Section, Regina, 1992.

[28] L. A. James, Mass Transfer Mechanisms during the Solvent Recovery of Heavy Oil (Doctoral dissertation), Waterloo: Retrieved from ProQuest Dissertations & Theses Global, 2009.

[29] O. Mohammadzadeh Shanehsaz, "Experimental Studies Focused on the Pore-Scale Aspects of Heavy Oil and Bitumen Recovery Using the Steam Assisted Gravity Drainage (SAGD) and Solvent-Aided SAGD (SA-SAGD) Recovery Processes," University of Waterloo, Waterloo, Ontario, Canada, 2012.

[30] T. Nasr, G. Beaulieu, H. Golbeck, G. Heck, "Novel expanding solvent-SAGD process "ES-SAGD," Journal of Canadian Petroleum Technology, vol. 42, 2003.

[31] G. B. Lim, P. R. Kry, J. P. Lebel, M. Y. Kwan, "Cyclic solvent process for in-situ bitumen and heavy oil production," Patent CA2349234, 2004.

[32] J. Nenniger, E. Nenniger, "Method and apparatus for stimulating heavy oil production," Patent CA2567399C.

[33] R. Leaute, "Liquid addition to steam for enhancing recovery (LASER) of bitumen with CSS: Evolution of technology from research concept to a field pilot at Cold Lake," SPE International Thermal Operations and Heavy Oil Symposium, Calgary, Canada, 2002.

[34] F. Torabi, B. Yadali Jamaloei, B. M. Stengler and D. E. Jackson, "The evaluation of CO_2 based vapour extraction (VAPEX) process for heavy-oil recovery," Journal of Petroleum Exploration and Production Technology, vol. 2, pp. 93-105, 2012.

[35] G. Q. Wu, A. Kantzas and D. Salama, "Computed tomography study of VAPEX process in laboratory 3D model," Journal of Canadian Petroleum Technology, vol. 49, pp. 40-47, 2010.

[36] T. W. de Haas, H. Fadaei, U. Guerrerob and D. Sinton, "Steam-on-a-chip for oil recovery: the role of alkaline additives in steam assisted gravity drainage," Lab on a Chip, vol. 13, pp. 3832-3839, 2013.

[37] Z. Qi, A. Abedini, P. Lele, N. Mosavat, A. Guerrero and D. Sinton, "Pore-scale analysis of condensing solvent bitumen extraction," Fuel, vol. 193, p. 284–293, 2017.

[38] L. A. James, N. Rezaei and I. Chatzis, "VAPEX, warm VAPEX and hybrid VAPEX – the state of enhanced oil recovery for in situ heavy oils in canada," Journal of Canadaian Petroleum Technology, vol. 47, no. 4, 2008.

[39] F. Mostowfi, J. Czarnecki, J. Masliyah and S. A. Bhattacharjee, "microfluidic electrochemical detection technique for assessing stability of thin films and emulsions," Journal of Colloidal Interface Science, vol. 317, no. 2, pp. 593-603, 2008.

[40] B. Bao, J. Riordon, F. Mostowfi and D. Sinton, "Microfluidic and nanofluidic phase behaviour characterization for industrial CO_2, oil and gas," Lab on a Chip, vol. 17, pp. 2740-2759, 2017.

[41] M. K. Shah, R. Fisher, I. Hassan, E. Makarov, O. Medvedev and A. Memon, "Measuring Reservoir Fluid Composition Using a Novel Continuous Contact Flash Method Based on a Microfluidic Device," in Abu Dhabi International Petroleum Exhibition and Conference, Abu Dhabi, UAE, 2015.

[42] V. J. Sieben, A. K. Tharanivasan, S. I. Andersen and F. Mostowfi, "Microfluidic approach for evaluating the solubility of crude oil asphaltenes," Energy & Fuels, vol. 30, p. 1933−1946, 2016.

[43] A. Hammami, C. H. Phelps, T. Monger-McClure and T. M. Little, "Asphaltene precipitation from live oils: an experimental investigation of onset conditions and reversibility," Energy & Fuels, vol. 14, pp. 14-18, 2000.

[44] M. Tavakkoli, P. He, P.-H. Lin, S. Rezaee, M. Puerto, R. Doherty, J. Creek, S. L. Biswal and F. M. Vargas, "Asphaltene deposition and fouling in reservoirs," in Offshore Technology Conference, Houston, Texas, USA, 2017.

[45] K. Ren, J. Zhou and H. Wu, "Materials for Microfluidic Chip Fabrication," Accounts of Chemical Research, vol. 46, no. 11, pp. 2396-2406, 2012.

[46] C. H. Lin, G. B. Lee, Y. H. Lin and G. L. Chang, "A fast prototyping process for fabrication of microfluidic systems on soda-lime glass," Journal of Micromechanics and Microengineering, vol. 11, pp. 726-732, 2001.

[47] S. K. Yap, W. K. Wong, N. X. Y. Ng and S. A. Khan, "Three-phase microfluidic reactor networks – Design, modeling and application to scaled-out nanoparticle-catalyzed hydrogenations with online catalyst recovery and recycle," Chemical Engineering Science, vol. 169, pp. 117-127, 2017.

[48] K. Keshmiri, S. Mozaffari, P. Tchoukov, H. Huang and N. Nazemifard, "Using Microfluidic Device to Study Rheological Properties of Heavy Oil," in AIChE Annual Meeting, San Francisco, 2016.

[49] D. Ciceri, J. M. Perera and G. W. Stevens, "The use of microfluidic devices in solvent extraction," Journal of Chemical Technology and Biotechnology, vol. 89, p. 771–786, 2014.

[50] M. Saqib, O. B. Şahinoğlu and E. Y. Erdem, "Alternating droplet formation by using tapered channel geometry," Scientific Reports, vol. 8, p. 1606, 2018.

[51] K. Ren, J. Zhou and H. Wu, "Materials for Microfluidic Chip Fabrication," Accounts of Chemical Research, vol. 46, no. 11, pp. 2396-2406, 2013.

[52] K. Ren and R. N. Zare, "Chemical Recognition in Cell-Imprinted Polymers," ACS Nano, vol. 6, pp. 4314-4318, 2012.

Chapter 3

[1] C. Hu, J. E. Morris and R. L. Hartman, "Microfluidic investigation of the deposition of asphaltenes in porous media," Lab on a Chip, vol. 14, no. 12, pp. 2014-2022, 2014.

[2] S. Molla and F. Mostowfi, "Microfluidic PVT–Saturation Pressure and Phase-Volume Measurement of Black Oils," SPE Reservoir Evaluation & Engineering, vol. 20, no. 1, pp. 233-239, 2017.

[3] R. Fisher, M. K. Shah, D. Eskin, K. Schmidt, A. Singh, S. Molla and F. Mostowfi, "Equilibrium gas–oil ratio measurements using a microfluidic technique," Lab on a Chip, vol. 13, pp. 2623-2633, 2013.

[4] K. Keshmiri, S. Mozaffari, P. Tchoukov, H. Huang and N. Nazemifard, "Using Microfluidic Device to Study Rheological Properties of Heavy Oil," in American Institude of Chemical Engineering (AIChE), San Francico, CA, USA, 2016.

[5] K. Xu, T. Liang , P. Zhu, P. Qi, J. Lu, C. Huh and M. Balhoff, "A 2.5-D glass micromodel for investigation of multi-phase flow in porous media," Lab on a Chip, vol. 17, pp. 640-646, 2017.

[6] J. P. Esquivel, F. J. Del Campo, J. L. Gómez de la Fuente, S. Rojas and N. Sabaté, "Microfluidic fuel cells on paper: meeting the power needs of next generation lateral flow devices," Energy and Environmental Scienece, vol. 7, pp. 1744-1749, 2014.

[7] G. Pasirayi, V. Auger, S. Scott, P. Rahman, M. Islam, L. O'Hare and Z. Ali, "Microfluidic Bioreactors for Cell Culturing: A Review," Micro and Nanosystems, vol. 3, pp. 137-160, 2011.

[8] L. Va, "Microfluidics: an enabling screening technology for enhanced oil recovery (EOR)," Lab on a Chip, vol. 16, no. 10, pp. 1777-1796, 2016.

[9] P. Lele, A. H. Syed, J. Riordon, N. Mosavat, A. Guerrero, H. Fadaei and D. Sinton, "Deformation of microdroplets in crude oil for rapid screening of enhanced oil recovery additives," Journal of Petroleum Science and Engineering, Vols. In Press, Accepted Manuscript, 2018.

[10] H. Lee, S. G. Leeb and P. S. Doyle, "Photopatterned oil-reservoir micromodels with tailored wetting properties," Lab Chip, vol. 15, p. 3047, 2015.

[11] D. Reyes, D. Iossifidis, P. A. Auroux and A. Manz, "Micro total analysis systems. 1. Introduction, theory, and technology," Anal Chem, vol. 74, no. 12, pp. 2623-36, 2002.

[12] E. Carrilho, S. M. Lunte and W. K. T. Coltro, "Comparison of the analytical performance of electrophoresis microchannels fabricated in PDMS, glass, and polyester-toner," Electrophoresis, vol. 29, no. 24, p. 4928–4937, 2008.

[13] M. Hashimoto, R. Langer and D. S. Kohane, "Benchtop fabrication of microfluidic systems based on curable polymers with improved solvent compatibility," Lab Chip, vol. 13, pp. 252-259, 2013.

[14] E. Leclerc, Y. Sakai and T. Fujii, "Microfluidic PDMS (Polydimethylsiloxane) Bioreactor forLarge-Scale Culture of Hepatocytes," Biotechnology Progress, vol. 20, pp. 750-755, 2004.

[15] M. Yao and J. Fang, "Hydrophilic PEO-PDMS for microfluidic applications," Journal of Micromechanics and Microengineering, vol. 22, no. 2, p. 025012, 2012.

[16] J. Ng Lee, C. Park and G. M. Whitesides, "Solvent Compatibility of Poly(dimethylsiloxane)-Based Microfluidic Devices," Analytical Chemistry, vol. 75 (23), p. 6544–655, 2003.

[17] J. Ng, I. Gitlin, A. Stroock and G. Whitesides, "Components for integrated poly(dimethylsiloxane) microfluidic systems," Electrophoresis, vol. 23(20), pp. 3461-73, 2002.

[18] I. D. Johnston, D. K. McCluskey, C. K. L. Tan and M. C. Tracey, "Mechanical characterization of bulk Sylgard 184 for microfluidics and microengineering," Journal of Micromechanics and Microengineering, vol. 24, p. 35017, 2014.

[19] C. Xiang, N. Yang, R. Zhang, J. Guo and H. Huang, "An Ultraviolet-Visible (UV) Photometry System Based on the PDMS-based Microfluidic Chip," in 13th Global Congress on Manufacturing and Management (GCMM 2016), 2017.

[20] K. Khanafer, A. Duprey, M. Schlicht and R. Berguer, "Effects of strain rate, mixing ratio, and stress–strain definition on the mechanical behavior of thepolydimethylsiloxane (PDMS) material as related to its biological applications," Biomed. Microdevices, vol. 11, no. 2, pp. 503-508, 2009.

[21] Z. Wang, "Polydimethylsiloxane mechanical properties measured by macro-scopic compression and nanoindentation techniques," PhD. thesis, University of South Florida, 2011.

[22] R. Seghir and S. Arscott, "Extended PDMS stiffness range for flexible systems," Sensors and Actuators, vol. 230, no. A, pp. 33-39, 2015.

[23] F. Saryazdi, H. Motahhari, F. F. Schoeggl, S. D. Taylor and H. W. Yarranton, "Density of Hydrocarbon Mixtures and Bitumen Diluted with Solvents and Dissolved Gases," Energy and Fuels, vol. 27, no. 7, pp. 3666-3678, 2013.

[24] A. R. Abate, D. Lee, T. Do, C. Holtzea and D. A. Weitz, "Glass coating for PDMS microfluidic channels by sol–gel methods," Lab Chip, vol. 8, pp. 516-518, 2008.

[25] S. H. Cho, J. Godin and Y. Lo, "Optofluidic Waveguides in Teflon AF-Coated PDMS Microfluidic Channels," IEEE Photonics Technol Lett, vol. 21, no. 15, p. 1057–1059, 2009.

[26] G. A. Diaz-Quijada and D. D. M. Wayner, "A Simple Approach to Micropatterning and Surface Modification of Poly(dimethylsiloxane)," Langmuir, vol. 20, pp. 9607-11, 2004.

[27] M. Khorasani and H. Mirzadeh, "Laser surface modification of silicone rubber to reduce platelet adhesion in vitro," J Biomater Sci Polym Ed, vol. 15, no. 1, pp. 59-72, 2004.

[28] Z. Pan, H. Shahsavan, W. Zhang, F. K. Yang and B. Zhao, "Superhydro-oleophobic bio-inspired polydimethylsiloxane micropillared surface via FDTS coating/blending approaches," Applied Surface Science, vol. 324, pp. 612-620, 2015.

[29] R. M. Diebold and D. R. Clarke, "Smooth, Aggregate-Free Self-Assembled Monolayer Deposition of Silane Coupling Agents on Silicon Dioxide," Langmuir, vol. 28, no. 44, pp. 15513-15520, 2012.

[30] S. S. Shende, S. Pendharker, Z. Jacob and N. Nazemifard, "Total Internal Reflection Fluorescence Microscopy To Investigate the Distribution of Residual Bitumen in Oil Sands Tailings," Energy Fuels, vol. 30, no. 7, p. 5537–5546, 2016.

[31] Y. Du, Y. Xue and H. L. Frisch, Physical Properties of Polymers Handbook, Woodbury, NY: AIP Press, 1996.

[32] T. Ougizawa and T. Inoue, Miscibility and interfacial behavior in polymer-polymer mixtures, in polymer blends and alloys, NY, chapter 3: Marcel Dekker, Inc, 1999.

[33] C. V. Rumens, M. A. Ziai, K. E. Belsey, J. C. Batchelor and S. J. Holder, "Swelling of PDMS networks in solvent vapours; applications for passive RFID wireless sensors," J. Mater. Chem. C, pp. 10091-10098, 2015.

[34] C. M. Hansen, "50 Years with solubility parameters—past and future," Progress in Organic Coatings, vol. 51, pp. 77-84, 2004.

[35] X. Su, B. Shi and L. Wang, "Investigation on Three-Dimensional Solubility Parameters for Explanation and Prediction of Swelling Degree of Polydimethylsiloxane Pervaporation Membranes," Journal of Macromolecular Science, vol. 54, p. 1248–1258, 2015.

[36] C. M. Hansen, Hansen Solubility Parameters: A User's Handbook, Boca Raton: CRC Press, 2007.

[37] Y. Kusano, S. Teodoru and C. M. Hansen, "The physical and chemical properties of plasma treated ultra-high-molecular-weight polyethylene fibers," Surface and Coatings Technology, vol. 205, p. 2793–2798, 2011.

[38] J. Bruke, Solubility parameters: theory and application, Harvard, 1984.

[39] H. Soltane, D. Roizard and E. Favre, "Effect of pressure on the swelling and fluxes of dense PDMS membranes in nanofiltration: an experimental study," J. Membr. Sci., vol. 435, p. 110–119, 2013.

[40] F. Handle, J. Füssl, S. Neudl, D. Grossegger, L. Eberhardsteiner, B. Hofko, M. Hospodka, R. Blab and H. Grothe, "The bitumen microstructure: a fluorescent approach," Materials and Structures, vol. 49, no. 1-2, pp. 167-180, 2016.

[41] N. A. Diachun, A. H. Marcus and M. D. Fayer, "Dynamics in Polydimethylsiloxane: The Effect of Solute Polarity," Journal of American Chemical Society, vol. 116, pp. 1027-1032, 1994.

[42] D. J. Campbell and S. B. Rupe, "Solvent Swelling and Optical Rotation Demonstrated on the Overhead Projector," Journal of Chemical Education, vol. 77, no. 7, 2000.

[43] J. G. Kushmeric, M. G. Hankins, M. de Boer, P. J. Clews and R. Carpick, "The influence of coating structure on micromachine stiction," Tribology Letters, vol. 10, no. 1-2, pp. 103-108, 2001.

Chapter 4

[1] O. V. Trevisan, A. C. L. Lisboa, F. A. França, W. Trindade, “Oil production in offshore fields: an overview of the Brazilian technology development,” World Heavy Oil Conference, 13-15 November, Beijing, China, 2006.

[2] R. M. Butler, “Thermal recovery of oil and bitumen,” Old Tappan, NJ: Prentice Hall Inc., 1991.

[3] J. K. Fairbridge, E. Cey, I. D. Gates, “Impact of intraformational water zones on SAGD performance,” Journal of Petroleum Science and Technology, vol. 82, pp. 187-97, 2012.

[4] M. Keshavarz, R. Okuno, T. Babadagli, “Efficient oil displacement near the chamber edge in ES-SAGD,” Journal of Petroleum Science and Engineering, vol. 118, pp. 99-113, 2014.

[5] R. M. Butler, I. J. Mokrys, “Recovery of heavy oils using vaporized hydrocarbon solvents: further development of the VAPEX process,” SPE Annual Technical Conference and Exhibition, 7-9 October, Regina, Canada, 2011.

[6] B. Zhao, M. Becerra, J. M. Shaw, “On asphaltene and resin association in Athabasca bitumen an Maya crude oil,” Energy & Fuels, vol. 23, pp. 4431-37, 2009.

[7] B. Zhao, J. M. Shaw, “Composition and size distribution of coherent nanostructures in Athabasca bitumen and Maya Crude oil,” Energy & Fuels, vol. 21, pp. 2795-2804, 2007.

[8] H. Jobic, K. Hahn, J. Karger, M. Bee, A. Tuel, M. Noack, I. Girnus, G. Kearley, “Unidirectional and Single-File diffusion of molecules in one-dimensional channel system A quasi-elastic neutron scattering study,” The Journal of Physical Chemistry B, vol. 101, pp. 5834-41, 1997.

[9] K. Hahn, J. Kärger, V. Kukla, “Single-File diffusion observation,” Physical Review Letters, vol. 76, pp. 2762, 1996.

[10] S. Gupta, S. Gittins, P. Picherack, “Insights into some key issues with solvent aided process,” Journal of Canadian Petroleum Technology, vol. 43, pp. 54-61, 2003.

[11] S. R. Etminan, “Determination of mass transfer parameters in solvent-based oil recovery processes,” SPE Annual Technology Conference Exhibition, 8-10 October, San Antonio, USA, 2012.

[12] M. R. Riazi, “A new method for experimental measurement of diffusion coefficients in reservoir fluids,” Journal of Petroleum Science and Engineering, vol. 14, pp. 235-50, 1996.

[13] X. Zhang, M. Fulem, J. M. Shaw, “Liquid-phase mutual diffusion coefficients for Athabasca bitumen + pentane mixtures,” Journal of Chemical & Engineering Data, vol. 52, pp. 691-94, 2007.

[14] S. K. Das, R. M. Butler, “Diffusion coefficient of propane and butane in Peace river bitumen,” Canadian Journal of Chemical Engineering, vol. 74, pp. 985-92, 1996.

[15] S. Bobroff, R. J. Philips, A. Shekarriz, “Nuclear magnetic resonance measurement of ammonia diffusion in dense solid-liquid slurries,” Pacific Northwest National Laboratory, 1997.

[16] M. E. King, R. W. Pitha, S. F. Sontum, “A laser refraction method for measuring liquid diffusion coefficients,” Journal of Chemical Education, vol. 66, pp. 787, 1989.

[17] Y. Wen, A. Kantzas, G. J. Wang, “Estimation of diffusion coefficients in bitumen solvent mixtures using X-ray CAT scanning and low field NMR,” 5th Canadian International Petroleum Conference, June 8-10 Calgary, Canada, 2004.

[18] A. K. Tharanivasan, C. Yang, Y. Gu, “Measurements of molecular diffusion coefficients of carbon dioxide, methane, and propane in heavy oil under reservoir conditions,” Energy & Fuels, vol. 20, pp. 2509-18, 2006.

[19] V. Oballa, R. Butler, “An experimental-study of diffusion in the bitumen-toluene system,” Journal of Canadian Petroleum Technology, vol. 28, pp. 63-90, 1989.

[20] M. Alizadehgiashi, J. M. Shaw, “Fickian and non-Fickian diffusion in heavy oil + light hydrocarbon mixtures,” Energy & Fuels, vol. 29, pp. 2177-89, 2015.

[21] M. Pourmohammadbagher, “Fickian to Single-File diffusion transition in nano-colloids,” MSc Thesis, University of Alberta, Edmonton, Canada, 2018.

[22] V. Berejnov, N. Djilali, D. Sinton, “Lab-on-chip methodologies for the study of transport in porous media: energy applications,” Lab-on-a-Chip, vol. 8, pp. 689-93, 2008.

[23] J. Wan, J. L. Wilson, “Visualization of the role of the gas-water interface on the fate and transport of colloids in porous media,” Water Resources Research, vol. 30, pp. 11-23, 1994.

[24] K. Keshmiri, S. Mozaffari, P. Tchoukov, H. Huang, N. Nazemifard, “Using microfluidic device to study rheological properties of heavy oil,” AIChE Annual Meeting, San Francisco, USA, 2016.

[25] D. Cuthiell, C. Mccarthy, T. Frauenfeld, S. Cameron, G. Kissel, “Investigation of the VAPEX process using CT scanning and numerical simulation,” Journal of Canadian Petroeum Technology, vol. 42, pp. 41-49, 2003.

[26] H. Moriceau, F. Rieutord, F. Fournel, Y. Le Tiec, L. Di Cioccio, C. Morales, A. M. Charvet, C. Deguet, “Overview of recent direct wafer bonding advances and applications Advances in Natural Sciences,” Nanoscience and Nanotechnology, vol. 1(4), pp. 043004, 2010.

[27] D. Lesueur, “The colloidal structure of bitumen: consequences on the rheology and on the mechanisms of bitumen modification,” Advances in Colloid and Interface Science, vol. 145, pp. 42-82, 2009.

[28] L. Corbett, “Composition of asphalt based on generic fractionation, using solvent deasphaltening, elution-adsorption chromatography and densimetric characterization,” Analytical Chemistry, vol. 41, pp. 576-79, 1969.

[29] S. J. Abedi, H. Y. Cai, S. Seifaie, J. M. Shaw, Simultaneous phase behavior, elemental composition and density measurement using x-ray imaging, Fluid Phase Equilibria, vol. 158-160, pp. 775-781, 1999.

[30] X. Zhang, J. M. Shaw, “Liquid-phase mutual diffusion coefficients for heavy oil + light hydrocarbon mixtures,” Petroleum Science Technology, vol. 25, pp. 773-90, 2007.

[31] R. B. Bird, W.E. Stewart, E. N. Lightfoot, “Transport Phenoena,” 2nd ed. New York: Wiley, 2002.

[32] H. Fadaei, J. M. Shaw, D. Sinton, “Bitumen-toluene mutual diffusion coefficients using microtluidics,” Energy & Fuels, vol. 27, pp. 2042-48, 2013.

[33] J. Crank, “The Mathematics of Diffusion,” 2nd ed. London: Oxford University Press, 1975.

[34] M. Ghanavati, H. Hassanzadeh, J. Abedi, “Critical review of mutual diffusion coefficient measurements for liquid solvent bitumen/heavy oil mixtures,” Canadian Journal of Chemical Engineering, vol. 92, pp. 1445-66, 2014.

[35] E. W. Funk, “Behavior of tar sand bitumen with paraffinic solvents and its application to separations for athabasca tar sands,” Canadian Journal of Chemical Engineering, vol. 57, pp. 333-41, 1979.

[36] Y. W. Wen, A. Kantzas, “Monitoring bitumen-solvent interactions with low-field nuclear magnetic resonance and X-Ray computer-assisted tomography,” Energy & Fuels, vol. 19, pp. 1319-26, 2005.

[37] B. Afsahi, A. Kantzas, “Advances in diffusivity measurement of solvents in oil sands,” Canadian International Petroleum Conference, Calgary, Canada, 2006.

[38] B. C. H. Fu, C. R. Phillips, “New technique for determination of diffusivities of volatile hydrocarbons in semi-solid bitumen,” Fuel, vol. 58, pp. 557-60, 1979.

[39] U. E. Guerrero Aconcha, A. Kantzas, “Diffusion of hydrocarbon gases in heavy oil and bitumen,” Latin American Caribbean Petroleum Engineering Conference, Cartagena de Indias, Colombia, 2009.

[40] A. Fayazi, S. Kryuchkov, A. Kantzas, “Evaluating diffusivity of toluene in heavy oil using nuclear magnetic resonance imaging,” Energy & Fuels, vol. 31, pp. 1226-34, 2017.

[41] A. Yeung, T. Dabros, J. Czarnecki, J. Masliyah, “On the interfacial properties of micrometre–sized water droplets in crude oil,” Processing of The Royal Society A: Mathematical, Physical and Engineering Science, vol. 455, pp. 3709-23, 1999.

[42] B. Long, M. Chadakowski, J. M. Shaw, “Impact of liquid-vapor to liquid-liquid-vapor phase transitions on asphaltene-rich nanoaggregate behavior in Athabasca vacuum residue + pentane mixtures,” Energy & Fuels, vol. 27, pp. 1779-90, 2013.

Chapter 5

[1] S. Gupta, S. Gittins and P. Picherack, "Insights into some keyissues with solvent aided process," J. Can. Petrol. Technol., vol. 43, pp. 54–61, 2003.

[2] B. Rostamin, S. R. Etminan, A. Soleimani and R. Kharrat, "Effect of Capillarity and Surface Tension on the performance of VAPEX Process," Canadian International Petroleum Conference, 2007.

[3] J. N. kuo and Y. K. Lin, "Capillary-Driven Dynamics of Water in Hydrophilic Microscope Coverslip Nanochannels," Japanese Journal of Applied Physics, pp. 51, 2012.

[4] D. Sinton, "Energy: the microfluidic frontier," Lab Chip, vol. 14, pp. 3127-3134, 2014.

[5] J. C. Mcdonal, D. C. Duffy, J. R. Anderson, D. T. Chiu, H. Wu, O. J. Shueller and G. M. Whitesides, "Fabrication of microfluidic systems in poly(dimethylsiloxane)," Electrophoresis, vol. 21, no. 1, pp. 27-40, 2000.

[6] D. N. Breslauer, P. J. Lee and L. P. Lee, "Microfluidics-based systems biology," Molecular Biosystems, vol. 2, pp. 97–112, 2006.

[7] R. Sharma and D. S. Ross, "Kinetics of Liquid Penetration into Periodically Constricted Capillaries," Journal of The Chemical Society, Faraday Transactions, vol. 87, no. 4, pp. 619-624, 1991.

[8] J. Berthier, D. Gosselin, A. Pham, F. Boizot, G. Delapierre, N. Belgacem, D. Chaussy, “Spontaneous capillary flows in piecewise varying cross section microchannels” Sensors and Actuators B: Chemical, vol. 223, pp. 868-877, 2016.

[9] j. Bauer, G. Drescher and M. Illig, "Surface tension, adhesion and wetting of materials for photolithographic process," Journal of Vacuum Science & Technology B, Microelectrons and Nanometer Structures Processing, Measurement and Phenomena, vol. 14, no. 4, pp. 2485, 1996.

[10] W. G. Anderson, "The Effects of Wettability on the Electrical Properties of Porous Media," Journal of Petroleum Technology, vol. 38, pp. 1371–1378, 1986.

[11] V. Dwarakanath, R. E. Jackson and G. A. Pope, "Influence of wettability on the recovery of NAPLs from alluvium," Environmental Science & Technology, vol. 36, no. 2, pp. 227–231, 2002.

[12] S. M. Benson and D. R. Cole, "sequestration in deep sedimentary formations," Elements, vol. 4, pp. 325–331, 2008.

[13] Abdallah, W., et al, "The fundamentals of wettability," Oilfield Review, vol. 19, pp. 44-63, 2007.

[14] K. L. Mittal, "The Role of Polarity in the Structure of Silanes Employed in Surface Modification," in Silanes and Other Coupling Agents, CRC Press, pp. 51-64, 2009.

[15] K. Keshmiri, S. Mozaffari, P. Tchoukov, H. Huang and N. Nazemifard, "Using Microfluidic Device to Study Rheological Properties of Heavy Oil," in American Institute of Chemical Engineering (AIChE), San Francisco, 2016.

[16] G. Hu, D. Li, “Multiscale phenomena in microfluidics and nanofluidics” Chemical Engineering Science, vol. 62 no. 13, pp. 3443-3454, 2007.

[17] L. J. Yang, T. J. Yao and Y. C. Tai, "The marching velocity of the capillary meniscus in a microchannel," Journal of Micromechanics and Microengineering, vol. 14, pp. 220–225, 2004.

[18] S. V. Garimella and C. B. Sobhan, "Transport in microchannels – A critical review," Annual Review Heat Transfer, vol. 13, pp. 1–50, 2003.

[19] E. W. Washburn, "The Dynamics of Capillary Flow," Physical Review, vol. 17, pp. 273, 1921.

[20] R. Chebbi, "Electroosmotic-capillary penetration in circular microchannels," Journal of Colloid and Interface Science, vol. 361, pp. 639-642, 2011.

[21] N. R. Tas, J. Haneveld, H. V. Jansen, M. Elwenspoek and A. van den Berg, "Capillary filling speed of water in nanochannels," Applied Physics Letters, vol. 85, pp. 3274-3276, 2004.

[22] S. Mozaffari, P. Tchoukov, A. Mozaffari, J. A. J. Czarnecki and N. Nazemifard, "Capillary driven flow in nanochannels – Application to heavy oil rheology studies," Colloids and Surfaces A: Physicochemical Engineering Aspects, vol. 513, pp. 178-187, 2017.

[23] J. Kuo and W. Wang, "Capillary Filling Speed of Ferrofluid in Hydrophilic Microscope Slide Nanochannels," Microfluidic Nanofluidic, vol. 18, pp. 57-64, 2015.

[24] A. Saha, S. K. Mitra, M. Tweedie, S. Roy and J. McLaughlin, "Experimental and numerical investigation of capillary flow in SU8 and PDMS microchannels with integrated pillars," Microfluidic Nanofluidic, vol. 7, pp. 451-465, 2009.

[25] S. Levine, J. Lowndes and R. Reed, ""Two-Phase Fluid Flow and Hysteresis in a Periodic Capillary Tube," Journal of Colloids & Interface Science, vol. 77, pp. 253-263, 1980.

[26] A.F. Stalder, G. Kulik, D. Sage, L. Barbieri, and P. Hoffmann, "A Snake-based approach to accurate determination of both contact points and contact angles", Colloids & Surfaces A, vol. 286, pp. 92-103, 2006.

[27] P. G. de Gennes, "Wetting: statics and dynamics," Reviews of Modern Physics , vol. 57, no. 3, pp. 827, 1985.

[28] D. Burgreen and F. R. Nakache, "Electrokinetic Flow in Ultrafine Capillary Slits," The Journal of Physical Chemistry , vol. 68, no. 5, pp. 1084-1091, 1964.

[29] J. C. T. Eijkel, J. Bomer, N. R. Tas and A. van den Berg, "1-D nanochannels fabricated in polyimide," Lab Chip, vol. 4, pp. 161-3, 2004.

[30] W. P. Hardy, "The spreading of fluids on glass," Philos. Mag., vol. 38, pp. 38-49, 1919.

[31] M. Ledyastuti, Y. Liang, M. Kunieda and T. Matsuoka, "Asymmetric orientation of toluene molecules at oil-silica interfaces," The Journal of Chemical Physics, vol. 137, 2012.

[32] K. M. Davisa, A. Agarwala, M. Tomozawa and K. Hiraob, "Quantitative infrared spectroscopic measurement of hydroxyl concentrations in silica glass," Journal of Non-Crystalline Solids, vol. 203, pp. 27-36, 1996.

[33] S. Knaust, M. Andersson, K. Hjort and L. Klintberg, "Influence of surface modifications and channel structure for microflows of supercritical carbon dioxide and water," The Journal of Supercritical Fluids, vol. 107, pp. 649-656, 2016.

[34] J. V. Alsten, and S. Granick,, "Shear rheology in a confined geometry: polysiloxane melts," Macromolecules, vol. 23, pp. 4856-4862, 1990.

[35] R. C. R. da Silva, R. S. Mohamed and A. C. Bannwart, "Wettability alteration of internal surfaces of pipelines for use in the transportation of heavy oil via core-flow," Journal of Petroleum Scienec and Engineerign , vol. 51, pp. 17-25, 2006.

[36] P. Fabbri, M. Messori, F. Pilati, R. Taurino, C. Tonelli, M. Toselli, “Hydrophobic and oleophobic coatings based on perfluoropolyether/silica hybrids by the sol-gel method” Advances in Polymer Technology, vol. 26, pp. 182-190, 2007.

[37] Y. F. Chen, F. G. Tseng, S. Y. C. Chien, M. H. Chen, R. J. Yu and C. C. Chieng, "Surface tension driven flow for open microchannels with different turning angles," Microfluidic Nanofluidic, vol. 5, no. 2, pp. 193-203, 2008.

[38] H. J. Barraza, S. Kunapuli and E. A. O'Rear, "Advancing Contact Angles of Newtonian Fluids During "High" Velocity, Transient, Capillary-Driven Flow in a Parallel Plate Geometry," Journal of Physics & Chemistry B, vol. 106, pp. 4979-4987, 2002.

[39] R. L. Hoffman, "A study of the advancing interface," Journal of Colloids and Intertace Science, vol. 50, pp. 228, 1975.

[40] F. A. L. Dullirn, M. S. El-Sayed and V. K. Batra, "Rate of Capillary Rise in Porous Media with Nonuniform Pores," Journal of Colloids and Interface Science, vol. 60, pp. 497-506, 1977.

Chapter 6

[1] P. Luo and Y. Gu, "Effects of Asphaltene Content and Solvent Concentration on Heavy Oil Viscosity," SPE International Thermal Operations and Heavy Oil Symposium, 1-3 November 2005.

[2] A. Firoozabadi, Thermodynamics of Hydrocarbon Reservoirs, McGraw-Hill, New York, 1999.

[3] A. B. Demir, I. H. Bilgesu and B. Hascakir, "The Effect of Brine Concentration on Asphaltene Stability," in SPE Annual Technical Conference and Exhibition, September, Dubai, UAE, 2016.

[4] O. Mohammadzadeh Shanehsaz, "Experimental Studies Focused on the Pore-Scale Aspects of Heavy Oil and Bitumen Recovery Using the Steam Assisted Gravity Drainage (SAGD)

and Solvent-Aided SAGD (SA-SAGD) Recovery Processes," University of Waterloo, Waterloo, Ontario, Canada, 2012.

[5] J. G. Speight, "The Chemical and Physical Structure of Petroleum: Effects on Recovery Operations," Journal of Petroleum Science and Engineering, vol. 22, pp. 13-15, 1999.

[6] H. Doryani, M. R. Malayeri and M. Riazi, "Visualization of asphaltene precipitation and deposition in a uniformly patterned glass micromodel," Fuel, vol. 182, pp. 613-622, 2016.

[7] F. M. Vargas, D. L. Gonzalez, J. L. Creek, J. Wang, J. Buckley and G. J. Hirasaki, "Development of a General Method for Modeling Asphaltene Stability," Energy & Fuels, vol. 23, no. 3, pp. 1147-1154, 2009.

[8] C. Stachowiak, J Viguie, J. E. Grolier, M. Rogalski, Effect of n-Alkanes on Asphaltene Structuring in Petroleum Oils, Langmuir 2005, 21, 4824-4829.

[9] S. I. Andersen, J. G. Speight, Thermodynamic Models for Asphaltene Solubility and Precipitation, Journal of Petroleum Science and Engineering, 1999, 22, 53-66.

[10] Murgich, J.; Abanero, J. A.; Strausz, O. P. Molecular recognition in aggregates formed by asphaltene and resin molecules from the Athabasca oil sand. Energy Fuels 1999, 13, 278–286.

[11] S. I. Anderson, J. G. Speight, Thermodynamic models for asphaltene solubility and precipitation, Journal of Petroleum Science and Engineering, 1999, 22, 53-66.

[12] C. Jian, T. Tang, S. Bhattacharjee, Probing the effect of side-chain length on the aggregation of a model asphaltene using molecular dynamics simulations, Energy & Fuels, 2013, 27, 2057-2067.

[13] Z.Yang, S. Chen, H. Peng, M. Li, M. Lin, Z. Dong, J. Zhang, Y. Ji, Effect of precipitating environment on asphaltene precipitation: precipitant, concentration, and temperature, Colloids and Surfaces A: Physicochemical and Engineering Aspects, 2016, 497, 327-335.

[14] D. Fenistein, L. Barre, D. Brosseta, D. Espinat, A. Livet, J. N. Roux, M. Scarsella, Viscosimetric and neutron scattering study of asphaltene aggregates in mixed toluene/heptane solvents, Langmuir 1998, 14, 1013.

[15] I. N. Evdokimov, N. Y. Eliseev, B. R. Akhmetov, Initial stages of asphaltene aggregation in dilute crude oil solution: studies of viscosity and NMR relaxation, Fuel 2003, 82, 817.

[16] A. S. Al-Qasim and M. Alasker, "Asphaltenes: what do we know so far," ASME 2017 36th International Conference on Ocean, Offshore and Arctic Engineering, pp. Trondheim, Norway, 25-30 June 2017.

[17] ECLIPSE Technical Description, "The asphaltene option," pp. 89-102, 2009.

[18] M. Tavakkoli, M. R. Grimes, X. Liu, C. K. Garcia, S. C. Correa, Q. J. Cox and F. M. Vargas, "Indirect Method: A Novel Technique for Experimental Determination of Asphaltene Precipitation," Energy & Fuels, vol. 29, pp. 2890-2900, 2015.

[19] Y. Kazemzadeh, R. Parsaei and M. Riazi, "Experimental study of asphaltene precipitation prediction during gas injection to oil reservoirs by interfacial tension measurement," Colloids and Surfaces A: Physicochemical and Engineering Aspects, vol. 466, pp. 138-146, 2015.

[20] N. Silva, V. d. R. Oliveira, M. Souza, Y. Guerrieri and G. Costa, "New method to detect asphaltene precipitation onset induced by CO_2 injection," Fluid Phase Equilibria, vol. 362, pp. 355-364, 2014.

[21] J. X. Wang and J. S. Buckley, "An experimental approach to prediction of asphaltene flocculation," in Proceedings of the SPE International Symposium on Oilfield Chemistry, Houston, TX, Feb 13−16, 2001.

[22] J. Taheri-Shakib, A. Shekarifard and H. Naderic, "Experimental investigation of the asphaltene deposition in porous media: Accounting for the microwave and ultrasonic effects," Journal of Petroleum Science and Engineering, vol. 163, pp. 453-462, 2018.

[23] N. I. Papadimitriou, G. E. Romanos, G. C. Charalambopoulou, M. E. Kainourgiakis, F. K. Katsaros and A. Stubos, "Experimental investigation of asphaltene deposition mechanism during oil flow in core samples," Journal of Petroleum Science and Engineering, vol. 57, no. 3-4, pp. 281-293, 2007.

[24] A. Memon, C. Borman, O. Mohammadzadeh, M. Garcia, D. J. R. Tristancho and J. Ratulowski, "Systematic evaluation of asphaltene formation damage of black oil reservoir fluid from Lake Maracaibo, Venezuela," Fuel, vol. 206, pp. 258-275, 2017.

[25] H. Rassamdana, B. Dabir, M. Nematy, M. Farhani and M. Sahimi, "Asphalt Flocculation and Deposition: I. The Onset of Precipitation," AIChE Journal, vol. 42, p. 3318, 1996.

[26] E. Buenrostro-Gonzalez, C. Lira-Galeana, A. Gil-Villegas and J. Wu, "Asphaltene Precipitation in Crude Oils: Theory and Experiments," AIChE Journal, vol. 50, no. 10, pp. 2552-2570, 2004.

[27] B. S. Soulgani, B. Tohidi, M. Jamialahmadi and D. Rash, "Modeling formation damage due to asphaltene deposition in the porous media," Energy & Fuels, vol. 25, no. 2, pp. 753-761, 2011.

[28] S. Wang and F. Civan, "Productivity Decline of Vertical and Horizontal Wells by Asphaltene Deposition in Petroleum Reservoirs," SPE International Symposium on Oilfield Chemistry, 13-16 February 2001.

[29] A. Taherpour, A. Cheshmeh Sefidi and A. Bemani, "Application of Fuzzy c-means algorithm for the estimation of Asphaltene precipitation," Petroleum Science and Technology, vol. 36, no. 3, pp. 239-243, 2018.

[30] S. Mohebbinia, K. Sepehrnoori, R. T. Johns and A. Kazemi Nia Korrani, "Simulation of asphaltene precipitation during gas injection using PC-SAFT EOS," Journal of Petroleum Science and Engineering, vol. 158, pp. 693-706, 2017.

[31] I. Chatzis, "Pore Scale Mechanisms of Heavy Oil Recovery using the VAPEX Process," in Proceedings: International Symposium of Society of Core Analysts, Monterey, CA, 2002.

[32] S. A. Farzaneh, A. A. Dehghan, M. H. Ghazanfari and R. Kharrat, "A Comparative Study on WAS, SWAS, and Solvent-Soak Scenarios Applied to Heavy-Oil Reservoirs Using Five-Spot Glass Micromodels," Journal of Canadian Petroleum Technology, vol. 51, no. 5, pp. 383-392, 2012.

[33] K. Keshmiri, S. Mozaffari, P. Tchoukov, H. Huang and N. Nazemifard, "Using Microfluidic Device to Study Rheological Properties of Heavy Oil," AIChE Annual Meeting and Conference, 13-18 November 2016.

[34] Y.-j. Lin, P. He, M. Tavakkoli, N. T. Mathew, Y. Y. Fatt, J. C. Chai, A. Goharzadeh, F. M. Vargas and S. L. Biswal, "Examining asphaltene solubility on deposition in model porous media," Langmuir, vol. 32, pp. 8729-8734, 2016.

[35] A. Telmadarreie and J. Trivedi, "Dynamic Behavior of Asphaltene Deposition and Distribution Pattern in Fractured Porous Media during Hydrocarbon Solvent Injection: Pore-Level Observations," Energy & Fuels, vol. 31, no. 9, pp. 9067-9079, 2017.

[36] Z. Qi, A. Abedini, A. Sharbatian, Y. Pang, A. Guerrero and D. Sinton, "Asphaltene Deposition during Bitumen Extraction with Natural Gas Condensate and Naphtha," Energy & Fuels, vol. 32, no. 2, pp. 1433-1439, 2018.

[37] Y.-J. Lin, P. He, M. Tavakkoli, N. T. Mathew, Y. Y. Fatt, J. C. Chai, A. Goharzadeh, F. M. Vargas and S. L. Biswal, "Characterizing Asphaltene Deposition in the Presence of Chemical Dispersants in Porous Media Micromodels," Energy & Fuels, vol. 31, pp. 11660-11668, 2017.

[38] V. J. Sieben, A. K. Tharanivasan, J. Ratulowski and F. Mostowfi, "Asphaltenes yield curve measurements on a microfluidic platform," Lab on a Chip, vol. 15, p. 4062, 2015.

[39] C. Hu, J. E. Morris and R. L. Hartman, "Microfluidic investigation of the deposition of asphaltenes in porous media," Lab on a Chip, vol. 14, pp. 2014-2022, 2014.

[40] X. Liu, P. K. Chu and C. Ding, "Surface modification of titanium, titanium alloys, and related materials for biomedical applications," Materials Science and Engineering: R: Reports, vol. 47, no. 3-4, pp. 49-121, 2004.

[41] S. Li, M. Genys, K. Wang and O. Torsæter, "Experimental study of wettability alteration during nanofluid enhanced oil recovery process and its effect on oil recovery," in SPE Reservoir Characterisation and Simulation Conference and Exhibition, Abu Dhabi, UAE, 2015.

[42] X. Sun, C. Dai, Y. Sun, M. Du, T. Wang, C. Zou and J. He, "Wettability alteration study of supercritical CO_2 fracturing fluid on low permeability oil reservoir," Energy & Fuels, vol. 31, no. 12, p. 13364–13373, 2017.

[43] P. P. Jadhunandan and N. Morrow, "Effect of wettability on waterflood recovery for crude-oil/brine/rock systems," Society of Petroleum Engineers, vol. 10, no. 1, 1995.

[44] M. Khishvand, A. H. Alizadeh, I. O. Kohshour, M. Piri and R. S. Prasad, "In situ characterization of wettability alteration anddisplacement mechanisms governing recovery enhancementdue to low-salinity waterflooding," Water Resources Research, vol. 53, p. 4427–4443, 2017.

[45] K. L. Mittal, Silanes and other coupling agents, CRC Press, Leiden, 2009.

[46] H. Alboudwarej, D. Pole, W. Y. Svrcek and H. W. Yarranton, "Adsorption of asphaltenes on metals," Industrial & Engineering Chemistry Research, vol. 44, no. 15, p. 5585, 2005.

[47] K. R. Dean and J. L. McAtee Jr, "Asphaltene adsorption on clay," Applied Clay Science, vol. 1, no. 4, pp. 313-9, 1986.

[48] A. Zahabi and M. R. Gray, "Kinetics and Properties of Asphaltene Adsorption on Surfaces," Energy & Fuels, vol. 26, p. 1009−1018, 2012.

[49] S. Pendharker, S. Shende, W. Newman, S. Ogg, N. Nazemifard, Z. Jacob, “Axial super-resolution evanescent wave tomor,” Opt. Lett., 41, 5499-5502, 2016.

[50] H. T. Zhang, R. Li, Z. Yang, C. X. Yin, M. R. Gray, C. Bohne, “Evaluating steady-state and time-resolved fluorescence as a tool to study the behavior of asphaltene in toluene.” Photochem. Photobiolog. Sci., 13, 917-928, 2014.

[51] Axelrod D. Total internal reflection fluorescence microscopy. Methods Cell Biol 2008;89:169–221.

[52] Shen H, Huang E, Das T, Xu H, Ellisman M, Liu Z. Tirf microscopy with ultrashort penetration depth. Opt Express 2014;22(9):10728–34.

[53] Hooshiar, A.; Uhlik, P.; Ivey, D. G.; Liu, Q.; Etsell, T. H. Clay minerals in nonaqueous extraction of bitumen from Alberta oil sands: Part 2. Characterization of clay minerals. Fuel Process. Technol. 2012, 96, 183−194.

[54] H. Fadaei, J. M. Shaw and D. Sinton, "Bitumen-Toluene Mutual Diffusion Coefficients Using Microtluidics," Energy & Fuels, vol. 27, pp. 2042-2048, 2013.

[55] M. M. Shadman, A. H. Saeedi Dehaghani and M. H. Badizad, "How much do you know about the methods for determining onset of asphaltene precipitation?," Petroleum, vol. 3, pp. 287-291, 2017.

[56] T. Maqbool, A. T. Balgoa, H. S. Fogler, “Revisiting asphaltene precipitation from crude oils: a case of neglected kinetic effects,” Energy & Fuels, vol. 23, pp. 3681-3686, 2009.

[57] F. Trejo, J. Ancheyta, M. S. Rana, “Structural characterization of asphaltene obtained hydroprocessed crude oils by SEM and TEM” Energy & Fuels, 23, 429–439, 2009.

[58] J. Wang, Q. Shi, Z. Huang, Y. Gu, L. Musango, Y. Yang, “Experimental investigation of particle size effect on agglomeration behaviors in gas-solid fluidized beds” Ind. Eng. Chem. Res., 54, 12177−12186, 2015.

[59] N. Jouault, Y. Corvis, F. Cousin, J. Jestin, L. Barre, “Asphaltene Adsorption Mechanisms on the Local Scale Probed by Neutron Reflectivity: Transition from Monolayer to Multilayer Growth above the Flocculation Threshold,” Langmuir, 25, 3991-3998, 2009.

Appendix A: MATLAB codes and numerical simulation of mass conservation equation

In numerical simulation, equations are solved by finite difference mathematical expression of the partial derivatives. Gridding is 1D in x direction in the elevation of diffusion (from 100% bitumen to 100% solvent). There are two conditions of constant and variant density for Fickian diffusion equation using the explicit method.

$$\frac{\partial \mathrm{w}}{\partial \mathrm{t}} = \mathrm{D}\frac{\partial^2 \mathrm{w}}{\partial \mathrm{x}^2} \qquad (A-1)$$

First approach is constant density and explicit method. Two sides of the above equation are discretized as below:

$$\frac{\partial^2 \mathrm{w}}{\partial \mathrm{x}^2} = \frac{w_{i+1}^t - 2w_i^t + w_{i-1}^t}{\Delta x^2} \qquad (A-2)$$

$$\frac{\partial \mathrm{w}}{\partial \mathrm{t}} = \frac{w_i^{t+\Delta t} - w_i^t}{\Delta t} \qquad (A-3)$$

Where w is the hexane mass fraction, t is the time, and i is the i^{th} node in the x direction. Substitution of equation (A-2) and (A-3) in the equation (A-1) corresponds to equation (A-4) Which gives the hexane mass fraction of solvent at i^{th} node at the next time step $(t + \Delta t)$.

$$\frac{w_i^{t+\Delta t} - w_i^t}{\Delta t} = D\,\frac{w_{i+1}^t - 2w_i^t + w_{i-1}^t}{\Delta x^2} \qquad (A-4)$$

or

$$w_i^{t+\Delta t} = w_i^t + \frac{\mathrm{D}.\Delta \mathrm{t}}{\Delta x^2}(w_{i+1}^t - 2w_i^t + w_{i-1}^t) \qquad (A-4)$$

Equation (A-4) can be used for internal nodes and solved for each one separately. The boundary condition of solvent concentration equal to zero at the bitumen-rich side and equal to 1 at the hexane-rich side is considered. There is also zero flux boundary condition which concentration of each boundary node is equal to the next node (at the left-hand-side) or is equal to the previous node (at the right-hand-side) of the region of interest.

$$\frac{w_i^t - w_{i+1}^t}{\Delta \mathrm{x}} = 0 \qquad or \qquad w_i^t = w_{i+1}^t \tag{A-5}$$

$$\frac{w_i^t - w_{i-1}^t}{\Delta \mathrm{x}} = 0 \qquad or \qquad w_i^t = w_{i-1}^t \tag{A-6}$$

The second approach is variant density and explicit method. The equation and discretized sides are:

$$\frac{\partial(\rho \mathrm{w})}{\partial \mathrm{t}} = \mathrm{D}\frac{\partial}{\partial \mathrm{x}}\left(\rho \frac{\partial(\mathrm{w})}{\partial \mathrm{t}}\right) \tag{A-7}$$

$$\frac{\partial(\rho \mathrm{w})}{\partial \mathrm{t}} = \frac{\rho_i^{t+\Delta t} w_i^{t+\Delta t} - \rho_i^t w_i^t}{\Delta t} \tag{A-8}$$

$$\frac{\partial}{\partial \mathrm{x}}\left(\rho \frac{\partial(\mathrm{w})}{\partial \mathrm{t}}\right) = \frac{\rho_{i+1/2}^t \partial w^t \Big/ \partial x_{i+1/2} - \rho_{i-1/2}^t \partial w^t \Big/ \partial x_{i-1/2}}{\Delta x} =$$

$$\frac{\rho_{i+\frac{1}{2}}^t (w_{i+1}^t - w_i^t) - \rho_{i-\frac{1}{2}}^t (w_i^t - w_{i-1}^t)}{\Delta x^2} \tag{A-9}$$

Substituting the (A-8) and (A-9) equations in the (A-7) equation lead to the calculation of solvent mass fraction for each internal node based on the following equation:

$$w_i^{t+\Delta t} = w_i^t + \frac{\mathrm{D}.\Delta \mathrm{t}}{\rho_i^t \Delta x^2}\left[\rho_{i+\frac{1}{2}}^t (w_{i+1}^t - w_i^t) - \rho_{i-\frac{1}{2}}^t (w_i^t - w_{i-1}^t)\right] \tag{A-10}$$

In equation (A-10), it was assumed that density at the next time step is almost equal to the density at the present time $\left(\rho_i^{t+\Delta t} = \rho_i^t\right)$ if time step is very small. This assumption was verified by implicit solution of the diffusion mass transfer equation. Densities at $i + \frac{1}{2}$ and $i - \frac{1}{2}$ estimated with the following equations:

$$\rho_{i+1/2}^t = \frac{2\rho_i^t \times \rho_{i+1}^t}{\rho_i^t + \rho_{i+1}^t} \qquad (A-11)$$

$$\rho_{i-1/2}^t = \frac{2\rho_i^t \times \rho_{i-1}^t}{\rho_i^t + \rho_{i-1}^t} \qquad (A-11)$$

MATLAB codes for simulation of constant and variant density with constant diffusion coefficient and concentration-dependent diffusion coefficient is presented below.

Constant density, explicit:

```
function [X,Y,t]= rho_cte
clc
close all
clear all
global A Q
global rho D
global Dx Dt
global N
global Yclc
L = 0.00562;
rho = 840;
DNOT = 1.9e-10;
rlx=1; eps=1e-5;
time_req = 2000;
Y1 = 0;  %BC
YNPLUS1 = 1; %BC
```

```
N =800;
Dx = L/N;
Dt=1;
Y = ones(N-1,1);
for ii = 1:0.0036/Dx
  Y(ii) = 0;
end
A = zeros(N-1,N-1);
Q = zeros(N-1,1); nitr = 1e20;
YM(:,1) = [Y1; Y; YNPLUS1];
for j = 1:nitr
   func_A_Q;
   if j==round(10/Dt)
      YM(:,2)=[Y1;Y;YNPLUS1];
   end
   if j==round(104/Dt)
      YM(:,3)=[Y1;Y;YNPLUS1];
   end
   if j==round(215/Dt)
      YM(:,4)=[Y1;Y;YNPLUS1];
   end
    if j==round(328/Dt)
      YM(:,5)=[Y1;Y;YNPLUS1];
   end
    if j==round(581/Dt)
      YM(:,6)=[Y1;Y;YNPLUS1];
   end
    if j==round(865/Dt)
      YM(:,7)=[Y1;Y;YNPLUS1];
   end
    if j==round(1537/Dt)
      YM(:,8)=[Y1;Y;YNPLUS1];
   end
   if j == round(time_req/Dt)
   break
   end
end
x = 0:Dx:L;
```

```
x=x.*1000;
t = 0:Dt:j*Dt;
[~, ~, raw] = xlsread('T_Shape_Data.xlsx');
raw    = raw(5:1686,281:289);
data   = reshape([raw{:}],size(raw));
c10s   = data(:,3);
c104s  = data(:,4);
c215s  = data(:,5);
c328s  = data(:,6);
c581s  = data(:,7);
c865s  = data(:,8);
c1537s = data(:,9);
x=data(:,1);
figure(1)
plot(x,c10s,'--r'); title('t=10.4s');xlabel('x (mm)');ylabel('Hexane mass fraction');
hold on;plot(X,YM(:,2));
figure(2)
plot(x,c104s,'--r',); title('t=104s'); xlabel('x (mm)');ylabel('Hexane mass fraction');
hold on;plot(X,YM(:,3));
figure(3)
plot(x,c215s,'--r'); title('t=215s');xlabel('x (mm)');ylabel('Hexane mass fraction');
hold on;plot(X,YM(:,4));
figure(4)
plot(x,c328s,'--r'); title('t=328s');xlabel('x (mm)');ylabel('Hexane mass fraction');
hold on;plot(X,YM(:,5));
figure(5)
plot(x,c581s,'--r'); title('t=581s');xlabel('x (mm)');ylabel('Hexane mass fraction');
hold on;plot(X,YM(:,6));
figure(6)
plot(x,c865s,'--r'); title('t=865s');xlabel('x (mm)');ylabel('Hexane mass fraction');
hold on;plot(X,YM(:,7));
figure(7)
plot(x,c1537s,'--r');title('t=1537s');xlabel('x(mm)');ylabel('Hexane mass fraction');
hold on;plot(X,YM(:,8));

function func_A_Q
   for i=2:N-2
   d(i)=1/(Y(i)/ds+(1-Y(i))/db);
```

```
   end
   d(1)=1/(Y(1)/ds+(1-Y(1))/db);
   d(N-1)=1/(Y(N-1)/ds+(1-Y(N-1))/db);
   for i=2:N-2
      Y(i)=Y(i)+D*DT*((Y(i+1)-Y(i))*(d(i+1)+d(i))/2-(Y(i)-Y(i-1))*(d(i-1)+d(i))/2)/DX^2/d(i);
   end
  Y(1)=Y(1)+D*DT*((Y(1+1)-Y(1))*(d(1+1)+d(1))/2-(Y(1)-0)*(db+d(1))/2)/DX^2/d(1);
  Y(N-1)=Y(N-1)+D*DT*((YNPLUS1-Y(N-1))*(ds+d(N-1))/2-(Y(N-1)-Y(N-2))*(d(N-2)+d(N-
1))/2)/DX^2/d(N-1);
  YNPLUS1=Y(N-1);
return
```

Variable density, concentration dependent diffusion coefficient, explicit:

```
function [X,Y]= rho
clc
clear all
global A Q
global rho D
global Dx Dt
global N
global Y Y1 YNPLUS1
global YC
L=0.03095;
D = .2e-10;
 for    iii=1:300
 nitr=100000;
time_req = 1600;
Y1 = 0;
YNPLUS1 = 1;
N=500;
Dx = L/N;
Dt=25;
Y = ones(N-1,1);
for ii = 1:0.0036/DX
  Y(ii) = 0;
end
```

```
for j = 1:nitr
   func_A_Q;
   if j==round(3*3600/DT)
      YM(:,iii)=[Y1;Y;YNPLUS1];
   end
   if j == round(time_req/DT)
    break
   end
end
D=D+0.01e-10;
fprintf('Solution for D, D = %3.3f is obtained\n', (iii-1)*0.01+.2)
 end
 X = 0:DX:L;
X=X.*1000;
 [m,n]=size(YM);
 YM=YM.*100;
[~, ~, raw] = xlsread('T-Shaped.xlsx');
raw = raw(3:652,50:55);
data = reshape([raw{:}],size(raw));
c=data(:,3);
c=c.*100;
x=[0:0.04764024:30.95628048];
[m1,n1]=size(c);
for j=1:90
       for k=0:(m1-1)
          if c(m1-k,1)==j
             s(n+1,j)=(c(m1-k+1)-c(m1-k-1))/(x(m1-k+1)-x(m1-k-1));
             break;
          end
          if c(m1-k,1)<j
             s(n+1,j)=(c(m1-k+1,1)-c(m1-k,1))/(x(m1-k+1)-x(m1-k));
             break;
          end
       end
end
 for i=1:n
    for j=1:90
       s(i,j)=abs(s(i,j)-s(n+1,j));
```

```
    end
  end
  w=min(s(1:n,:));

  for j=1:90
     for i=1:n
        if s(i,j)==w(j);
           D(j)=(0.2+(i-1)*0.01)*10^(-10);
        end
     end
  end

  c=linspace(1,90,90);
  figure(1)
  hold on
  plot(c,D);
X = 0:DX:L;
X=X.*1000;
    function func_A_Q
       global A Q rho D DX N DT Y Y1 YNPLUS1 YC
       ds=624;
  db=1026;
    for i=2:N-2
       d(i)=1/(Y(i)/ds+(1-Y(i))/db);
    end
    d(1)=1/(Y(1)/ds+(1-Y(1))/db);
    d(N-1)=1/(Y(N-1)/ds+(1-Y(N-1))/db);
    for i=2:N-2
       Y(i)=Y(i)+D*DT*((Y(i+1)-Y(i))*(d(i+1)+d(i))/2-(Y(i)-Y(i-1))*(d(i-1)+d(i))/2)/DX^2/d(i);
    end
   Y(1)=Y(1)+D*DT*((Y(1+1)-Y(1))*(d(1+1)+d(1))/2-(Y(1)-0)*(db+d(1))/2)/DX^2/d(1);

return
```

Appendix B: Microfabrication steps

In this study, 4 inches × 4 inches × 0.043 inches borofloat (81 % SiO_2, 13 % B_2O_2, 4 % Na_2O/K_2O, 2 % Al_2O_3) glass wafer was used for fabrication. Wafers were cleaned using piranha solution (H_2SO_4 and H_2O_2 with 3:1 volume ratio) at wet deck. For this purpose, select a glass container and label it with "piranha", your name, and date. Prepare two beakers for sulphuric acid and hydrogen peroxide and mark them according to the desired amount of piranha solution. Put on the apron, face shield and chemical resistant gloves. Ensure there are no leaks with the gloves using the nitrogen gun. Pour the sulphuric acid into the labeled container first and then add the hydrogen peroxide slowly into the container and rinse the beakers for 5 cycles. Wash the sulphuric acid and hydrogen peroxide bottles and pat dry with a wipe. Place the wafers carrier into the piranha bath for 15 minutes. When piranha cleaning has done, remove the carrier from the bath and put the carrier into the dump rinser for 5 cycles and dry wafers with spin rinse dryer.

Layers of Cr and Au were coated on the wafers that act as the masking layer using sputtering system 1 (Bob). First section is opening and loading of the chamber. Chamber should be at atmospheric pressure (760 Torr) and chamber vent switch must be closed. After opening the chamber, load three glass wafers and direct the top section down until it meets the chamber. Pump down the pressure to about -6 Torr and deposited the desired target (first chrome and then gold) for a specific time. Full SOP is provided with the following link:
https://www.nanofab.ualberta.ca/capabilities/process-information/

Photoresist (HPR 504) was spun onto the wafer (500 rpm for 10 s followed by 4000 rpm for 40s) and soft baked for 110 s at 115 °C using CEE 200CB coat-bake. Photoresist was exposed to

light through a photomask (3s), previously designed using L-edit software, to transfer the pattern then resist was developed (354 developer). L-edit training videos can be find at the following link:

https://www.nanofab.ualberta.ca/user-information/centre-access/photomask-information/l-edit-training-videos/

Au and Cr layers were wet etched using gold etchant and chrome etchant with a visual endpoint. Pick three glass container and label them with Cr etchant, Au etchant, and acetone. Submerse the wafer in Au etchant first and when gold is fully removed, wash the wafer with DI water. Put it in the Cr etchant and at the end of etching process, submerse the wafer in acetone until the photoresist is stripped away. Put the wafer container in 5 cycles rinser, transfer the etchants to storage bottles and wash wet deck.

Borofloat glass was etched using Hydrofluoric acid (HF) for the specific time to obtain desired channel depth. Label two plastic containers with HF and water (for quenching the etching), your name and the date. Put on the apron, face shield and chemical resistant gloves. Ensure there are no leaks with the gloves using the nitrogen gun. Bring a bottle of etchant and pour it into the container with a magnet at the bottom. Put the wafers in a carrier and hang them inside the container. Accurate etch rate (depth/time) was first determined using the contact profilometer (Alphastep) and the total time of etching was calculated. At the end of the etching, lift the carrier and quench the etching by submersing the wafers in the water container and then rinse the wafers. Transfer the etchant to a labeled storage bottle; wash the outside of the bottle with calcium chloride followed by water. Wash the container with calcium chloride and rinse it for 5 cycles. Rinse the deck with calcium chloride and wash with water. Put wash the calcium chloride container and place it in chemical pass-thru.

The remaining Au, Cr, and photoresist at the unpatterned areas were removed using the etchants and acetone. The etched and unetched substrates should be bonded temporarily. Place the wafer face down in the tape applicator and center a film frame on the wafer. Pull tape over the wafer and film frame and push roller over the wafer and film frame gently and separate tape trimming from the film frame by cutting it with a cutter, carefully. Washed the wafers with bonding soap, rinse them with DI water and press together to form temporary bonding. Inspect the bonding for possible rainbow that means glasses are not bonded at that spot.